GROWTH OF NANOSTRUCTURE OF TRANSITION METAL ALLOY NITRIDE AND CARBIDE

Miss Pattira Homhuan

A Dissertation Submitted in Partial Fulfillment of the Requirements
for the Degree of Doctor of Philosophy Program in Nanoscience and Technology
(Interdisciplinary Program)
Graduate School
Chulalongkorn University
Academic Year 2010

การปลูกฟิล์มบางโครงสร้างนาโนของโลหะผสมทรานซิชันไนไตรด์และคาร์ไบด์

นางสาวภัททิรา หอมหวล

วิทยานิพนธ์นี้เป็นส่วนหนึ่งของการศึกษาตามหลักสูตรปริญญาวิทยาศาสตรดุษฎีบัณฑิต
สาขาวิชาวิทยาศาสตร์นาโนและเทคโนโลยี (สหสาขาวิชา)
บัณฑิตวิทยาลัย จุฬาลงกรณ์มหาวิทยาลัย
ปีการศึกษา 2553

Thesis Title	Growth of Nanostructure of Transition Metal Alloy Nitride and Carbide
By	Miss Pattira Homhuan
Field of Study	Nanoscience and Technology
Thesis Advisor	Assistant Professor Sukkaneste Tungasmita, Ph.D.
Thesis Co-advisor	Associate Professor Surasing Chaiyakun, Ph.D.

Accepted by the Graduate School, Chulalongkorn University in Partial Fulfillment of the Requirements for the Doctoral Degree

…… Dean of the Graduate School
(Associate Professor Pornpote Piumsomboon, Ph.D.)

THESIS COMMITTEE

…….. Chairman
(Associate Professor Vudhichai Parasuk, Ph.D.)

…… Thesis Advisor
(Assistant Professor Sukkaneste Tungasmita, Ph.D.)

…… Thesis Co-advisor)
(Associate Professor Surasing Chaiyakun, Ph.D.)

…… Examiner
(Associate Professor Duangdao Aht-Ong, Ph.D.)

…… Examiner
(Assistant Professor Warangkana Warisnoichraoen, Ph.D.)

…… External Examiner
(Sirinee Thaiwatthana, Ph.D.)

ภัททิรา หอมหวล: การปลูกฟิล์มบางโครงสร้างนาโนของโลหะผสมทรานซิชันไนไตรด์และคาร์ไบด์. (Growth of Nanostructure of Transition Metal Alloy Nitride and Carbide) อ. ที่ปรึกษาวิทยานิพนธ์หลัก: ผู้ช่วยศาสตราจารย์ ดร.สุคคเณศ ตุงคะสมิต, อ. ที่ปรึกษาวิทยานิพนธ์ร่วม: รองศาสตราจารย์ ดร. สุรสิงห์ ไชยคุณ 125 หน้า.

ฟิล์มบางโลหะผสมทรานซิชันคาร์ไบด์และไนไตรด์ปลูกโดยเทคนิคแมกนีตรอนสปัตเตอร์ริงซึ่งใช้สำหรับชั้นเคลือบป้องกันและสารกึ่งตัวนำจากออกไซด์ของโลหะ สำหรับฟิล์มโครเมียมเซอร์โคเนียมไนไตรด์ ความดันย่อยของไนโตรเจนถูกเปลี่ยนตั้งแต่ 0 ถึง 100% เพื่อหาเงื่อนไขที่ดีสุดในการปลูกฟิล์ม ผลการวิจัยพบว่าฟิล์มบางโครเมียมเซอร์โคเนียมไนไตรด์ปลูกที่ ความดันย่อยไนโตรเจนที่ 20% มีค่าความแข็งและมอดุลัสมากที่สุด ส่วนประกอบโลหะของฟิล์มสามารถถูกควบคุมโดยการปรับกระแสแมกนีตรอนที่เป้าในขณะที่ความดันย่อยไนโตรเจนที่ 20% คงที่ ผลการวิจัยแสดงว่า สารละลายของแข็งสามารถสร้างเป็นรูปเป็นร่าง ความแข็งของฟิล์มสัมพันธ์กับการเรียงตัวของผลึก ฟิล์มบางถูกอบที่อุณหภูมิ 300, 500 และ 700 องศาเซลเซียส เพื่อตรวจสอบความเสถียรทางด้านความร้อน ความแข็งของฟิล์มเพิ่มขึ้นเมื่ออุณหภูมิการอบมากขึ้น สมบัติทางกลของฟิล์มสามารถถูกพัฒนาโดยไอออนในกระบวนการปลูกฟิล์ม แทนทาลัม อิตเทรียมคาร์ไบด์สามารถเป็นหนึ่งในตัวเลือกของขั้วโลหะ แทนทาลัมอิตเทรียมคาร์ไบด์ปลูกลงบนฟิล์มออกไซด์ที่มีฮาฟเนียมเป็นส่วนประกอบหลัก สัดส่วนของอิตเทรียมสามารถเปลี่ยนแปลงได้จากการปรับกำลังของ เป้าโลหะแทนทาลัมคาร์ไบด์และอิตเทรียม สัดส่วนของอิตเทรียมในฟิล์มส่งผลต่อโครงสร้างผลึก ความต้านทาน และความต่างศักย์ราบ โครงสร้างของแทนทาลัมอิตเทรียมคาร์ไบด์ แสดงเป็น ลูกบาศก์แบบเฟซเซ็นเตอร์เมื่อ ค่าเอกซ์ในแทนทาลัมอิตเทรียมคาร์ไบด์ มีค่าน้อยกว่าหรือเท่ากับ 0.4 และโครงสร้างของแทนทาลัมอิตเทรียมคาร์ไบด์ แสดงเป็นผลึกที่ไม่เป็นระเบียบเมื่อค่าเอกซ์ในแทนทาลัมอิตเทรียมคาร์ไบด์ มีค่ามากกว่าหรือเท่ากับ 0.5 หลังจากการอบที่ 600 องศาเซลเซียส สภาพต้านทานของฟิล์มแทนทาลัมอิตเทรียมคาร์ไบด์เกือบมีค่าคงที่เมื่อค่าเอกซ์ในแทนทาลัมอิตเทรียมคาร์ไบด์ น้อยกว่าหรือเท่ากับ 0.5 หลังการอบที่ 600 องศา ความต่างศักย์ราบสามารถเปลี่ยนแปลงในขอบเขต 0.5 โวลต์ โดยการเปลี่ยนค่าเอกซ์ในแทนทาลัมอิตเทรียมคาร์ไบด์ น้อยกว่าหรือเท่ากับ 0.5 บนฮาฟเนียมออกไซด์และฮาฟเนียมซิลิเกตภายหลังการอบที่อุณหภูมิต่ำกว่า 500 องศาเซลเซียส ค่ายังผลฟังก์ชันงานของแทนทาลัมอิตเทรียมคาร์ไบด์มีค่ามากขึ้นเนื่องจากมีจำนวนออกซิเจนอยู่ในฟิล์ม

สาขาวิชา วิทยาศาสตร์นาโนและเทคโนโลยี ลายมือชื่อนิสิต ……..

ปีการศึกษา ……2553… ลายมือชื่อ อ.ที่ปรึกษาวิทยานิพนธ์หลัก……..

ลายมือชื่อ อ.ที่ปรึกษาวิทยานิพนธ์ร่วม……

4989722120 : MAJOR NANOSCIENCE AND TECHNOLOGY

KEYWORDS : TRANSITION METAL NITRIDE/TRANSITION CARBIDE

PATTIRA HOMHUAN: GROWTH OF NANOSTRUCTURE OF TRANSITION METAL ALLOY NITRIDE AND CARBIDE. ADVISOR: ASSISTANT PROFESSOR SUKKANESTE TUNGASMITA, Ph.D., CO-ADVISOR: ASSOCIATE PROFESSOR SURASING CHAIYAKUN, Ph.D. 125 pp.

Transition metal carbide and nitride thin film were grown using magnetron sputtering technique. They were new generation materials to be used as the protective layer and metal gate in metal oxide semiconductor devices, respectively. For chromium zirconium nitride films, the nitrogen partial pressure in the process was varied from 0 - 100% to find the optimized condition. The results showed that chromium zirconium nitride film grown at 20% of total pressure had the maximum hardness and modulus values. The metallic composition of the films could be controlled by varying the magnetron current of the targets while the nitrogen partial pressure was kept constant at 20% nitrogen partial pressure. The results indicated that the solid solution could be formed. The hardness of films also related to the preferred orientation of the crystal. The films were annealed at 300, 500 and 700 °C to investigate their thermal stability. The hardness values tended to increase with an increase in the annealing temperature. The mechanical properties of films could be improved by using the ion assistance during the growth. Tantalum yttrium carbide, which is a candidate for negative metal oxide semiconductor, was grown on a hafnium based high-k dielectric material. The composition of yttrium in films could be controlled by varying the power that supplied the TaC and Y targets. The yttrium contents in films also affected the structural, resistivity and flat band voltage shift in the devices. The structure of tantalum yttrium carbide $(TaC)_{1-x}Y_x$ films keep a face center cubic structure in x value ≤ 0.4 and disorder crystalline in x value ≥ 0.5. The resistivity of $(TaC)_{1-x}Y_x$ films is almost constant in x value ≤ 0.5 even after annealing at 600 °C. The flat band voltage can be controlled in the range of 0.5 V by varying x value ≤ 0.5 on hafnium oxide and hafnium silicate in the post-annealing condition below 500 °C. The effective work function may increase due to the large amount of oxygen.

Department : Nanoscience and technology Student's Signature .....

Academic Year : 2010 Advisor's Signature .....

Co-advisor's Signature .....

ACKNOWLEDGEMENTS

I would like to express my gratitude to my advisor, Assistant Professor Dr. Sukkaneste Tungasmita and Associate Professor Dr. Surasing Chaiyakun for their kind suggestion and time throughout the length of this work. I wish to express my host researcher at National Institute for Materials Science, Dr. Toshihide Nabatame and Dr. Toyohiro Chikyow for their advice and encouragement throughout in Japan.

I am also grateful to Associate Professor Dr. Vudhichai Parasuk, Associate Professor Dr. Duangdao Aht-Ong, and Dr. Sirinee Thaiwatthana for serving as chairman and the committee, respectively. All have made valuable comments and help in the production of this thesis.

I would like to thank Assistant Professor Dr. Somchai Kiatgamolchai for his support the research facilities in department of Physics, Faculty of Science, Chulalongkorn University. I also would like to thank Dr. Rattaporn Thonggoom for her support the research facilities in department of Chemistry, Faculty of Science, Mahidol University.

I also thank Mr. Hiroyuki Yamada and the members of MANA Foundry of International Center for Materials Nanoarchitectonics of National Institute for Materials Science, Japan and Mr. Nuttapong Parncharoenthaworn for helping measurement and preparation the samples.

I would like to thank The Commission on Higher Education, Graduate Thesis Grant and National Institute Materials Science for financial support that enabled this research.

Many thanks to all colleagues and friends in Nanoscience and Technology, Thailand and National Institute for Materials Science, Japan who have helped me in various ways with their friendship and encouragement.

Finally, a deep affectionate gratitude is acknowledged to my family for love, understanding, supporting and encouragement throughout my entire study.

Contents

List of Tables

List of Figures

CHAPTER I
INTRODUCTION

Thin solid films can be formed by the arrangement of individual atoms on the substrates. The thickness of thin films, as referred to the definition, is less than 1 μm. Nowadays, thin films are widely used in electronic devices, decorative parts, optical coating, hard coating and wear resistance films [1]. The properties of thin films are different from bulk materials because of the atomic growth process. In the aim of modern science and technology, it focuses on the creation new material which having novel and functional properties. These outstanding properties result from the small size of structural element in the range of 1-50 nm. This material is called "nanomaterial" [2]. In this work, we concentrate on synthesis and characterizations of novel nanomaterial with unique properties for a wide range in metal carbide and metal nitride thin film as functional materials for modern science and technology.

Transition metal nitride (MN_x form) coatings become interesting because of their outstanding mechanical and tribological properties: high hardness (20-25 GPa, approximately), good adhesion to metal substrate, good corrosion and wear resistance [3]. All these properties make metal nitride thin films have been used for mechanically and chemically protective layers for industrial applications for many years. The cubic-base structural chromium nitride is a more recent and one of interesting choice of such layers due to its well-matched properties to some industrial requirements, especially those for hard coating and tribological applications. Chromium nitride (CrN) film has a high hardness, high wear- and corrosion-resistance, and it also has a low friction-coefficient [4-5]. Adding one more metal element to the structure, Cr-based ternary nitride films have been reported that these films have improvements over the properties seen with binary compound CrN films [6-8]. However, there is an apparent lack of important information about the properties of Cr-Zr-N films derived from various growth parameters which are the keys to engineer the desired properties of the material. In this work, we explored the roles of nitrogen partial pressures and post-process annealing temperature on the structural, mechanical and electrical properties of the resultant Cr-Zr-N. We also demonstrate and discuss in the effect of low-energy ion bombardment during the film

growth with dual dc magnetron sputtering technique, for an improvement of the mechanical properties of this Cr-Zr-N ternary nitride thin films.

On the other points of view, transition metal carbide (MC_x form) is another interesting material because of high hardness and high melting point for compound with covalent bond, good electronic and thermal conductivity for compound with metallic bond. Most of metal carbide shows NaCl face center cubic (FCC) structure, which is ionic bond. One reason that makes metal carbide attractive is the combination of outstanding properties in a mixture of metallic, covalent and ionic component [9]. It is widely useful for complementary metal-oxide-semiconductor devices (CMOS) as metal gate. In CMOS technology, metal gate and high-dielectric constant (κ) are required to replace poly-crystalline silicon (poly-Si) and silicon dioxide (SiO_2), respectively. These changes are aim to eliminate polysilicon depletion, Fermi level pinning effects, gate resistance effects [10-12], leakage current and power consumption lost [13]. To obtain the greater capacitance for the maximum drive current, a dielectric with a higher permittivity ($\kappa\sim$ 20) than SiO_2 dielectric ($\kappa\sim$ 3.9) can be used. Hafnium oxide (HfO_2) and Hafnium silicate ($HfSiO_x$) are two of most promising candidates for this task. The selection of metal gate based on Hf-compound is a best choice for materials that have effective work function near the conduction and valence band edge of Si [12]. The effective work function ($\phi_{m,eff}$) of n-metal gate is 4.1 eV. Metal carbide is one choice for the negative metal-oxide semiconductor (NMOS) electrode because of low vacuum work function [8]. Nitrogen-free tantalum carbide (TaC) also emerged as a promising gate electrode of high-k metal oxide semiconductor field effect transistor (MOSFETs) because of high mobility and thermal stability [12, 14]. This nitrogen-free metal gate is interested because nitrogen in metal gate can make the work function in metal carbide increase [12, 15]. We expect that the lower effective work function ($\phi_{m,\,eff}$) can be obtained by introducing yttrium (Y) atoms with low work function of 3.1 eV into tantalum carbide (TaC) matric. In this work, we have systematically investigated the effect of Y content in tantalum yttrium carbide $(TaC)_{1-x}Y_x$ gate electrodes on structural properties, resistivity and flat band voltage (V_{fb}) control for Hf-based high-k MOS capacitors. It has been found the first time that $(TaC)_{1-x}Y_x$ can be a candidate for n-metal gate electrode in gate last process.

This thesis is divided into five chapters. In the following chapter, chapter 2, theoretical background is described. In chapter 3, some of characterization techniques that been used in this work, are described. Chapter 4 highlights about the experimental results and important discussions. The final chapter of this thesis, chapter 5, is the conclusions.

CHAPTER II
THEORETICAL BACKGROUND

2.1 Transition Metal Carbides and Nitrides

Transition metal nitride and carbide show the outstanding properties: high hardness, high melting point (TaC has the highest melting point), high electrical and thermal conductivity. Most of binary transition nitride (MN_x form) and carbide (MC_x form) materials are FCC, which crystal structure is shown as in Fig. 2.1. The chemical stability of both transition metal carbide and nitride is also high. They are difficult to be attacked by acid (except oxidizing acid and hydrofluoric acid). Transition metal carbide (MC_x form) and nitride (MN_x form) are considered as the family of interstitial alloys or compounds. Non-metal atoms are randomly situated in the interstitial site.

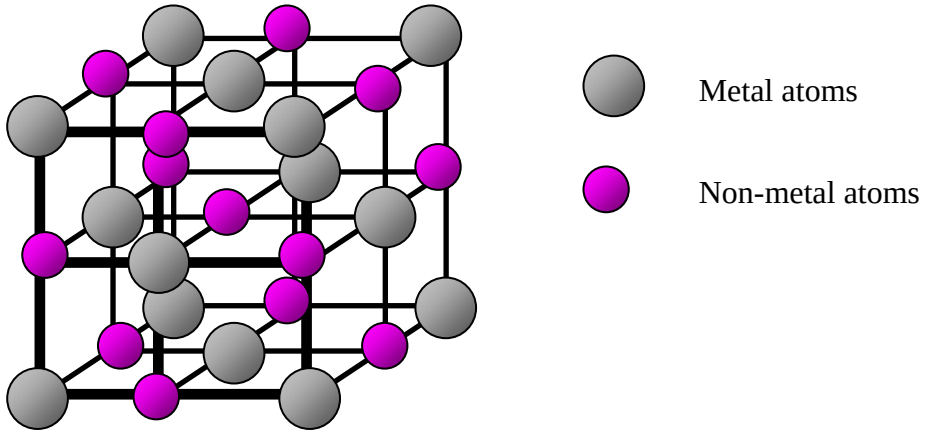

Figure 2.1: The face center cubic structure.

The properties of transition metal carbide and nitride using in this work are shown in Table 2.1.

Table 2.1: The properties of transition metal nitride and carbide for technical applications [16].

Compound	Lattice Parameter (nm)	Density (g cm^{-3})	Micro-hardness (GPa)	Melting Poing (°C)	Young's Modulus (GPa)	Electrical resistivity (μΩ cm)
TaC	0.4455	14.48	16	3,985	290	15
CrN	0.4148	6.14	13	1,770 Decomposes	450	640
ZrN	0.4570	7.32	15	3,000	460	24

Transition metal nitride (MN_x form) and carbide (MC_x form) contain the mixture of metallic, covalent and ionic component. The metallic component shows good electrical conductivities. Atomic orbital of atoms are combined to form bonding in covalent bond. The ionic can be formed by transferring the charges from the metal atom to non-metal atom. For preparation of the transition metal carbide and nitride, the thin films are grown by physical vapor deposition (PVD). The transition metal atoms are reacted with reactive gas ions from the plasma at low pressure then be sputtered from the target and forming thin film layer on the substrate.

2.2 Plasma

In general, plasma, consisting equal number of electrons and ions, are neutral. Plasma can be generated by external power supply. After a high voltage is applied to a metal electrode within a chamber, the primary electrons can be produced from the ionization of background gas. The ions in plasma move to bombard the negative cathode, whereas the electrons are accelerated across the sheath, a region with low electron density, into the plasma. If the electrons have enough energy, the ionization of neutral gas atoms can be occurred after collision between gas and electron. There are various collision processes that can occur within the plasma to generating and

sustaining plasma. If we consider energy conservation, there are 2 kinds of collisions: elastic and inelastic collision. In case of elastic collision, momentum and energy are conservation during the collision. Little energy can transfer from energetic electrons to the atoms or ions. On the other hands, in case of inelastic collision, energy can be lost during the collision. There are many inelastic processes in the plasma. One important process is ionization

$$e^- + Ar \rightarrow Ar^+ + 2e^- \quad (2.1)$$

This reaction creates another electron and ion. A second reaction is the excitation of atoms or ions into an excited state.

$$e^- + Ar \rightarrow Ar^* + e^- \quad (2.2)$$

An energy decay and emission of photon can be produced in this process. The lifetime of excited state is very short (in order nanosecond). However, excited inert gases have enough time to collide with ground state atoms. This phenomenon may cause excitation or even ionization.

$$A^* + B \rightarrow A + B^* \text{ (excitation)} \quad (2.3)$$

$$A^* + B \rightarrow A + B^+ + e^- \text{ (ionization)} \quad (2.4)$$

where A and B are arbitary species

Because plasma is conductive, the perturbation from electric field ($\vec{E}$) is very weak. A force of moving charge in electric field can be ignored. In contrast, the perturbation from magnetic field ($\vec{B}$) is strong.

A force of moving charge in magnetic field is

$$F_m = q\vec{v} \times \vec{B} \quad (2.5)$$

where q is the charge on the particle

v is the velocity

If the charged particle move at right angle to the magnetic field, the particle will move in an orbital path the radius of this orbit (r) is

$$r = mv_{\perp} / qB \tag{2.6}$$

where m is the mass of the particle

$v_{\perp}$ is the component of the velocity perpendicular to the magnetic field.

In general, the orbit of ion is larger than that of electron. The orbit of ion is always ignored because it is always much larger than the chamber. As the charged particle moves in electric field and magnetic field, the particle will drift cyclical motion. The direction is perpendicular to both electric field and magnetic field. This is shown in Fig. 2.2. This drift is known as $\vec{E} \times \vec{B}$

The drift velocity of charged particle in magnetic and electric field is

$$v = E / B \tag{2.7}$$

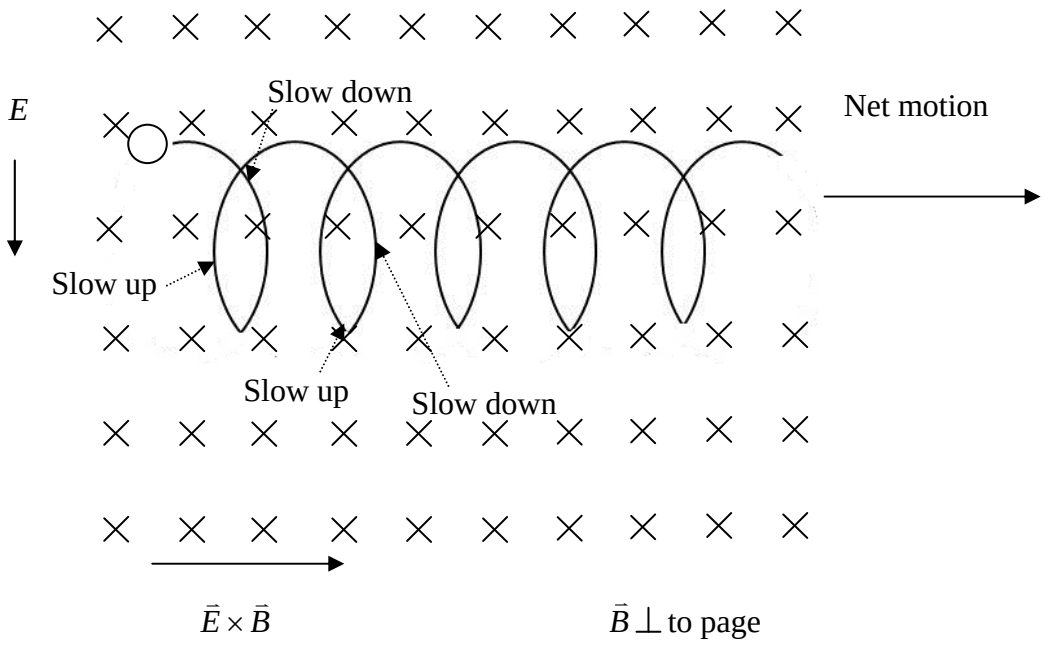

Figure 2.2: The motion of an electron in magnetic and electric field [17].

Because orbit of ion is larger, electron motion is only considered in this case. A spiral path of electron makes the path length of the electron increase many times comparing with straight line. This phenomenon makes the probability of collision between electron and other species increase and the density of ion and electron increase. In the case of circular planar magnetron in sputtering system used in the work, it consists of an array of magnets or electromagnetics and cooling water at the back of magnetron. Magnetron consists of 2 poles. The first pole is at the center of the magnetron. The second pole is an annular ring at the edge of the cathode. The magnetic field direction in a parabolic shape starts from the center pole to outer ring pole. The $\vec{E} \times \vec{B}$ drift forms a close path and is parallel to the surface of cathode, as shown in Fig. 2.3. As the ions bombard the cathode, the secondary electrons will be emitted from cathode. These electrons are trapped near the cathode and form a drifting, circulating current. It causes an increase in ionization and much denser plasma [17].

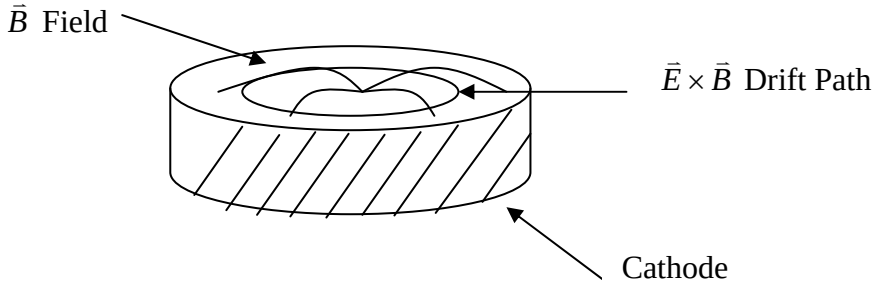

Figure 2.3: A circular planar magnetron cathode, showing the shape of magnetic field and the resulting drift path [17].

2.3 Sputtering

Sputtering is one of process for the deposition thin film. The target, the source of coating material, and substrate are placed into a vacuum chamber. The pressure is in the chamber in the range of $5x10^{-4}$ to $5x10^{-7}$ Torr. Generally, an inert gas, such as argon (Ar), is used in the process because of its inertness, its heavy mass and its low cost. After energetic particles especially ions of a heavy inert gas bombard the target,

the sputtered material is ejected from target surface in atomic form due to the momentum exchange. The substrates are in front of the target to receive the flux of sputtered atoms. Alloys and compound almost every element can be sputtered while the composition is kept constant. We can consider the sputtering deposition in both physical and chemical sputtering. In case of physical sputtering, energetic particles bombard the target atoms and transfer kinetic energy. If the surface of those atoms acquires enough energy to overcome the local binding force, they will be ejected from the target surface. In case of reactive sputtering, there are reaction between reactive ion and surface target to form an unstable compound. We can describe the atomic collision by using a simple binary hard sphere elastic collision, as shown in Fig. 2.4. The incident ion of mass M_i and velocity v_i impact on the target particle M_t. After elastic collision between bombarding ion and target, the target particle is moved deeper in the target by momentum exchange. If the bombarding ion and target particles are identical mass, the momentum transfer to the target is the maximum value. If the mass of the ions is less than that of the target particle, the bombarding particles will be reflected [18].

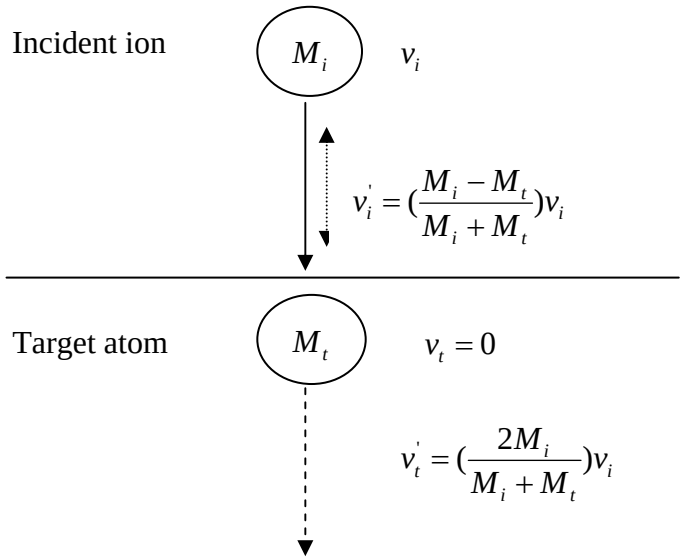

Figure 2.4: The momentum exchange process during sputtering [19].

In general, many phenomena can occur after the ion bombards the surface target, as shown in Fig. 2.5. This is known as collision cascade. There are 3 kinds of

materials that are emitted from the target after ion bombardment. The first is reflected ions and neutrals. The second is the secondary electron (electron from the target). The third is the ejected target atoms from the series of collisions. Moreover, ion implantation, the buried ions in the target, can occur. The last phenomenon is rearrangement in the target material. It includes missing atoms (vacancy), interstitial (atoms out of position) or a change in stoichiometry in target [19].

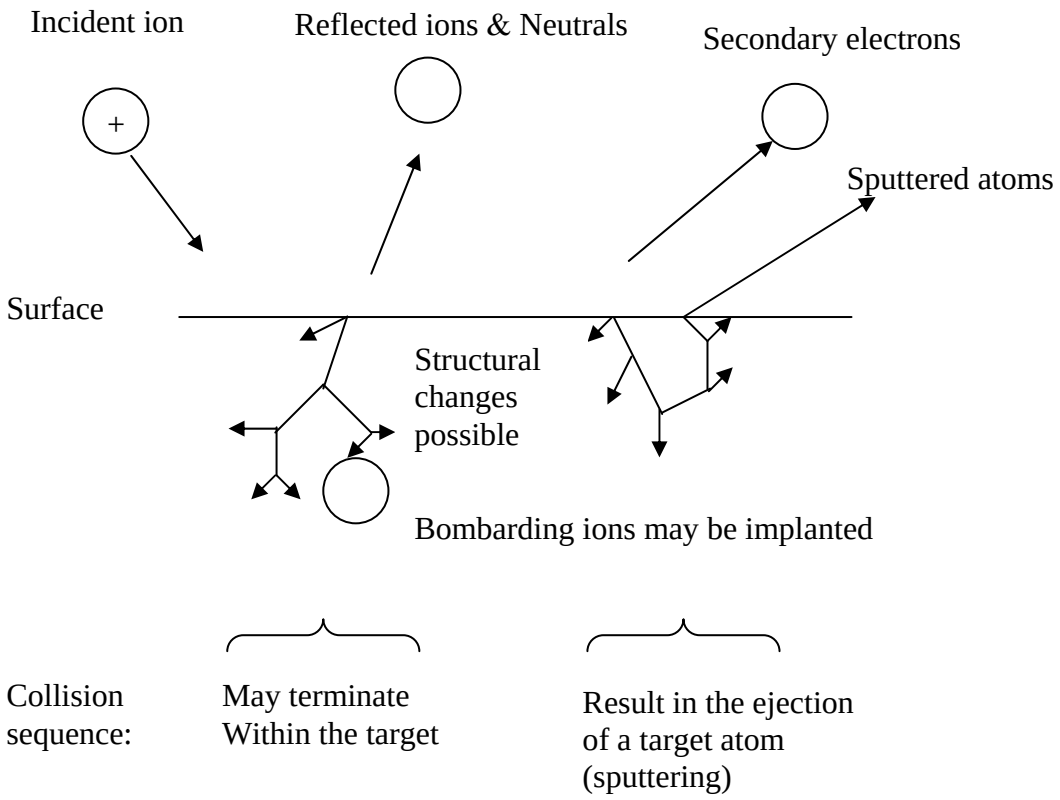

Figure 2.5: Interactions of ions with surfaces [19].

In reactive sputtering, compound thin film can be grown from metallic target by introducing reactive gas (N_2, O_2) and inert gas (Ar) in the vacuum system. In plasma atmosphere, the compound can form on the surface target from the reaction between ion of reactive gas and target. This phenomenon makes the deposition rate decrease because the binding energy of compound is higher than that of the metal target and the mass of reactive gas is less effective than Ar gas. If the partial pressure of reactive gas in the system increases, the coverage area of compound on target tends to increase. The deposited film changes abruptly from a metal to a nearly full-stoichiometric compound [18].

The bias sputtering is the specific process applying a negative voltage to the substrate. The positive ions are introduced to bombard the substrate during the sputtering deposition. In case of low energy ion bombardment (< 200 eV), the impurity species, having high sputtering yield, can be removed or otherwise the composition can change by ion bombardment. Moreover, the surface mobility of adatoms and grain size can be affected by low energy ion bombardment. The sputtering yield is an average number of target atoms ejected per incident particles. The diffusion of adatoms results from ion bombardment because adatoms gain energy from the ions. In case of high energy ion bombardment, the structure of films can be modified [18].

The energy of ions moving to bombard the substrate during growth film is very important parameter. The maximum ion energy is calculated from

$$E_i = e\left|V_s - V_p\right| \tag{2.8}$$

where V_s is substrate voltage

V_p is plasma potential

V_p can be extracted from “knee” in I-V graph. The floating potential can be determined when the current is zero. In this work, Langmiur’s probe has been used to determine the plasma parameters. There are two kinds of probes: flat probe and wire probe. Flat probe is used for measurement ion flux (J_{ion}) and floating potential. Wire probe is suitable for measurement the plasma potential. Negative voltage is applied to the flat probe for measurement the ion current. In contrast, positive voltage is applied to wire probe for measurement the electron current at the same position as the substrate [20].

2.4 Thin Film Process

There are 3 main steps for thin films deposition. The first step is the production of atomics, molecule or ionic species. The second step is the transportation these species to the substrate through the medium and the third step is the formation of a thin solid film on substrate. The following process for condensation on the substrate can be described: As the incident flux of film species impact the substrate, they transfer sufficient energy to the substrate. These species are absorped on the

surface substrate known as “adatom”. Adatoms can diffuse over the surface substrate because they still remain energy after impacting. Adatoms can also interact among themselves and form bigger clusters. If the clusters or the nuclei are unstable thermodynamic, they tend to leave the surface in time, depending on the interface between film and substrate materials and the substrate temperature. There is no desorption if the cluster collides with other absorbed species. This phenomenon make the cluster grow in size and more stable. The clusters become stable after they reach the critical size. The nucleation steps include the formation of stable, chemisorbed and critical-sized nuclei. This process is shown in Fig. 2.6.

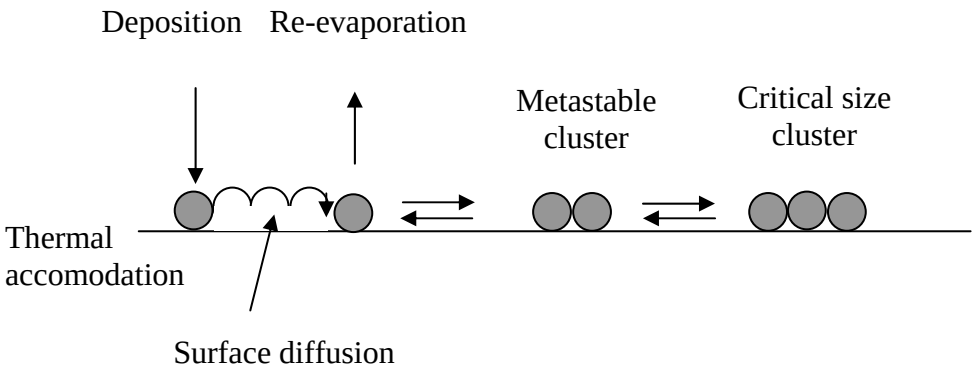

a) Nucleation

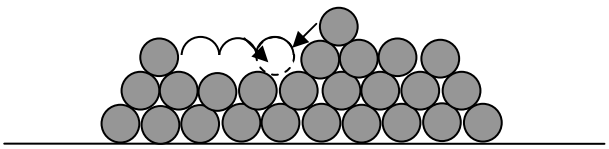

b) Layer growth

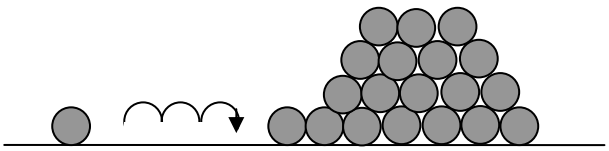

c) Island Growth

Figure 2.6: The schematic representation of nucleation process (a) the formation of layer growth (b) and the island growth (c) [21].

The number and size of critical nuclei increase until the saturation nucleation density. The nucleation density and average nucleus size depend on many parameters such as the energy of the impinge species, the rate of impingement, the activation energies of absorption and desorption, thermal diffusion, the temperature, topography and chemical nature of the substrate. The grown nuclei are called islands. The small islands start to coalescence with each other to reduce the surface area. This stage is called coalescence. The growth of larger island changes to form continuous film. For the growth process, there are 3 modes, as shown in Fig. 2.7: island, layer type and mixed type. Island growth or Volmer-Weber type can be occurred when the binding energy between adatoms is more than the binding energy between adatoms and substrate. This type can be occurred for metal film on insulator or contaminated substrate such as metal film on SiO_2. Layer by layer or Frank-van der Merwe type can be occurred when the binding energy between adatoms is less than or equal the binding energy between adatoms and substrate. This type can be found in case of metal film on metal substrate (Cd on W), metal film on semiconductor substrate (Fe on GaAS) and semiconductor film on semiconductor substrate ($Si_{1-x}Ge_x$ on Si). The mixed type or Stranski and Krastanow is combination of first two. After layer grows on the substrate, the island will be formed. This type is driven by the elastic strain energy (E_{strain})

$$E_{strain} \propto [\frac{(a_f - a_s)}{a_s}]^2 h \tag{2.9}$$

where a_f is the lattice constant of film

a_s is the lattice constant of substrate

h is the thickness of film

In this case, the lattice constant of film is larger than that of substrate. The strain energy has more effect than the surface energy which is the energy requirement to form island growth. The different islands are random crystallographic orientation and topography. During coalescence process, the islands contact each other. This phenomenon make grain boundary and various point and line defect occur into the films because of the mismatch of crystallographic and geometry.

There are 3 types structure of film depending on grain orientation. If the orientation of grain is random, the films show polycrystalline. However, if the grain size is approximate 1 nm, the films show amorphous. If the film has high deposition rate (in unit of atoms) or low deposition temperature, the adatoms do not have enough time to diffuse on the substrate. They are buried by the subsequently deposited atoms. Therefore, the amorphous film can be formed. In contrast, the films show single crystalline if the orientation grain parallel to each other [1, 21].

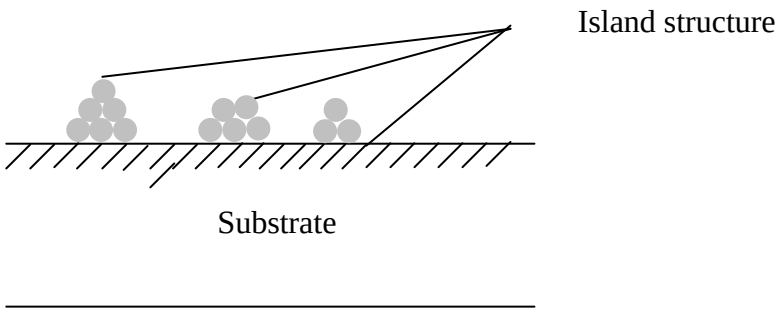

a) Volmer-Weber type

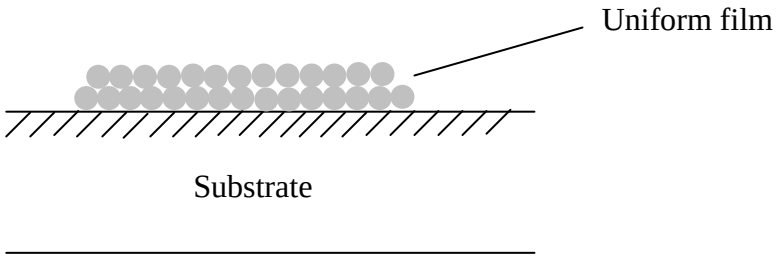

b)Frank-van der Merwe type

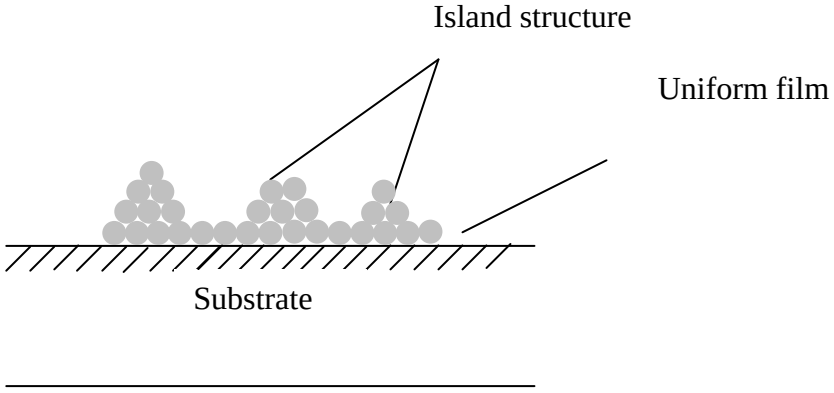

c) Stranski-Krastanov type

Figure 2.7: There modes of thin films growth process.

2.5 Evolution of Microstructure

There are 3 processes affecting the evolution of microstructure: surface diffusion, bulk diffusion and atomic shadowing. At elevated temperature, bulk diffusion can be occurred. Bulk diffusion is the process that adatoms incorporated into the coating. The adatoms can readjust the position within the lattice. A geometric interaction between the roughness of the growing surface and arriving atoms is called shadowing effect. The shadowing effect can be eliminated by surface diffusion at higher temperature. The different range of T/T_m (where T is the substrate temperature in absolute temperature and T_m is the coating melting point in absolute temperature) is the basis of structure zone model. The model for sputtering in the absence of ion bombardment is shown in Fig. 2.8.

The zone 1 structure can be occurred at low T/T_m (less than 0.3) when the adatoms is not enough energy to diffuse on surface and overcome the shadowing effect. The zone 1 presents the impurity such as oxygen. The roughness in zone 1is high because of tapered crystals or domed tops. The direction of domed tops is related the direction of arriving flux. The roughness can result from the shape of initial growth nuclei, preferential nucleation, substrate roughness and preferential growth. Due to the limited surface diffusion, it leads to porosity and form the column. The size of column can be very small and amorphous can be formed. The transition structure, zone T, shows the dense fibrous grain at higher substrate temperature. The adatoms have enough energy to overcome the roughness from substrate and initial nucleation. It makes films grow with smooth and high density. Grain coarsening can be occurred in the coalescence of small islands process.

However, the grain boundary cannot move during continuous film process. The crystalline is nearly random due to incomplete orientation selection. There are competition grain growths among neighboring grains especially (111) and (200) plane. The columnar structure can be developed to larger grain. This zone results from energetic particle bombardment. These particles occurring from magnetron source are ions and energetic neutrals. There are 2 ways that the neutral particle can be originated from the target. One is that positive ions neutralized and reflected from the target surface. Another way is that sputtered negative ions are accelerated and the

neutralized in the gas. The zone 2 is found when $0.3 < T/T_m < 0.5$. Adatoms have high surface diffusion than zone 1. The grain size in this region is increased as T/T_m increase. There is dense intercrystalline boundary between the columnar, platelet and whisker grain. The zone 3 can be occurred at high relative temperature $T/T_m > 0.5$. The bulk diffusion is dominated in this region. The structure can be columnar or equiaxed. Grain boundary can move in coalescence and growth film process. The recrystalline, the transformation of grain size distribution, can be occurred. The grain size becomes larger size [18, 21, 22].

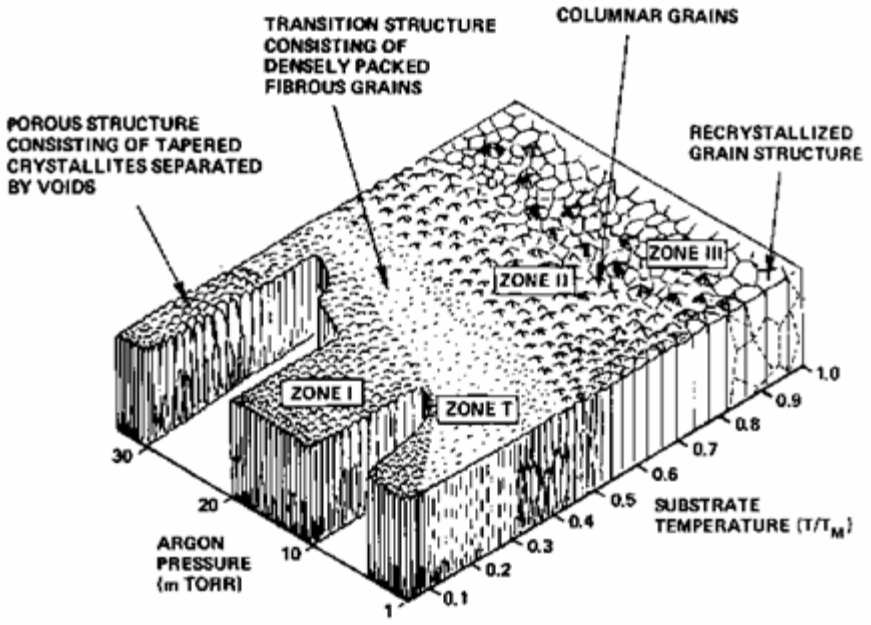

Figure 2.8: The structure zone model representation the effect of substrate temperature and argon working pressure on the structure of metal coating [18].

The grain size relates to the kinetic energy of adatoms to move on the surface. When the adatoms have high kinetic energy, the grain size tends to increase. The grain size can be also modified after deposition by annealing. As the annealing temperature increase, the grain size trends to increase due to high activation energy process of thermal diffusion.

The roughness of films depends on the nucleation barrier of the substrate. In case of low nucleation barrier and high nucleation density, the size of critical nucleus is small; therefore, the films become fined grain and smooth. In contrast, if the size of critical nucleus is large due to the large nucleation barrier, the film becomes coarse-grain rough film. When the adatoms have enough energy to move on the surface, the roughness will decrease.

The adhesion between films and substrate depends on the chemical nature, cleanness, and the surface substrate. The higher value of kinetic energy of incident species, adsorption energy of the deposited film and initial nucleation density make the adhesion of film be better. The contamination on the substrate may cause either an increase or a decrease in adhesion. It depends on either an increase or a decrease in the absorption energy, respectively. The adhesion can be improved by using fined-grain substrate or pre-coat with suitable material.

The lattice constant of thin film is different from the lattice constant of bulk. It can be either an increase or a decrease value. It depends on either negative value or positive value of surface energy [1].

2.6 Hard Coating Material

Hard coating materials can be used for increasing the tool life, reducing the manufacture cost, improving the quality of product in many applications such as dies, cutting tool and mold. The hardness of materials is very important properties of hard coating. The hardness can be defined as the resistance of plastic deformation. The hardness of hard materials is between 20 to 40 GPa. If the hardness is above 40 GPa, the materials is defined as “superhard material” If the hardness is above 80 GPa, the materials is defined as “ultra-hard materials”. In metal and alloy films, the mobility of dislocation is eliminated when the grain size is decreased. The obstruction of dislocation mobility affects an increase in the hardness of materials. The relation between the hardness and grain size according to Hall-Petch [23] is shown in (2.10)

$$H = H_o + \frac{k}{\sqrt{d}} \tag{2.10}$$

where H is the hardness

H_o is the intrinsic hardness of single crystal

d is the grain size

k is the materials constant

The grain size affects the hardness when the grain size is more than approximately 10 nm. If the grain size is less than 10 nm, there are a lot of defect in the grain boundary, causing the fast diffuse atoms in this region. In this case, the hardness can be decreased because of the grain boundary sliding. Most hard coating can be found in the binary transition metal nitride, carbide and boride compound such as TiN, CrN, TaC and BN. The outstanding bond in hard coating is covalent bond but there is still ionic and metal bond in nitride and carbide compound. For harder materials have higher cohesive energy, shorter bond length and higher degree of covalent bond. For the hardest material, the hardness of diamond is around 70-100 GPa. It consists of pure covalent bonding.

The hardness of binary compound can be improved by an addition an element in binary compound. It's called "ternary compound". Some atoms can be substituted by another atom with different size. This phenomenon makes the strain occur in the crystal and cause an increase in hardness. The adhesion is also importance properties of hard coating. The adhesion is defined as the condition that the substrate and film can be held together. This adhesion of films can be tested by perform a scratch test. The adhesion between film and substrate can be improved by preparing the cleaning surface of substrate, using the interlayer. The increase in roughness of substrate can also improve the adhesion [22, 24-25].

2.7 Metal Oxide Semiconductor Technology

A metal gate and high-k dielectric can be deposited into the metal oxide semiconductor field effect transistor (MOSFET) process using a gate-first or gate-last approach. The difference between 2 approaches is the step of deposition either before or after the source/drain activation anneal. The procedure of gate-last process or the replacement gate process is shown in Fig. 2.9. The source and drain are fabricated by a high temperature process, following by the final process - the gate fabrication. A "dummy" SiO_2/polysilicon gate stack is deposited. This process follows source/drain implant, source/drain high-temperature rapid thermal anneal (RTA) and source/drain

silicide formation. After that an additional dielectric layer is deposited and resurfaced by chemical-mechanical polish (CMP), stopping at the top of dummy gate. After CMP process, the dummy gate is removed and then final high-k and metal gate are deposited. The metal gate between the gate stack is removed by CMP and stopped at the top of high-k layer. Finally, the contact and metal layer complete the process. The gate-last process was then annealed in a low temperature process after high-k and metal stack are formed. The properties of dielectric and metal gate will be similar the intrinsic value in the gate last process [26].

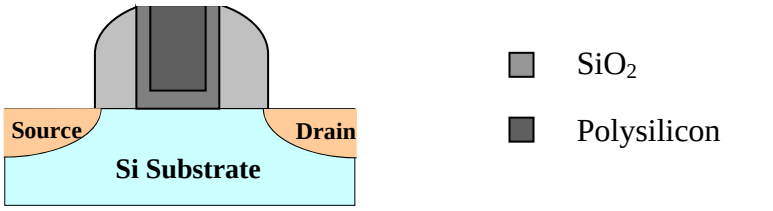

a) Fabrication Polysilicon/SiO_2 CMOS and CMP to expose gap

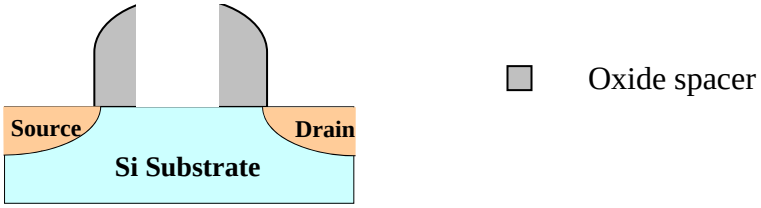

b) Remove Polysilicon/SiO_2

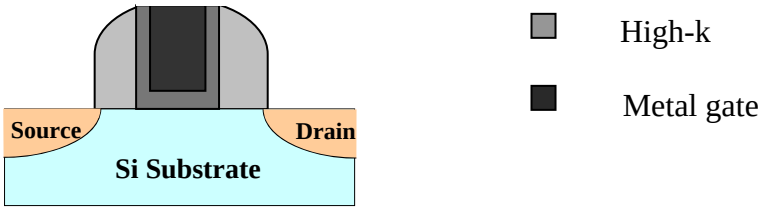

C) Deposite high-k and metal gate

Figure 2.9: Schematic process of gate-last process [26].

2.8 Ideal Metal Oxide Semiconductor

The cross section of MOS capacitor is shown in Fig. 2.10. It consist of conducting gate electrode (metal or heavily doped polysilicon), oxide layer and semiconductor substrate.

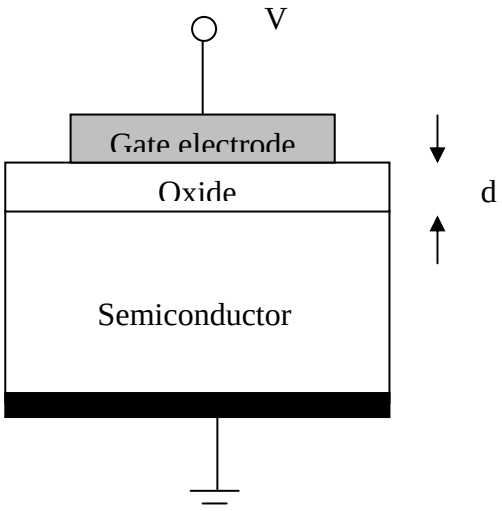

Figure 2.10: The schematic representation the MOS structure [27, 28].
where d is the thickness of insulator and V is the applied voltage

The capacitance of oxide layer depend on the thickness and area of the film

$$C = \frac{k\varepsilon_o A}{d} \tag{2.11}$$

where C is the capacitance

ε_o is the permittivity of free space

A is the capacitor area

d is the dielectric of oxide film

k is the dielectric constant

SiO_2 is commonly used in MOS gate electrode as an oxide layer. The energy-band diagram of ideal MOS structure without applied voltage is shown in Fig. 2.11. In ideal MOS, there is no current flow in the structure when the resistivity is infinite. Moreover, the difference work function between the metal and semiconductor is zero.

The band is flat when the voltage is not applied. This is called “The flat-band condition” [27].

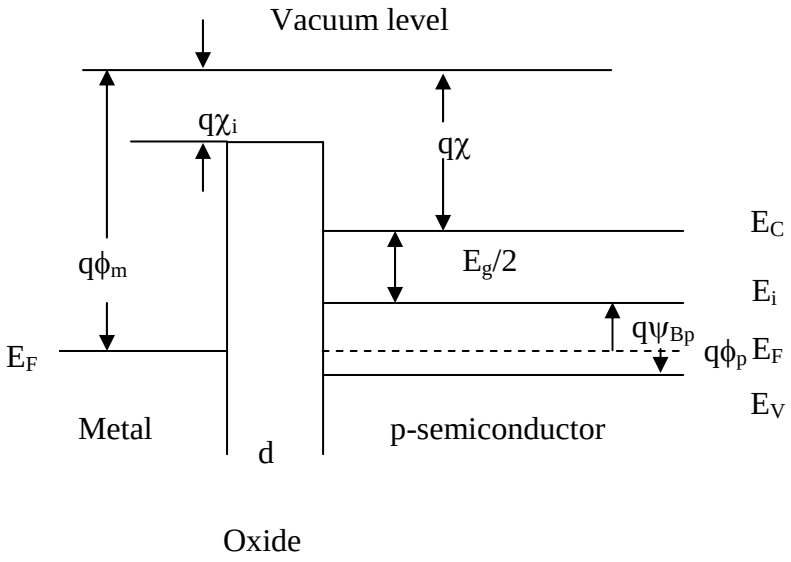

Figure 2.11: The energy band diagram of ideal MOS without bias voltage in p-type semiconductor [27].

where χ is the electron affinities of semiconductor

χ_i is the electron affinities of oxide layer

ψ_{Bp} and ϕ_p is the Fermi potential with respect to the midgap and bandedge, respectively

E_g is the energy band gap of semiconductor

ϕ_m is the metal work function

When an ideal MOS capacitor is biased with positive or negative voltage, the energy band will bend as shown in Fig.2.12. For the p-type semiconductor, the valence band edge (E_v) bends upward and is closer to the Fermi level when a negative voltage is applied to the metal plate. In the ideal case, there is no current flow in the structure; therefore, the Fermi level remains flat in the semiconductor. The band bending causes the accumulation of holes (majority carrier) near the semiconductor surface. It’s called “accumulation”. The bands bend downward and the holes are depleted if a small positive voltage is applied. It’s called “depletion”. The bands bend

even more downward if the larger positive voltage is applied. In this case, the intrinsic level E_i is the crosses over the Fermi level E_F. In this case, the number of electrons (minority carrier) is larger than that of holes. This case is called “inversion”. The total capacitance, C, in the system is the series combination of oxide capacitance and semiconductor depletion-layer

$$\frac{1}{C} = \frac{1}{C_o} + \frac{1}{C_D} \tag{2.12}$$

where C_o is the oxide capacitance

C_D is the semiconductor depletion layer capacitance

For the thickness of oxide layer (d), the constant capacitance is C_o, relating the maximum capacitance in the system. The semiconductor capacitance depend not only the bias voltage but also the measurement frequency.

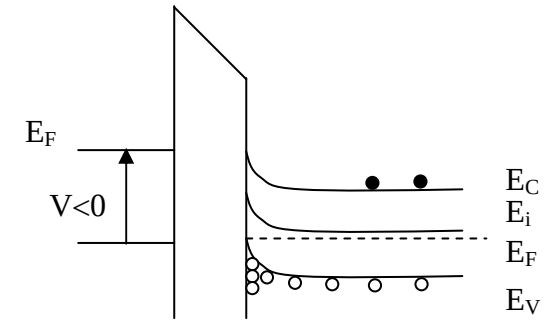

a) accumulation

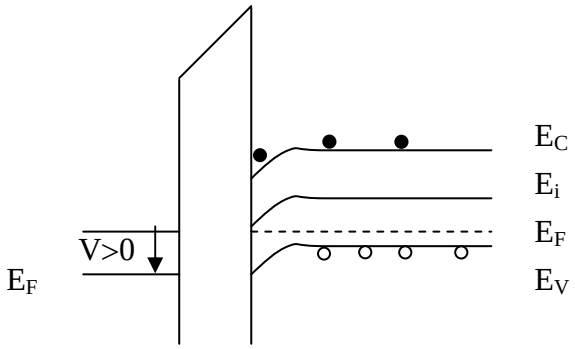

b) depletion

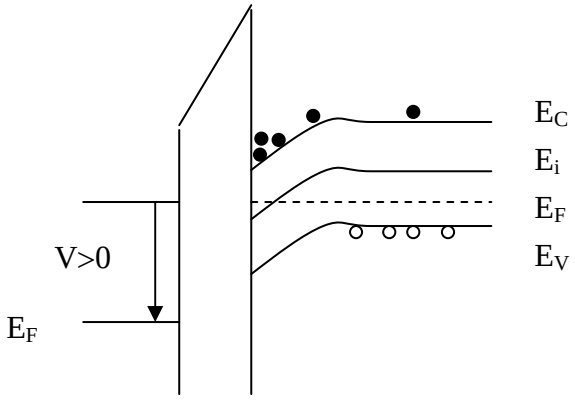

c) inversion

- Electrons
- Holes

Figure 2.12: The energy-band of MOS structure after applying the bias voltage in case of a) accumulation b) depletion c) inversion [27].

In basic MOS capacitor, it consists of the single crystal silicon, monolayer of SiO_x incomplete oxide silicon, a thin amorphous SiO_2 and metal gate, as shown in Fig. 2.13. There are 4 kinds of charges in MOS capacitors 1) trapped charges Q_{it}, which are at the interface between Si-SiO_2. These charges can be produced by excess silicon, broken Si-H, excess oxygen and impurity. 2) Fixed charges, which are near the interface. These charges cannot move under electric field ($\vec{E}$) 3) Oxided trapped charges can be created inside oxide layer 4) Mobile ionic charges Q_m are mobile within the oxide. The oxide charges, including the fixed charged, the oxide trapped charges and the mobile ionic charges don't depend on the bias. They make the flatband voltage shift as shown in Fig. 2.14.

The voltage shift value depends on the location of charges. If the location is closer to the interface between oxide-semiconductor, it makes the more shift of voltage. As the positive charges appear inside the oxide layer, it added positive gate bias for the semiconductor. A more negative gate bias is applied for the same original semiconductor band bending. The fixed oxide positive charge, Q_f, located near the interface between Si-SiO_2 interface. The thickness of oxide films or the concentration of impurities in the Si doesn't affect the density of fixed charge. The number of fixed charge depends on the oxidation, annealing condition and silicon surface orientation. The excess silicon (trivalent) or the loss of an electron from excess oxygen near the Si-SiO_2 interface is the origin of fixed charge. Mobile ionic charges can move inside the oxide layer, depending on the bias condition. It also causes the voltage shift.

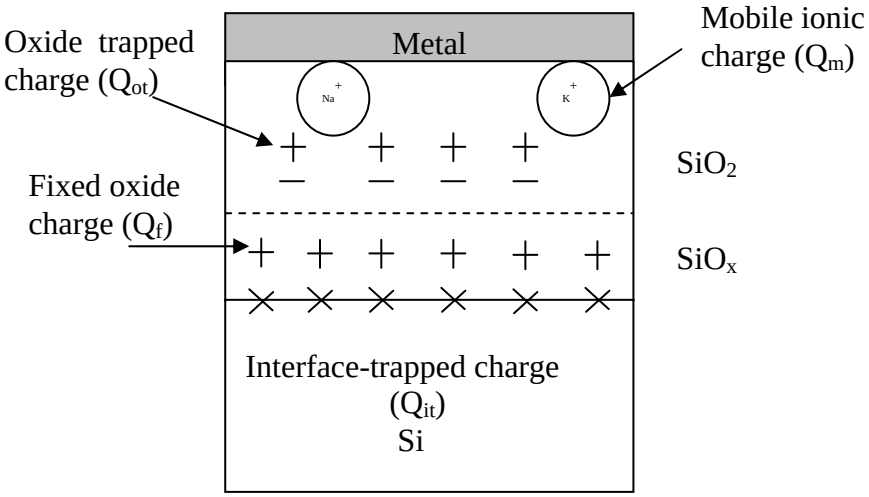

Figure 2.13: The basic classification of charges in MOS capacitor [27].

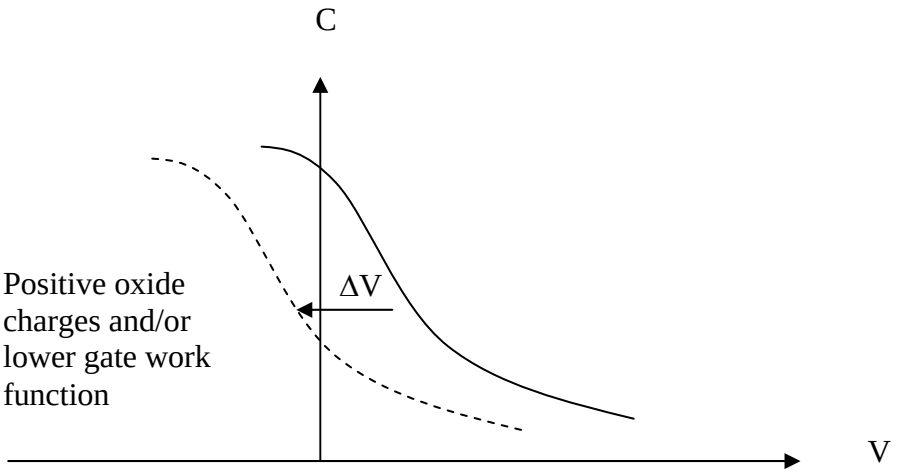

(a)

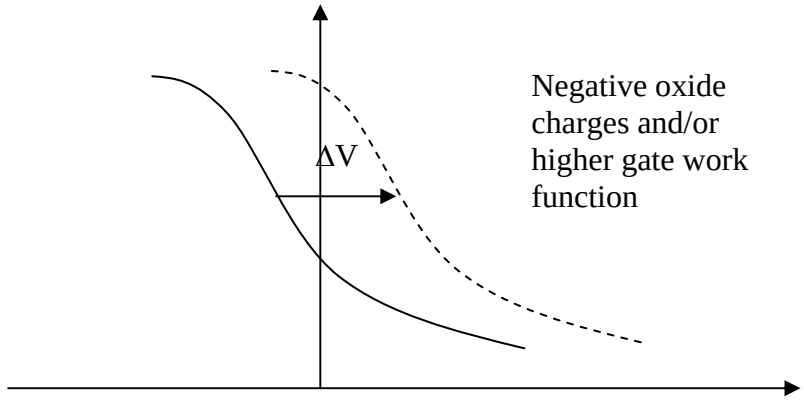

(b)

Figure 2.14: High frequency C-V curve on p-semiconductor shifted the voltage axis due to (a) the positive oxide charges (b) the negative oxide charges [27].

The work function difference between p-type semiconductor and metal gate is shown below

$$\phi_{ms} = \phi_m - (\chi + \frac{E_g}{2q} + \psi_{Bp}) \tag{2.13}$$

If the work function difference (ϕ_{ms}) is not zero, C-V curve will be shifted by the same amount in gate bias, as shown in Fig.2.14.

The net flat band voltage is

$$V_{FB} = \phi_{ms} - \frac{Q_f + Q_m + Q_{ot}}{C} \tag{2.14}$$

$$\Delta V = -\frac{Q_f + Q_m + Q_{ot}}{C_o} \tag{2.15}$$

where Q_f is fixed charge

Q_m is the effective net charge of mobile ionic ion per unit area

Q_{ot} is the effective net charge of the oxide trapped charge per unit area at the Si-SiO_2 interface.

ΔV is the voltage shift due to the oxide charge

The flat-band voltage is the applied voltage to MOS structure. It makes no band bending in the semiconductor, as shown in Fig. 2.15. There is no field in three materials. In this case, the work function of metal is less than that of semiconductor. The flat band condition can be occurred after applying the negative gate voltage $-(\phi_s-\phi_m) \cong \phi_{ms}$, called flat band voltage with respect to the Fermi level of p-type substrate [28].

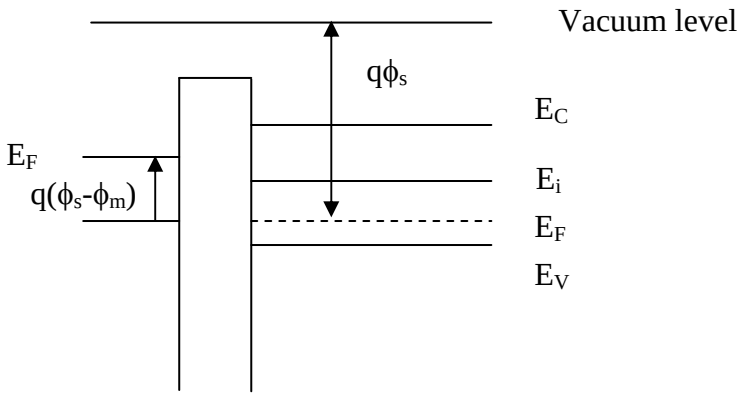

Figure 2.15: The energy-band diagram of a MOS capacitor at flat-band [28].

For ideal MOS, there is no conduction of insulator. If there is enough high temperature or high electric field, the electric field in insulator or oxide layer can be occurred. The electric field can be estimated in the oxide film after applying bias voltage (V) as shown

$$E_o = E_s \frac{\varepsilon_s}{\varepsilon_o} \approx \frac{V}{d} \tag{2.16}$$

where E_o and E_s are the electric field in the oxide film and semiconductor

ε_s .and ε_o are the permittivity in the semiconductor and oxide film, respectively.

The tunneling effect is the most common conduction mechanism under high electric field. The electron wave function can pass through the oxide film from metal to semiconductor. This phenomenon depends on the applied voltage causing the gate leakage [27-29].

To improve the performance, the drain current needs to be increased in MOSFET structure. One method is an increase in the capacitance. For increasing the capacitance, the dimension of oxide layer is reduced to 1 nm. It makes the leakage current in CMOS as the SiO_2 is a oxide layer. An alternative way for reduction the thickness of oxide layer is to use a gate insulator with a higher dielectric constant more than 3.9. This solution can reduce the leak current and improve the reliability of the device. By using equivalent oxide thickness concept (EOT), the capacitance per unit area is kept constant as the same as SiO_2 gate dielectric.

$$EOT = \frac{k_{SiO_2}}{k_x} t_x \tag{2.17}$$

where k_{SiO_2} is the dielectric constant of SiO_2 (3.9)

k_x is the high dielectric constant of alternative oxide layer

t_x is the physical thickness of alternative oxide

Therefore, the thickness of high-k dielectric material can be grown thicker than SiO_2 whereas the EOT is kept constant. For example, the thickness of the alternative oxide films with a dielectric constant 16 can be approximately fourth times as thick as SiO_2 film. The requirements for new high dielectric constant material are: the dielectric constant should be in the range of 10 to 30 to maintain a higher capacitance. The band gap should be more than 5 eV to avoid the leakage current. Moreover, thermal stability is importance. Oxygen diffusion coefficient has to be low value to prevent the formation of interfacial layer. Hafnium oxide (HfO_2) (k~20) and

Hafnium silicate ($HfSiO_x$) (k~16) are one choice for high-k dielectric. They don't react with Si and metal gate. Hf-based are mass production in both Intel and IBM company.

Another way to improve the capacitance is using the metal gate instead of polycrystalline silicon electrode in CMOS technology. If the ionized impurity in polycrystalline silicon is not high enough, the depletion of polycrystalline silicon can be occurred near the oxide layer. This phenomenon makes the total capacitance decrease. Metal gate is suitable to be used for avoiding the gate depletion because metal gate has high carrier concentration. The selection of metal gate is based on the the desired effective work function for negative metal oxide semiconductor (NMOS) and positive metal oxide semiconductor (PMOS). The effective work function has to be near the conduction band edge (4.1 eV) and valance band edge (5.2 eV) of silicon, respectively [12, 30-31]. The diagram of modern MOS structure is shown in Fig. 2.16.

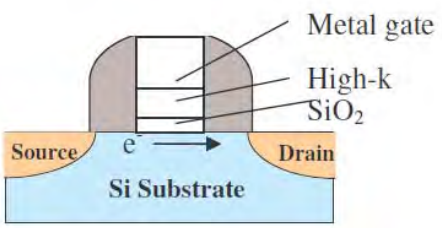

Figure 2.16: Schematics of SiO_2/ high-k/metal gate stack.

Threshold voltage is the voltage applied to gate to form the inversion layer or channel in Si substrate. The formation of inversion layer after applied voltage in Si allows the electron flow from the source to drain. It's called "drain current". Low value of threshold voltage (~0.2 V) is essential for high performance in CMOS technology. The SiO_2 layer is importance layer to permit the low trap density (dangling bond) and this layer enhances the electron mobility. Metal gate need to thermal stable after annealing at high temperature to maintain the stable gate stack [30-31].

Dipole can be occurred in the interface between HfO_2 and SiO_2 due to the fixed charge in the oxide layer. This dipole causes the mobility reduction in inversion layer [33-34], as shown in Fig. 2.17.

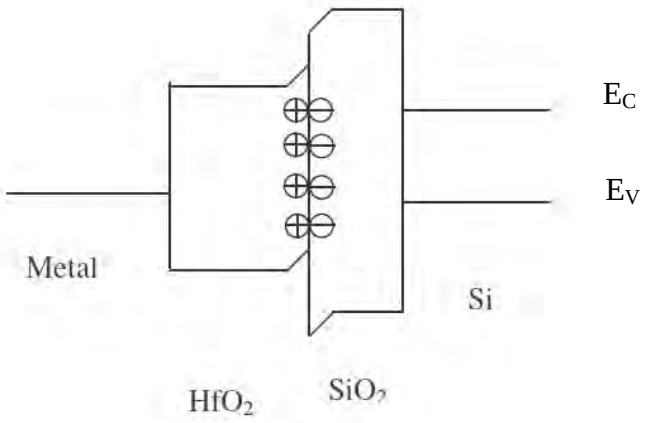

Figure 2.17: The energy band diagram of $Si/SiO_2/HfO_2$/Metal gate with the dipole at the SiO_2/HfO_2interface [32].

CHAPTER III
CHARACTERIZATION METHOD

3.1 X – Ray Diffraction

X – Ray diffraction (XRD) is a non-destructive technique for analysis crystal structure, lattice parameter, crystallizes size. The basic schematic diagram of X-ray diffraction is shown in Fig. 3.1. According to Bragg's law, a monochromatic X-ray with specific wavelength (λ= 1.5406 A) is incident on the lattice plane inside the sample at an angle theta (θ) and then, the beam is diffracted toward the detector. The constructive wave interference can occur if the path difference between the ray scattered from the top plane and bottom plane is equal to $2d\sin\theta$, as shown in Fig. 3.2.

$$2d\sin\theta=n\lambda, \tag{3.1}$$

when *d* is a spacing between atomic planes in the crystal,

λ is wavelength of x- ray beam,

θ is the Bragg angle for an incident angle as same as a diffracted angle.

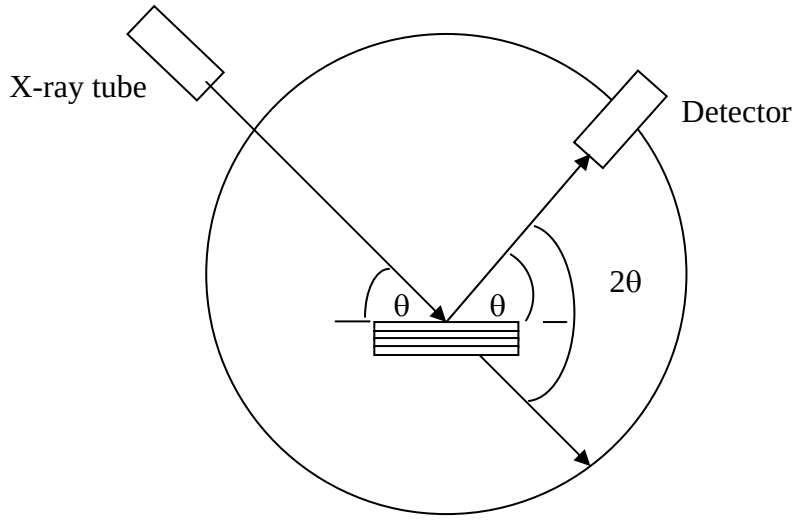

Figure 3.1: The x-ray spectrometer [34].

The sample is fixed while the x-ray tube and detector move in the same direction. The result shows the relationship between the intensity of the diffracted x- ray and the Bragg's diffraction angle (2θ). The crystal structure and the preferred orientation can be determined by this mode of measurement [35-36].

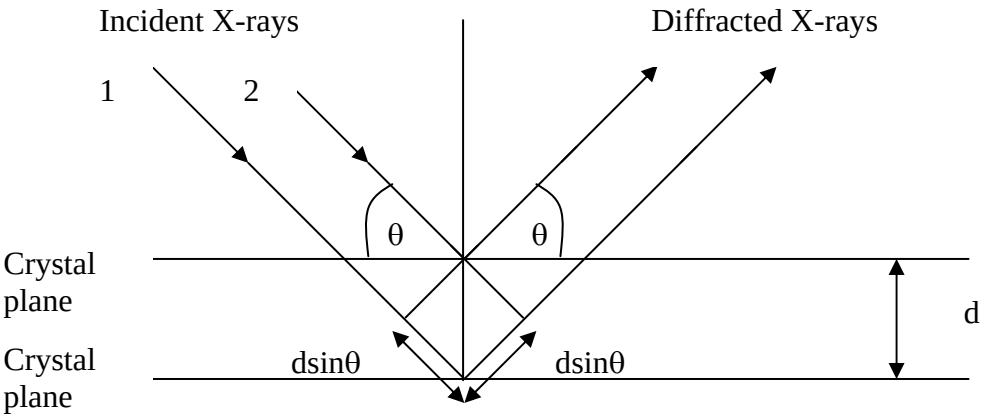

Figure 3.2: Diffraction of X- ray from parallel planes in the crystal followed by Bragg Law [36].

For the cubic structure with lattice parameter a , the relation between interplanar spacing d_{hkl} of planes labeled by Miller indices (hkl) and the lattice parameter (a) is

$$d_{hkl} = \frac{a}{\sqrt{h^2 + k^2 + l^2}} \tag{3.2}$$

where d is the distance between adjacent plane in the set (hkl)

h,k,l are the integer number

In the case of powder and columnar structure thin film, the grain size or column width can be estimated from Scherrer's formular, showing in

$$t = \frac{0.9\lambda}{B\cos\theta} \tag{3.3}$$

where t is the grain size

B is the width, in radian, the full width at half maximum of FWHM

3.2 Atomic Force Microscope

Atomic force microscope (AFM) is useful technique for the image and surface information. The limitation factor of AFM is that the roughness of surface sample cannot be high value. The resolution of image is eliminated by the shape and size of the tip. The equipment consists of the Si tip locating at the end of cantilever. The force of cantilever (F) is proportional the deflection of the end of cantilever(x), obeying Hook's law (F=kx). While the tip scans over the surface, there is van der waals force between the sample surface and a tip on cantilever. In this work, the non-contact mode - "*Tapping mode*^{TM}" is used because of less damage from the contact between the sample and tip. A Si tip slightly taps on the sample surface during scanning with a feedback loop. Fig. 3.3 shows the major component of AFM. The sample is scanned on the piezoceramic material such as lead zirconium titanate (PZT), changing the shape after applying voltage. The piezoceramic material can move in 3 axes: x, y and z. The deflection of cantilever can be measured by using the laser signal reflected from cantilever to a photodetector. Then, the deflection is used to determine how the feedback loops to control the constant deflection cantilever and force. The signal is transformed to be a surface image. In this mode, the oscillation amplitude of the cantilever is constant. It makes the interaction between tip and surface is constant. Almost all samples, including insulators, semiconductors and conductor can use AFM to obtain images. The root mean square (RMS) surface roughness can be obtained from AFM analysis [37].

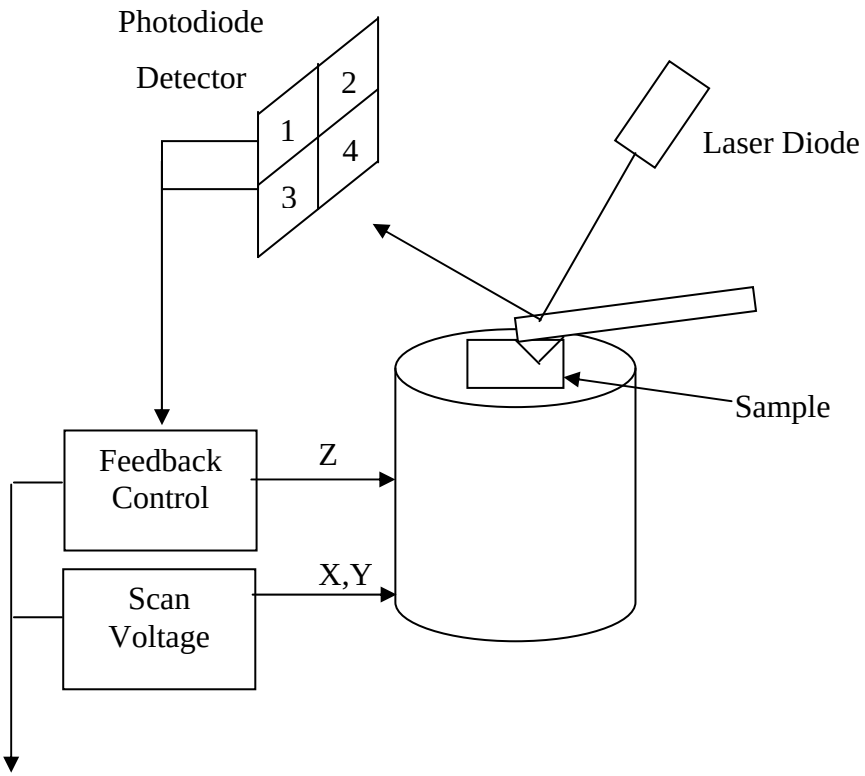

Figure 3.3: The schematic representation of the major components of an atomic force microscope [37].

RMS roughness is a standard deviation of the surface height within a given area [38].

$$RMS = \sqrt{\frac{\sum_{i=1}^{N}(z_i - z_{ave})^2}{N}} \tag{3.4}$$

where Z_{ave} is the average surface height within the given area,

Z_i is the current surface height,

N is the number of point within a given area.

3.3 Scanning Electron Microscopy with Energy Dispersive X-ray Analysis

In Scanning Electron Microscope (SEM) with electron probe microanalyzer, a primary electron beam bombards a specimen in the vacuum. Many signals are produced as a result of interaction between the primary electrons and the specimen such as secondary electrons, backscattered electrons, transmitted electrons, X- ray, cathodoluminescence and Auger electrons, as shown in Fig. 3.4. These signals can be used for investigation many properties of samples such as composition, surface topography and crystallography. The signal of secondary electrons and backscattered electrons are interested to obtain the topography. The secondary electrons can be occurred near the beam's impact area. In the electron probe microanalyzer (EPMA) or the electron microscope, the characteristic x-ray emitting after electron bombardment are interesting to obtain the composition information. As in Fig. 3.5, it shows the process after incident electron bombardment. Although SEM lacks of 3 dimensional sections, the information of SEM is better resolution than light optical instrument. Moreover, the elemental analysis information of SEM cannot be obtained from light microscope. The modern SEM, it can have a resolution in the nanometer range as close to transmission electron microscopy (TEM). However, this kind of SEM has more advantage than TEM that the specimens don't need to be thin enough to transmit electron. In some cases, SEM is better to obtain topography than AFM, where probe interaction is hard to control. The resolution in the vertical direction is much poorer than AFM.

The diagram of SEM consist of the electron column (electron gun and two or more electron lenses in vacuum system, as shown in Fig. 3.6. Electrons are generated from electron gun and they are accelerated in the range up to 40 keV. Electron lenses can be used for reduction the beam diameter of electron to generate a sharp image at high magnification and focus on specimen. When electron beam interact with the surface of specimen in 1 μm depth, signal can be generated to form an image requiring a scanning point by point. The interaction between electron beam and surface of specimen can be divided into 2 classes: elastic and inelastic scattering. In elastic scattering, there is no losing energy. The electron backscattering forming the image in SEM can be occurred in this case. In contrast, the energy can transfer from

electron beam to the atoms of the specimen in inelastic scattering leading to generate secondary electron, auger, x-ray, cathodolumines (long wavelength electromagnetic radiation in the visible ultraviolet and infrared), lattice vibration (phonon) and electron oscillation in metal (Plasmon) [39-40].

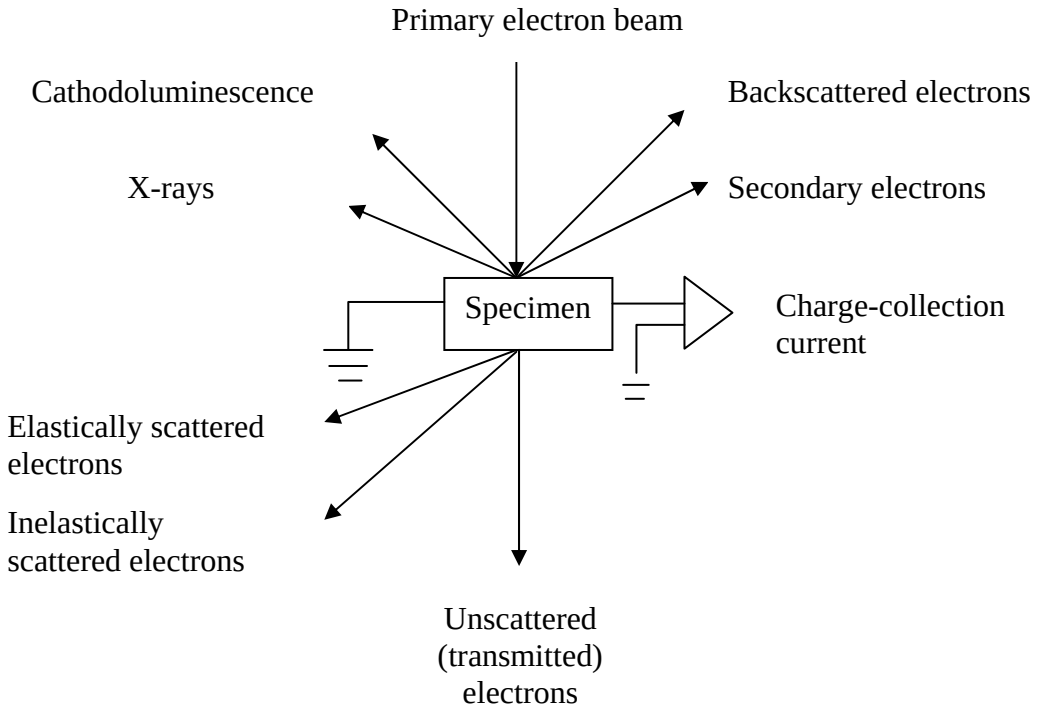

Figure 3.4: Photon and charged particle emission from an electron-bombarded surface [39].

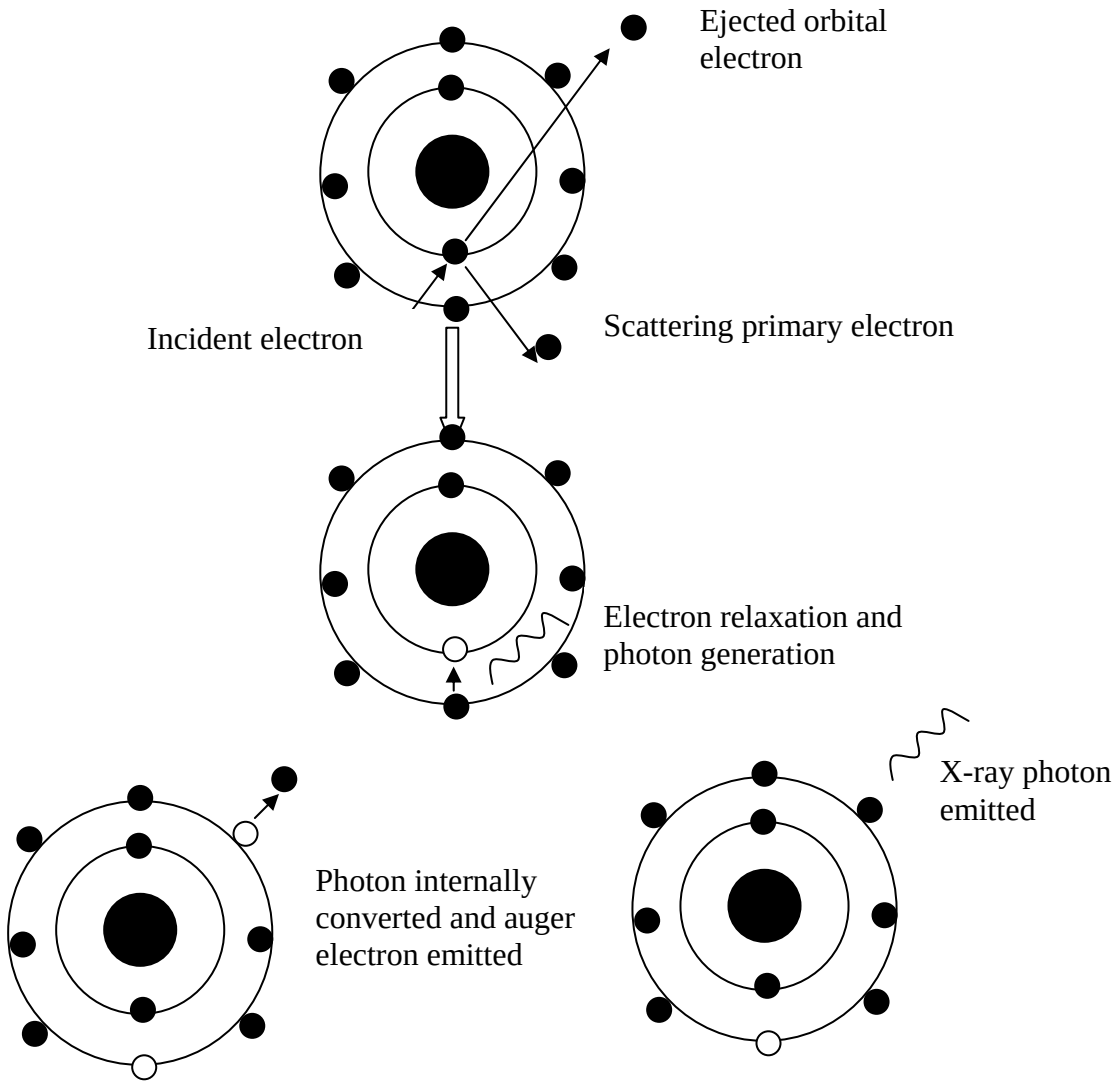

Figure 3.5: Schematic illustration of the process after incident electron bombardment [40].

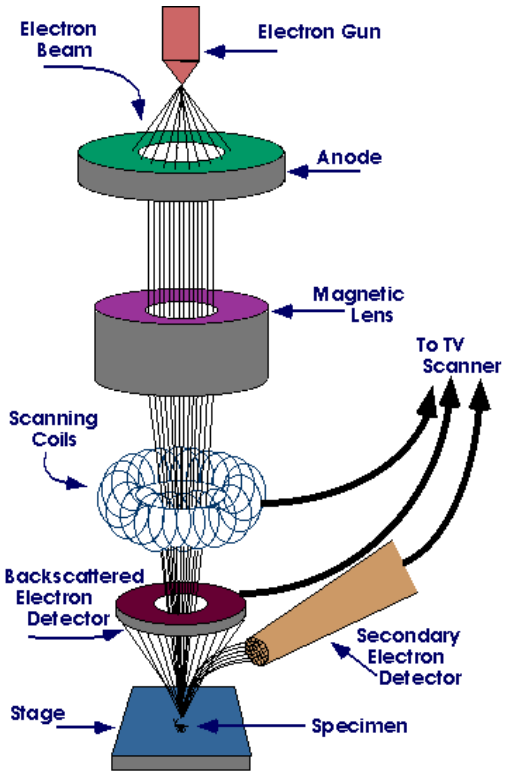

Figure 3.6: Schematic representation the major component of scanning electron microscope [41].

In this work, the chemical composition of the specimens is determined by X-ray spectroscopy (EDS or EDX). The concentration of each element affect the intensity generated for each element in the specimen. However, it's difficult to calculate the composition specimen directly from the intensity because absorption and x-ray fluorescence phenomena can be occurred. There are many factors relating to the atomic species, atomic number (Z_i), x-ray absorption (A_i) and x-ray fluorescence (F_i). For calculation the weight fraction of the element i, the common formula is

$$\frac{C_i}{C_{(i)}} = [ZAF]\frac{I_i}{I_{(i)}} \tag{3.5}$$

where C_i is the weight fraction of the element i

$C_{(i)}$ is the weight fraction of I in the standard

$\frac{I_i}{I_{(i)}}$ is the basic experimental measurement that underlies all quantitative x-ray microanalysis [40].

3.4 Transmission Electron Microscopy

The transmission electron microscope (TEM) is a powerful tool for the microstructural characterization. Although the diffraction pattern in x-ray method is more quantitative than electron diffraction pattern, the electron can focus easily more than x-ray diffraction. As seen from Fig. 3.7, it shows the ray diagram for making image in conventional TEM. The back focal plane consists of the diffraction pattern of sample. The objective aperture, a tiny hole in a plate, located at back focal plane to select the ray. If the objective aperture is located to pass only the transmitted electron (un-diffracted), a bright field image (BF) can be formed. If the aperture is located to pass only some diffracted electron, a dark field image (DF) can be formed [36].

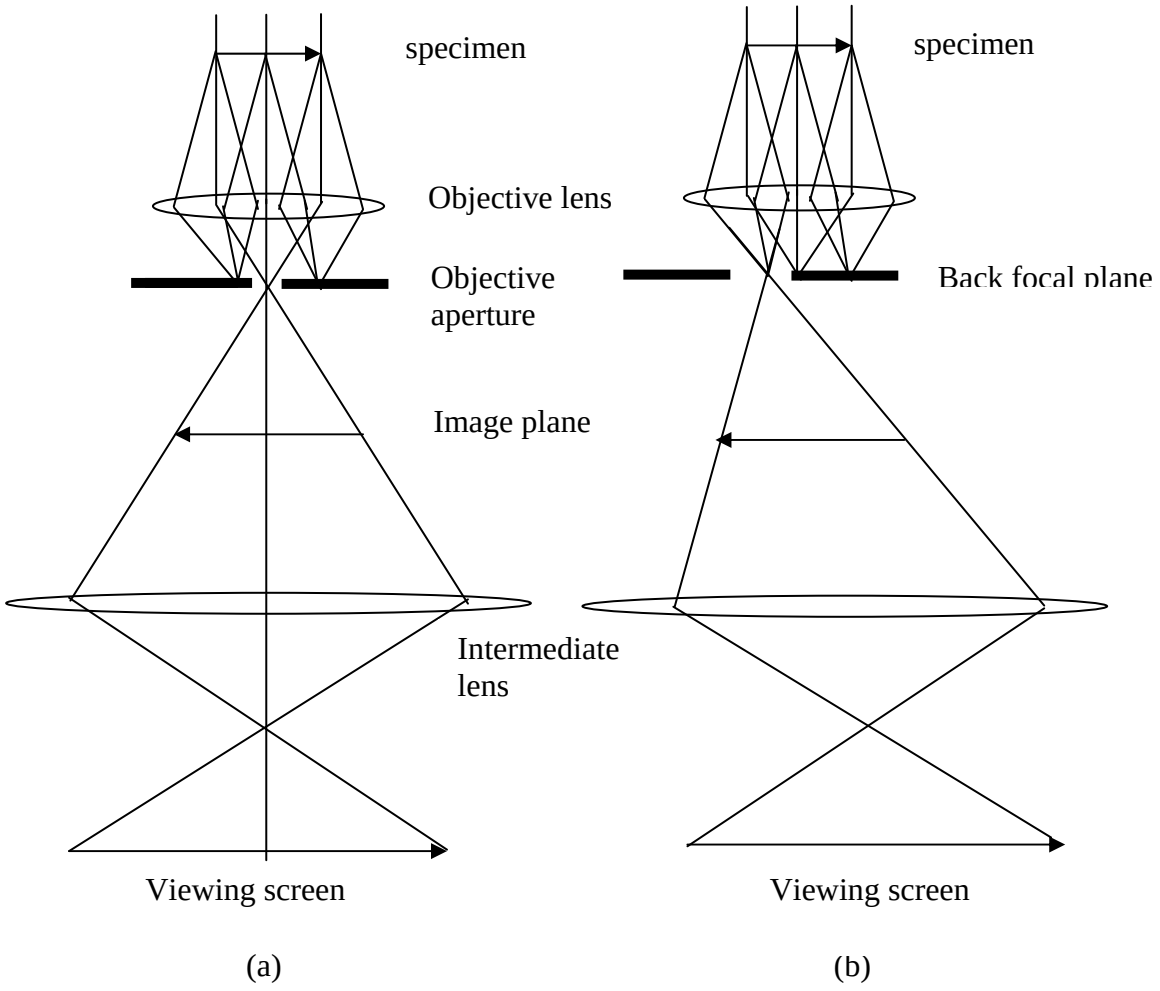

Figure 3.7: Schematic represent the bright field (BF) mode (a) and dark-field (DF) mode (b) [36].

In case of electron diffraction pattern, the fluorescence screen is positioned normal to the incident beam. The rings of reflection from reflecting plane in polycrystalline recorded as shown in Fig. 3.8

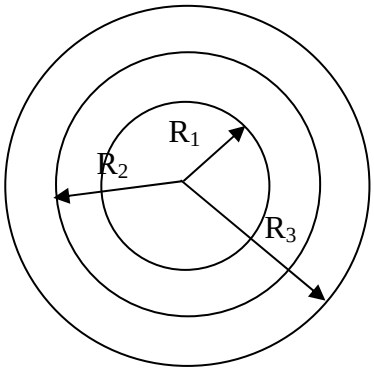

Figure 3.8: Selected-area electron diffraction pattern in polycrystalline [42].

When an electron beam passes the polycrystalline material, a random distribution of orientation, diffraction pattern will be produced from the superposition of single spot pattern. From Bragg's law condition, the total deflection angle is 2θ. The radius of a specific ring (R) relate the distance from material to screen (L) as shown

$$R = L\tan 2\theta \approx L2\theta \tag{3.6}$$

From Bragg's law equation

$$d = \frac{2\lambda L}{2R} \tag{3.7}$$

where d is the spacing between atomic planes in the crystal

λ is the wavelength of electron beam

For cubic structure

$$\text{Let } h^2 + k^2 + l^2 = N^2 \tag{3.8}$$

We can write the relation between the distance from the center spot to the reflection of interests and d-spacing

$$\frac{d_2^2}{d_1^2} = \frac{N_1^2}{N_2^2} = \frac{R_1^2}{R_2^2} \tag{3.9}$$

The forbidden and allowed reflection in cubic structure is shown in Table 3.1.

Table 3.1: Allowed and forbidden reflection in cubic crystal [42].

$h^2+k^2+l^2$	Primitive cubic	Face centered cubic	Body centered cubic
1	100	-	-
2	110	-	110
3	111	111	-
4	200	200	200
5	210	-	-
6	211	-	211
7	-	-	-
8	220	220	220
9	221/300	-	-
10	310	-	310
11	311	311	-
12	222	222	222
13	320	-	-
14	321	-	321
15	-	-	-
16	400	400	400

3.5 Nanoindentation

Nanoindentation is a method for investigation the mechanical properties such as elastic modulus and hardness from the reading of indenter load and depth of penetration. We use Berkovich indenter tip in this work.

Figure 3.9: The Berkovich indenter tip [43].

The hardness is defined as

$$H = \frac{P}{A_p} \tag{3.10}$$

$$A_p = 24.5h_p^2 \tag{3.11}$$

where A_p is the projected area of the contact

P is the maximum load or force

h_p is plastic depth

The purpose of nanoindentation testing is to determine the hardness and modulus from the indenter load and depth of penetration. The relation between load and depth is shown in Fig. 3.10. An indirect measurement of the contact can be estimated from the depth of penetration. When the indenter is removed from material, the plastic deformation can be occurred. The definition of hardness is the resistance to the penetration by the harder material or the resistance of deformation [44].

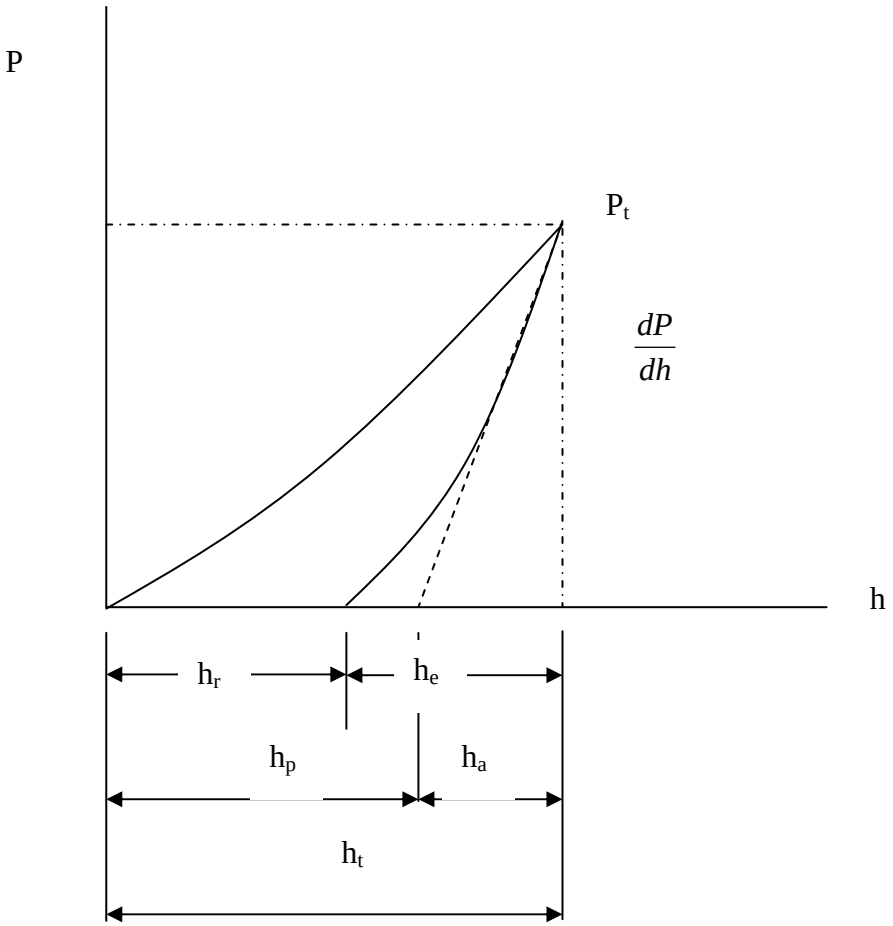

Figure 3.10: Load versus displacement for load and unload [45].

where P_t is the maximum load

h_t is the total depth at the maximum load

h_r is the residual depth after unloading

h_e is the elastic displacement during unload

h_a is the depth from the edge of the contact to the surface at the maximum load

The reduced modulus can be determined from the slope of the unloading curve at the maximum load.

$$E_r = \frac{1}{2}\sqrt{\frac{\pi}{A}}\frac{\partial P}{\partial h} \tag{3.12}$$

The reduced modulus (E_r) combines the modulus of indenter (E_i) and the modulus of specimen (E_s)

$$\frac{1}{E_r} = \frac{(1-\nu_i^2)}{E_i} + \frac{(1-\nu_s^2)}{E_s} \tag{3.13}$$

where ν_i is the Poisson's ratio of diamond indenter (0.07)

ν_s is the Poisson's ratio of specimen between 0 to 0.5

E_i is the modulus of diamond indenter (1140 GPa)

The Poisson's ratio resists a change in a volume and shape. For example, the Poisson's ratio of rubber is around 0.45 to 0.5 [46], whereas the Poisson's ratio of steel is 0.29 [47]. The slope of the unload curve shows the stiffness, the resistance of an elastic body to deformation after applied force.

3.6 Nanoscratch

The indenter scratches on the surface of the sample. The friction coefficient with a ramped or constant normal force can be determined by dividing the lateral force by the normal force. Either a change in friction coefficient or critical load (the minimum normal force which failure occur) can be investigated as the scratch resistance. It depends on the shape of indenter, the duration and rate of load. However, the adhesion is not a well-develop process because it depends on the type of film/substrate system [45].

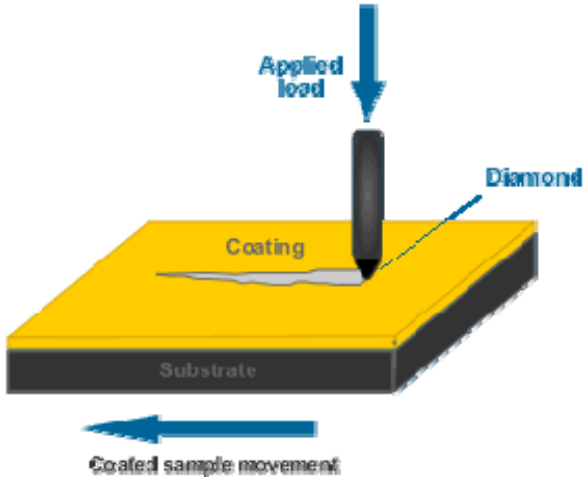

Fig 3.11: Scratch test diagram [48].

3.7 X-Ray Photoelectron Spectroscopy

X-ray photoelectron spectroscopy (XPS) for measurement the energy of electron emitted from a material. The notation of photoelectron can be described in quantum numbers: n, l, s, j. The first notation, n, the principal quantum number describes the electron shell. This takes value of 1, 2, 3 etc. The second, l, the orbital angular momentum describes the sub-shell. The value of l start from 0 to n-1 (0= s orbital, 1=p orbital, 2=d orbital, 3=f orbital). The third, s, spin quantum number describes the spin of electron. There are two directions counter-clockwise (s = -½) and clockwise (s = ½).The forth, j, total angular momentum quantum number calculates from l+s. In spectroscopists' notation, the subscript number refers to the j value, as shown in Table 3.2. When the specimen is bombarded with an x-ray photon, electrons from a core level are ejected. The energy of the emitted photoelectron is analyzed by the electron spectrometer. The binding energy of electron (E_B) can be calculated from

$$E_B = h\nu - E_k - W \tag{3.14}$$

where $h\nu$ is the photon energy

E_k is kinetic energy of electron

W is spectrometer work function

Table 3.2: The relationship between quantum numbers, spectroscopists' notation and x-ray notation [49].

Quantum numbers				Spectroscopists' notation	X-ray notation
n	L	S	J		
1	0	+1/2,-1/2	1/2	$1s_{1/2}$	K
2	0	+1/2,-1/2	1/2	$2s_{1/2}$	L_1
2	1	+1/2	1/2	$2p_{1/2}$	L_2
2	1	-1/2	3/2	$2p_{3/2}$	L_3
3	0	+1/2,-1/2	1/2	$3s_{1/2}$	M_1
3	1	+1/2	1/2	$3p_{1/2}$	M_2
3	1	-1/2	3/2	$3p_{3/2}$	M_3
3	2	+1/2	3/2	$3d_{3/2}$	M_4
3	2	-1/2	5/2	$3d_{5/2}$	M_5

The process of photoemission is shown in Fig. 3.12. The electron from K shell is ejected from atom if the binding energy is less than the x-ray photon energy.

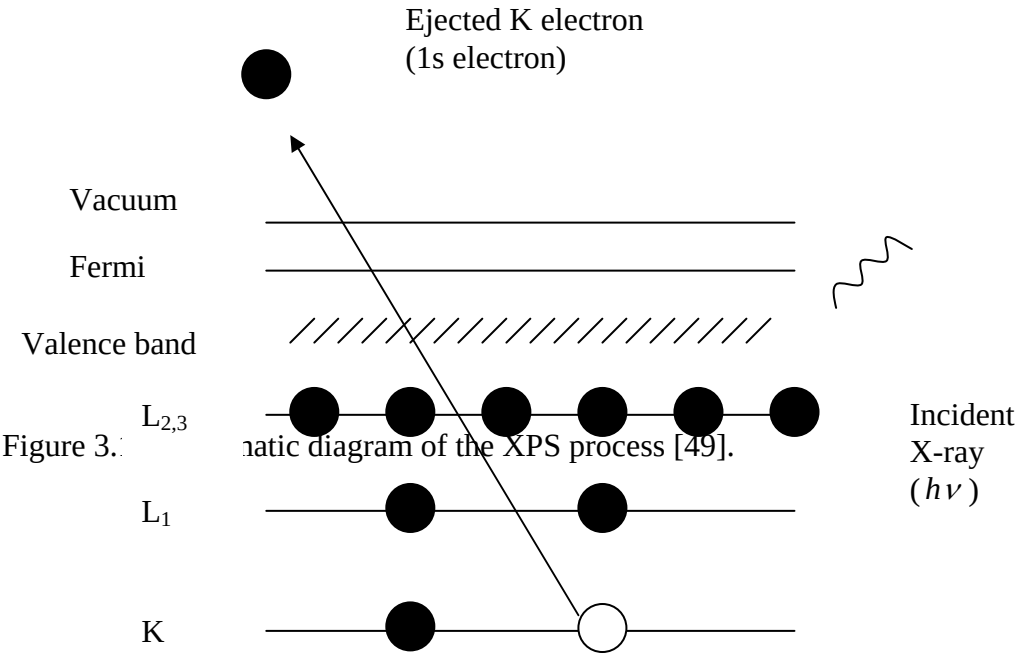

Figure 3.1 matic diagram of the XPS process [49].

3.8 van der Pauw Method

The van der Pauw method is a technique used for investigation the sheet resistance, a measurement of resistance of uniform thickness films. The thickness of samples has to less than the width and length to reduce the error in calculation. Four ohmic cantacts, infinitely small region for current- voltage measurement, are constructed on the boundary of samples or as close as possible, as show in Fig. 3.13. [50].

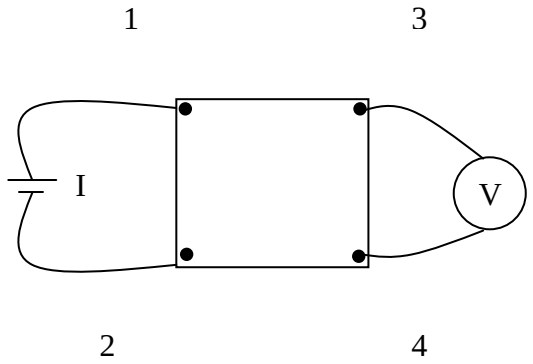

Figure 3.13: Schematic representation the four ohmic contacts for I-V measurement.

$$R = \frac{\rho}{d} = \frac{\pi}{\ln 2} R_{ave} F\left(\frac{R_2}{R_1}\right) \qquad (3.15)$$

where R is the sheet resistance (Ω/square)

ρ is the resistivity (Ωm)

d is the thickness of films (m)

There are special conditions for measurement the specific resistivity. The contacts need to be sufficient small at the circumference of the samples. In addition, the thickness of sample has to be a homogeneous and there is no isolate hole on the surface. Contact 1, 2, 3, 4 fixed on the boundary of sample. The resistance $R_{12,34}$ is defined as the potential difference V_4-V_3 between the contact 4 and 3 per unit current through the contact 1 and 2. The direction of current start from the contact 1 to the contact 2. Similarity, the resistance $R_{23,41}$ are defined.

The specific resistance can be written in the form

$$\rho = \frac{\pi d}{\ln 2}\left(\frac{R_{12,34} + R_{23,41})}{2} f\left(\frac{R_{12,34}}{R_{23,41}}\right)\right. \tag{3.16}$$

where f is a function of the ratio $\frac{R_{12,34}}{R_{23,41}}$ and satisfies the relation, as shown in Fig. 3.14.

$$\frac{R_{12,34} - R_{23,41}}{R_{12,34} + R_{23,41}} = f \arccos h\left\{\frac{\exp(\ln 2 / f)}{2}\right\} \tag{3.17}$$

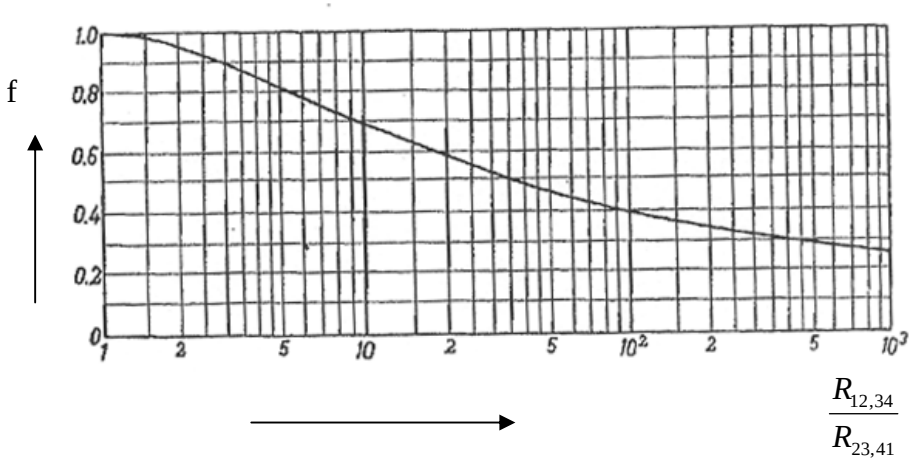

Figure 3.14: The function f used for determine the resistivity of sample, plotted as a function of $\frac{R_{12,34}}{R_{23,41}}$ [50].

3.9 Capacitance-Voltage Measurement

Capacitance-voltage (C-V) measurement is used on MOS to determine semiconductor parameters such as oxide charge, oxide thickness. Fig. 3.15 shows the MOS structure. A simple MOS structure consists of metal plate on the top layer, silicon oxide insulator in the middle layer and semiconductor substrate.

The high frequency DC voltage is applied to capacitor while the capacitance is measured. The frequency of AC signal from 10 kHz to 10 MHz is commonly used for measurement. The C-V measurement can be divided into 3 regions: accumulation,

depletion and inversion, as shown in Fig. 3.16. When negative DC bias was applied to capacitor, the majority carriers (hole) in the substrate are attracted to accumulate near the oxide layer. This phenomenon can be explained that the carriers cannot pass through the insulate layer. For p-type CMOS, the negative bias voltage is enough to keep constant capacitance and flat slope in accumulation region. As the voltage increases toward positive, the positive gate repels the majority carrier (holes) far away from the interface between oxide layer and semiconductor substrate. The depletion region can be formed beneath the oxide layer. It creates another insulator layer because of the absent of free-moving charge. As a result, there are 2 capacitances in the series: oxide layer and depletion layer. When the voltage becomes more positive, the depletion zone penetrates deeply in the semiconductor. Therefore, the capacitance tends to decrease in depletion region. The slope in this region tends to negative. As the voltage become more positive, the minority carriers (electrons) are attracted. These electrons are accumulated at the interface between oxide layer and semiconductor. This region is called “inversion region” because of inversion of carriers [51-52].

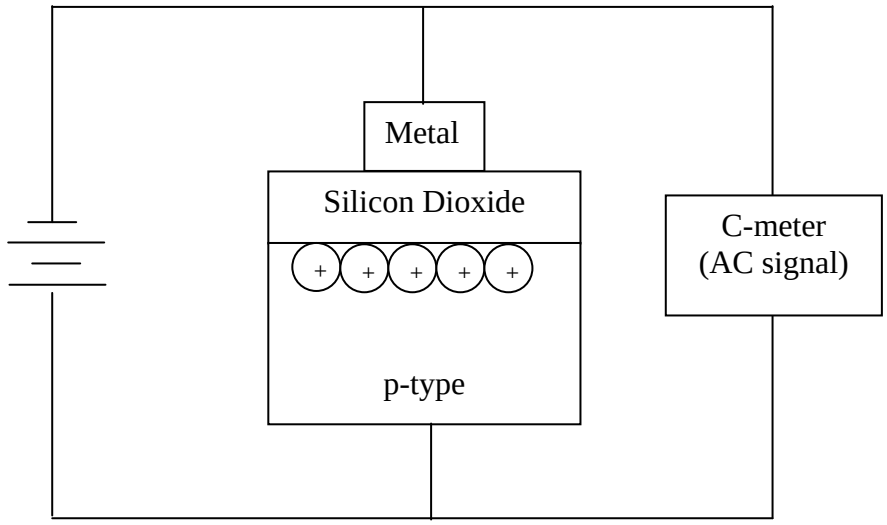

Figure 3.15: C-V measurement for the MOS structure formed on a P-type substrate [51].

The flat band voltage (V_{fb}) can be extracted from C-V measurement. An external voltage of V_{fb} is applied to MOS structure to make the disappear of band bending. This condition is called flat band condition. The semiconductor band becomes flat after flat band voltage is applied [51-52].

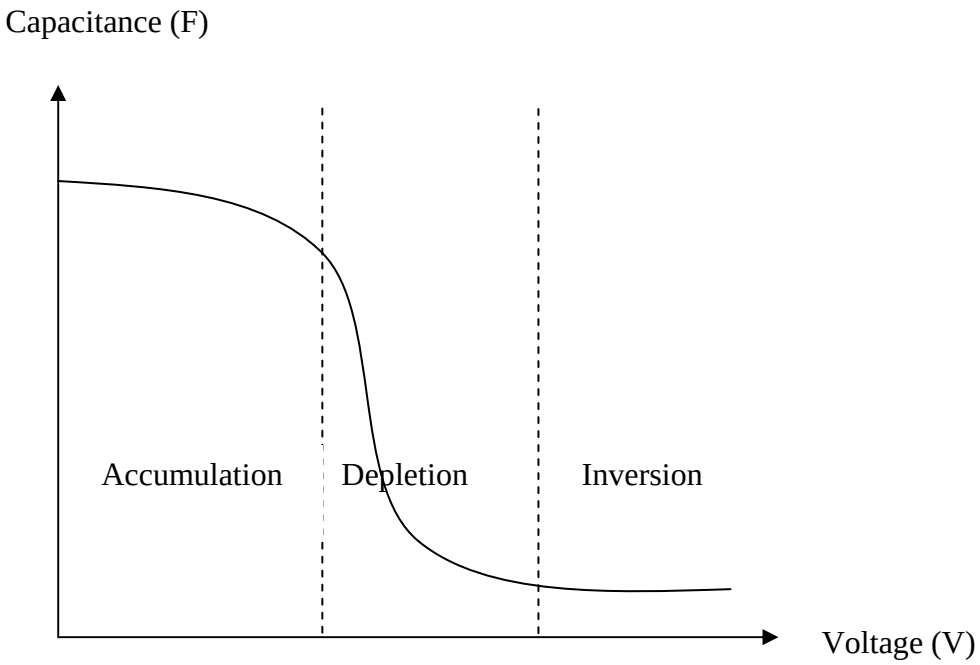

Figure 3.16: The high frequency C-V curve in 3 region: accumulation, depletion and inversion [51].

CHAPTER IV

EXPERIMENTAL DETAILS AND RESULTS DISCUSSION

Part I: Transition Metal Nitride

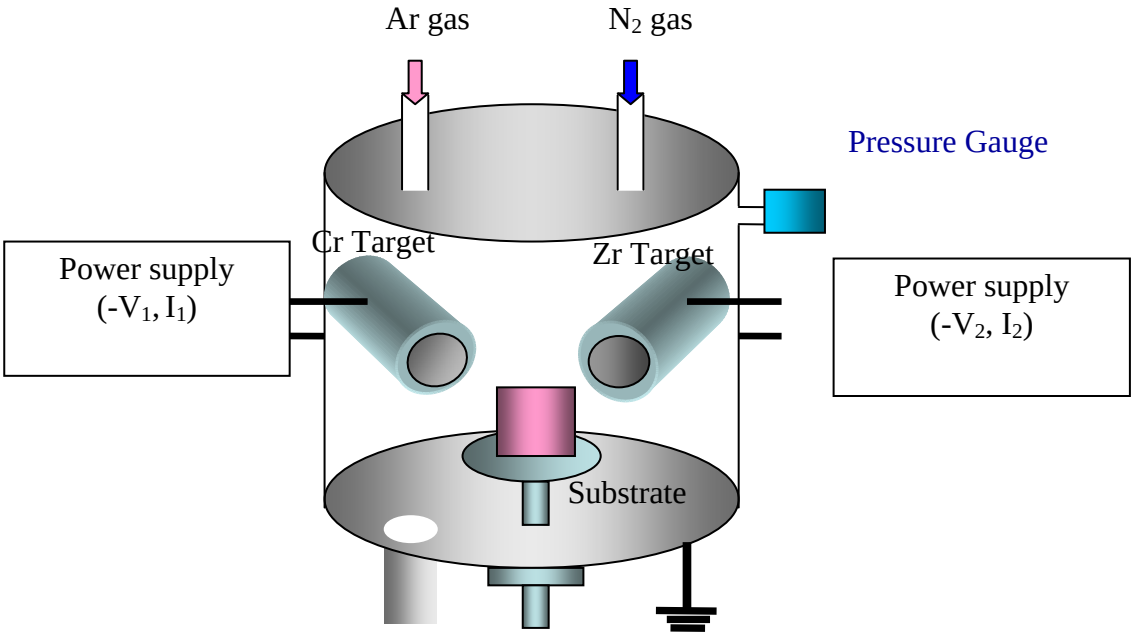

Figure 4.1: Schematic of dual magnetron sputtering system for growth of Cr-Zr-N films

4.1 Thin Films Synthesis

To synthesis the ternary alloy nitride compound, two pure metallic targets (99.95%) of Cr and Zr, were used in this work. The base pressure of the sputtering system was at $5x10^{-5}$ mbar. Both Ar and N_2 gases were introduced to a chamber, as the sputtered gas, for plasma, to grow Cr-Zr-N. The nitrogen partial pressure $N_2/Ar+N_2$ was varied from 0 to 100% to study the optimized condition. The plasma glow discharge can be occurred in the chamber after the voltage is applied through the magnetron. If there is enough energy to ionization, Ar^+ and N_2^+ ions will be produced. As N_2^+ ions move to bombard the targets, the surface atoms react with ions. Consequently, CrN and ZrN are formed on each surface target. At the same time, the targets are bombarded by Ar^+. It makes the sputtering process occur. Then, ternary

nitride films deposited on the substrate. During the formation of films, the discharge current of each target was constantly controlled at 0.5 A. All films were grown without an extra heat source, except the transferred energy from the collision of adatoms and plasma species at the substrate surface. In the first part, we studied the effects of nitrogen partial pressure, post-annealing temperature, magnetron current and bias voltage on the structural properties, as well as, the resistivity and mechanical properties of Cr-Zr-N films.

4.2 Effect of Nitrogen Partial Pressure

The results show that Cr-Zr-N film grown at 20% nitrogen partial pressure has the best mechanical properties in hardness and modulus. The details on experimental setup are shown in paper 1 (see appendix B). For optimization, Cr-Zr-N film grown at 20% nitrogen partial consists of the maximum amount of nitrogen, bonding with metallic atoms. The higher nitrogen partial pressure can cause more interstitial nitrogen atoms in films. It causes an increase in the sheet resistance as the nitrogen partial increases. In contrast, Cr-Zr-N films grown at lower nitrogen partial pressure than 15% show amorphous structure, no long range order. The nitrogen composition in Cr-Zr-N films tends to increase in the range between 0 to 20 % nitrogen partial pressure, as can be seen from Fig. 4.2. At over 20 % nitrogen partial pressure, the nitrogen composition is almost constant due to the saturated incorporation of nitrogen atoms in the films.

Generally in the reactive sputtering process, the nitrogen ions react with surface target. More nitrogen partial pressure makes more the coverage of nitride compound on surface target. As both nitrogen ions and argon ions move to bombard the coverage area of nitride compound on surface target, the deposition rate tends to decrease with an increase in the nitrogen partial pressure. The maximum roughness is 7.9 nm at 20% nitrogen partial pressure because there is competition among orientation of (111), (200) and (220) domains, as seen in the Fig. 4.3 (see also in paper no.1) [53].

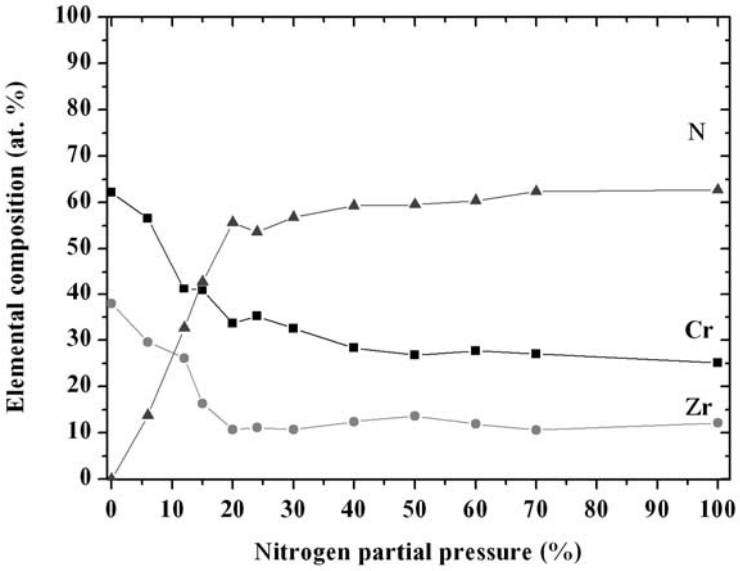

Figure 4.2: Elemental concentrations of Cr-Zr-N films formed with different nitrogen partial pressures [53].

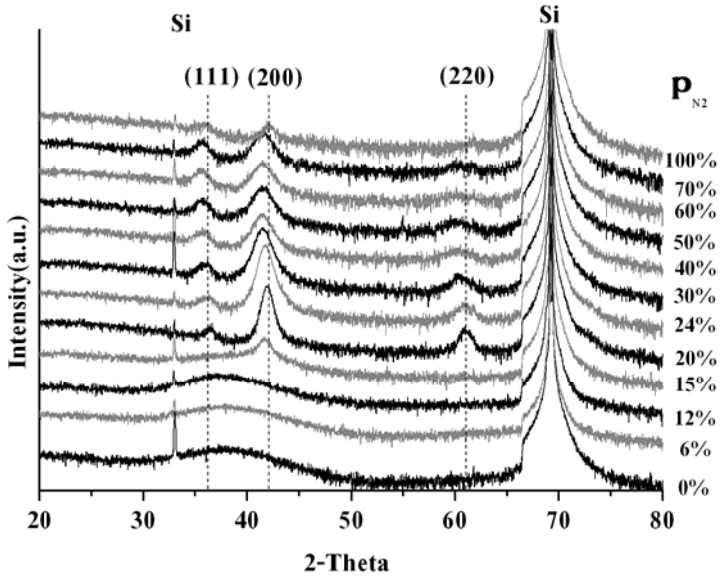

Figure 4.3: Representative XRD spectra of Cr-Zr-N films grown at different nitrogen partial pressures [53].

4.3 Effect of Annealing Temperature

The stoichiometric Cr-Zr-N films grown at 20% nitrogen partial pressure were annealed under an Ar flow at vacuum pressure at 300 °C, 500 °C and 700 °C, respectively. The details on experimental setup are shown in paper 1 (see appendix B).The results shows that the hardness of Cr-Zr-N films tends to increase after annealing. The maximum hardness was found at 35.1±4.7 GPa after annealing at 700 °C. There is no phase separation after annealing. This shows that Cr-Zr-N thin film material grown at 20 % nitrogen partial pressure has thermal stability until 700 °C. After annealing, nitrogen atoms tend to out diffuse from interstitial site. This phenomenon causes the diffraction peaks shift toward the higher diffraction angles, indicating lower lattice constant [53].

4.4 Effect of Magnetron Current

Magnetron current of Cr and Zr targets was varied to control the composition of films. The magnetron current related to the composition in films. The nitrogen partial pressure was kept constant at 20%. As the magnetron current of current increases, a number of ions impinging to the target also increase. This phenomenon makes an increase in the sputtered atoms from the surface target.

For the variation of magnetron current of Zr target, the magnetron current of the Zr target was varied from 0 - 1.5 A, whereas the magnetron current of Cr target was kept constant at 0.5 A (165 W).

The elemental concentrations of Cr, Zr and N in the as-deposited films on silicon (100) substrates, deposited from different currents of the Zr target, are summarized in Table 4.1. The concentration of N in the films is almost constant, whereas the concentration of Zr increases almost linearly with increases in the magnetron current of Zr. This is due to an increase in the sputtering rate S_t which corresponds to the target-current I_t and target-voltage V_t linearly. Therefore, the deposition rate tends to increase with an increase in power of target, as shown in Fig. 4.4. The energy of ions bombarding the target depends on V_t with an increase in I_t, the

number of ions impinging on target so the sputtering rate increases. The power of Cr was constant (165 W), whereas the power of the Zr target is proportional to the magnetron current of the Zr target.

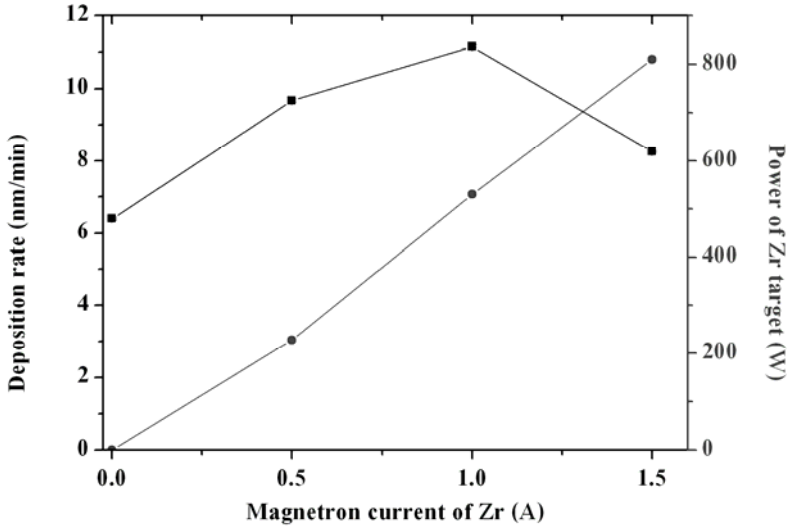

Figure 4.4: Deposition rate of Cr-Zr-N films (■) and the power of Zr target (●) as a function of the magnetron current of Zr.

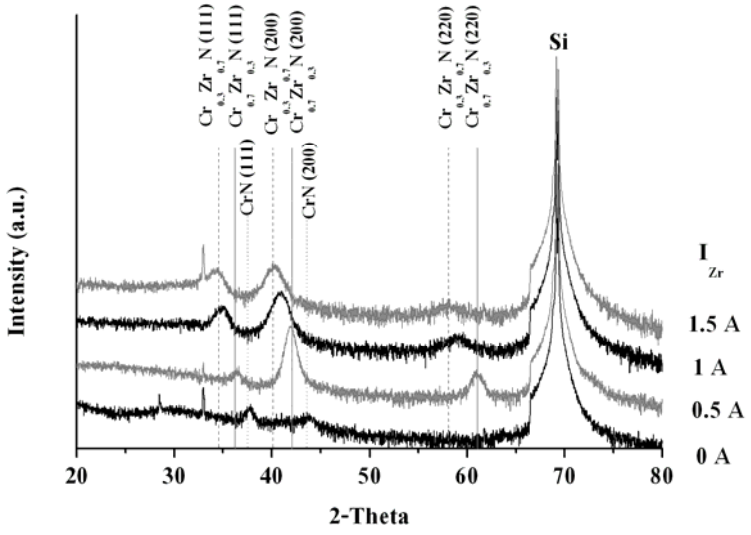

Figure 4.5: Representative XRD spectra of Cr-Zr-N films that were made with different magnetron currents of Zr target.

The representative x-ray diffraction (XRD) spectra of Cr-Zr-N films grown with different current of Zr, plotted on a semi-log scale are shown in Fig. 4.5. All the diffraction peaks shift towards the lower diffraction angles, indicating that the lattice constant increases, as the Zr current increases. This phenomenon can be explained that the zirconium atoms, substituted for the chromium atoms, have a larger radius than the chromium atoms (0.159 vs. 0.125 nm, respectively). As the magnetron current of Zr increases, the stoichiometric form of Cr-Zr-N changes from $Zr_{0.3}Cr_{0.7}N$ to $Cr_{0.3}Zr_{0.7}N$ due to an increase in the concentration of zirconium in the films. Moreover, the (111) plane tends to develop with increasing Zr currents, because the magnetron Zr current affects the developmental texture. As the magnetron current of Zr increases, the texture coefficient of the (111) plane tends to increase, due to a decrease in the energy of ad-atoms to form films. The higher sputtering rate of the Zr target increases the amount of zirconium nitride and nitrogen atoms sputtered to form films material, leading to more collisions before deposition into the Si substrate. Therefore, the ad-atoms have less energy to form films with an increase in current of Zr.

Table 4.1: The properties of Cr-Zr-N films as a function of the magnetron current of Zr.

Current of Zr (A)	Elemental composition (Atomic %)			Roughness (nm)	Hardness (GPa)	Reduced modulus (GPa)	Sheet resistance (Ohm/square)
	Cr	Zr	N				
0	36	0	64	4.6	10.9 ± 0.3	140.3 ± 15.8	764.4 ± 17.8
0.5	34	11	55	7.9	30.0 ± 4.6	324.1 ± 21.7	38.3 ± 0.1
1	17	24	59	2.7	22.7 ± 1.7	233.8 ± 13.9	875.4 ± 5.4
1.5	11	29	60	2.1	27. 4 ± 2.7	249.4 ± 10.7	683.7 ± 7.5

The surface morphology of Cr-Zr-N films, as evaluated by atomic force microscope (AFM), is shown in Fig. 4.6, and RMS roughness for all films is shown in Table 4.1.

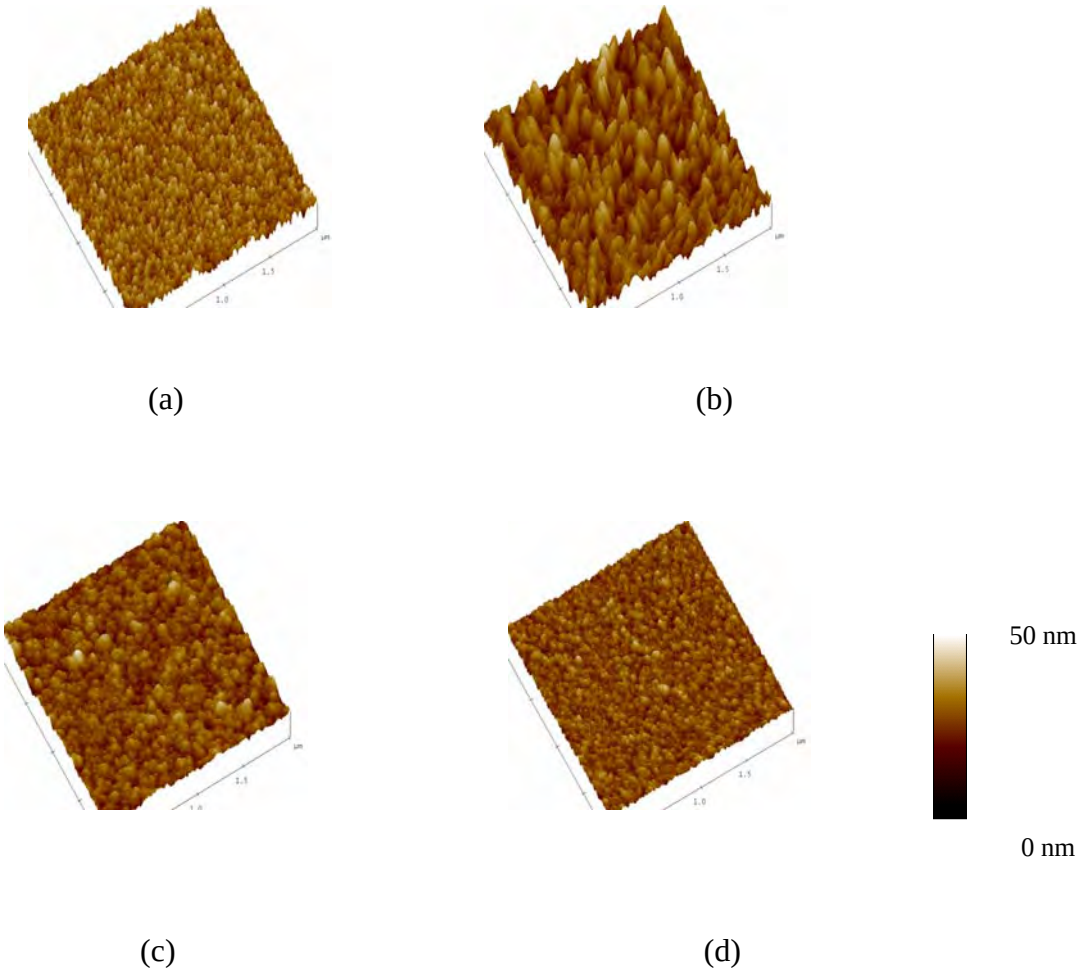

Figure 4.6: Representative AFM images of Cr-Zr-N films formed with different magnetron Zr currents of (a) 0 A, (b) 0.5 A, (c) 1 A and (d) 1.5 A.

The RMS roughness of Cr-Zr-N films was initially higher than that of CrN films when formed at a Zr current of 0.5 A (Table 4.1), because of the substitution of Cr atoms with Zr atoms. However, the roughness of Cr-Zr-N tends to decrease with increasing magnetron currents of Zr which is in agreement with a previous report [7]. As the current of Zr increases, the film process is increased in the supersaturation. This condition shows the high initial nucleation density and small size of critical

nucleus. This phenomenon makes the smooth film and a decrease in the grain size [1].

The maximum roughness of Cr-Zr-N films is related to the maximum hardness (see Table 4.1), where the hardness of Cr-Zr-N films is higher than that of CrN in the same growth conditions. This can be due to the addition of zirconium in these films forming a solid solution. However, an increase in the composition of zirconium in the films does not significantly affect the hardness of films which instead depends on an appropriate nearly stoichiometric composition of the film. If nitrogen in the film is higher than the maximum stoichiometric level for metal nitride formation, the excess nitrogen will situate in the interstitial sites. Moreover, excess zirconium atoms in films, situating in interstitial site, lead to a decrease of the mean free path of conductive electrons [54]. This would be expected to result in an increase in the sheet resistance, as was indeed seen in this study where the sheet resistance increased as the magnetron Zr current was increased (Table 4.1).

Table 4.2: Elemental concentrations, hardness and reduced modulus of Cr-Zr-N films with varying magnetron current of Cr targets.

Current of Cr (A)	Elemental composition (Atomic %)				Stoichiometric form	Hardness (GPa)	Reduced modulus (GPa)
	Cr	Zr	N	O			
0.3	16	11	56	17	$Cr_{0.16}Zr_{0.11}N_{0.56}+O_{0.17}$	35.9 ± 2.2	277.6 ± 10.7
0.4	23	10	67	-	$Cr_{0.23}Zr_{0.10}N_{0.67}$	27.0 ± 3.4	245.4 ± 22.5
0.5	32	7	61	-	$Cr_{0.32}Zr_{0.07}N_{0.61}$	27.3 ± 1.8	270.4 ± 17.1
0.6	35	6	59	-	$Cr_{0.35}Zr_{0.06}N_{0.59}$	24.4 ± 1.0	252.8 ± 14.0
0.7	37	5	58	-	$Cr_{0.37}Zr_{0.05}N_{0.58}$	25.8 ± 2.4	264.1 ± 9.8

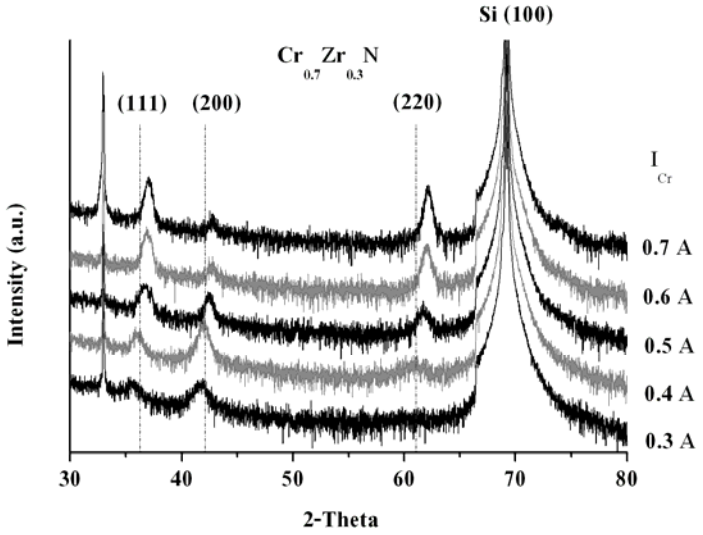

Figure 4.7: Representative XRD spectra of Cr-Zr-N films that were made with different magnetron currents of Cr target.

For the variation of magnetron current of Cr target, the magnetron current of Cr was varied from 0.3 A to 0.7A, whereas the magnetron current of Zr was kept constant at 0.8 A (350 W). In this study, the nitrogen partial pressure is kept constant at 20% nitrogen partial pressure. The elemental composition of Cr tend to increase when the magnetron current of Cr increase, as shown in Table 4.2. For XRD data as shown in Fig. 4.7, all diffraction peaks shift towards the higher diffraction angles, indicating a decrease in the lattice constant. This phenomenon can be explained as Cr atoms which have a smaller radius, substituted for Zr atoms in the lattice. (111) and (220) orientations can be developed after the composition of Cr in films increases. However, the number of (200) orientation tends to decrease. The adatoms have low energy to move on the surface of substrate due to no external energy source. As the magnetron current of Cr increases, the deposition rate of films tends to increase. The atomic shadowing effect can be occurred in this case because the adatoms have low energy to diffuse on the surface. In coalescence process, (200) orientation can expand on the surface slowly because of low diffusivity (more stable) [21]. Therefore, new adatoms have more probability to be trapped on higher diffusivity planes, (111) and (220). This phenomenon makes more (111) and (220) orientations as Cr atoms in films increase. For mechanical properties as shown in Table 4.2, the hardness and

modulus tend to decrease as the Cr composition in films increase. The maximum hardness and reduced modulus are 35.9±2.2 GPa and 277.6±10.7 GPa, respectively. It relates to a change in preferred orientation peak. As the texture coefficient of (200), $\frac{I_{200}}{\sum I_{200} + I_{111} + I_{220}}$ decrease, the hardness tends to decrease. Among (111), (220 and (200), (200) plane is the maximum density [55]. As the number of (200) orientation decrease, the density of films tends to decrease. Although the hardness and the density are not directly related, vacancies or voids in films are associated with a change in the dislocation density or configuration during plastic deformation [56].

4.5 Effect of Bias Voltage

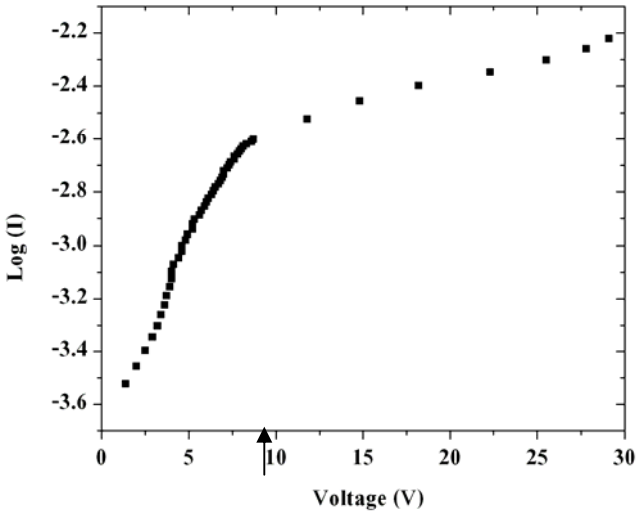

Figure 4.8: The relation between Log (I) and voltage Cr-Zr-N growth film at 20% nitrogen partial pressure.

Fig. 4.8 shows the relation between Log (I) and voltage in the Cr-Zr-N growth film at 20% nitrogen partial pressure. The knee shows the plasma potential (V_p). In this study ternary Cr-Zr-N films were grown on both Si(100) substrates and 316L stainless steel by dual unbalanced dc magnetron sputtering. Prior to growth Cr-Zr-N films, the 75 nm of Cr interlayer was grown in Ar to increase the adhesive between

the substrate and Cr-Zr-N film. The nitrogen partial pressure ($N_2/Ar+N_2$) during the process was kept constant at 20% which is the optimized condition from our previous study. During the growth, ion-assistance was used by applying the negative bias (V_s) to the substrate for attract Cr-Zr-N growth film at 20% nitrogen partial pressure. The ions from the plasma nearby move to bombardment the surface of substrate. The maximum kinetic energy of ions (E_i) can be calculated from the difference between plasma potential (V_p) and V_s, $E_i \approx e|V_s - V_p|$. From plasma characterization graph shown in Fig. 4.9, the plasma potential at substrate was 8 V and the floating potential was 0.5 V. The ion-to-metal atom flux ratio was equal to 3. The assisted ion energy during growth Cr-Zr-N was varied from 38 eV to 128 eV.

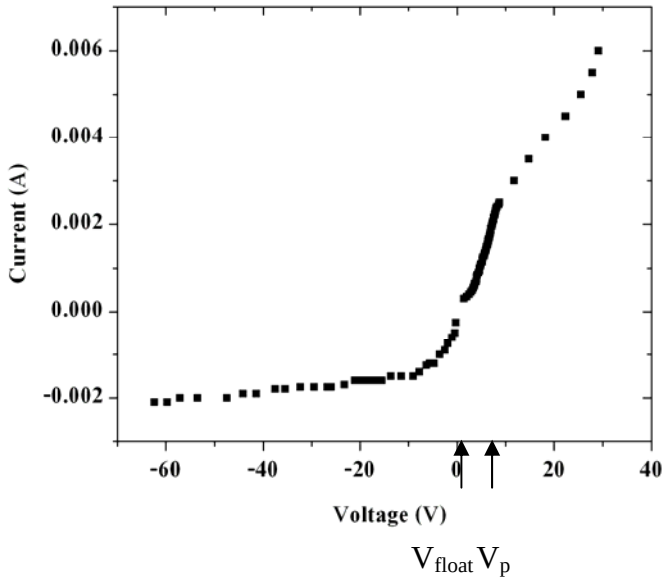

Figure 4.9: The plasma characteristic curve Cr-Zr-N growth film at 20% nitrogen partial pressure.

The energetically positive ions, especially N^+_2 ions can be occurred when there is energy greater than its molecule binding energy of nitrogen (9.7 eV) [57].

There are 2 main cases of the interaction between ions and surface film. One is that ions near the substrate move to bombard the surface atoms. The energy and momentum of ions were transferred to adatoms after collision. It makes the mobility of these adatoms increase, and these adatoms move on surface to find the equilibrium lattice site [58]. Another is that, the ions move to deeper into films especially in

vacant sites so, the density of films is increased due to a decrease in void [59-61]. These impinging ions are supersaturate N in the films. The deposition rate of Cr-Zr-N films grown reduces with increasing energy of ions.

The elemental concentrations of Cr, Zr and N in the as-deposited films at constant 20% nitrogen partial pressure with different ion energy on silicon (100) substrates are shown in Table 4.3.

Table 4.3: The elemental composition of Cr-Zr-N on Si, hardness and reduced modulus with difference ion energy.

Energy of ions (eV)	Elemental composition (Atomic %) Cr	Zr	N	O	Stoichiometric form	Hardness (GPa)	Reduced modulus (GPa)
8	27	8	50	15	$Cr_{0.27}Zr_{0.08}N_{0.50}+O_{0.15}$	22.9±0.6	200.8 ±6.0
38	34	8	50	8	$Cr_{0.34}Zr_{0.08}N_{0.50}+O_{0.08}$	18.5 ±3.5	263.4 ±30.2
68	28	9	63	-	$Cr_{0.28}Zr_{0.09}N_{0.63}$	29.8 ±12.3	206.5 ±61.9
98	28	9	63	-	$Cr_{0.28}Zr_{0.09}N_{0.63}$	29.9 ±11.7	239.6 ±48.2
128	24	8	68	-	$Cr_{0.24}Zr_{0.08}N_{0.68}$	39.3 ±13.4	295.8 ±67.5

The result indicates that the composition of nitrogen slightly depends on the ion energy. The nitrogen content in the film increases with increasing ion energy; in contrast, the composition of Cr in films is decreased with almost constant Zr concentration. The elemental composition of nitrogen in films can be occurred either the energetic neutral N atoms sputtered from both Cr and Zr targets and the nitrogen ions near the substrate. The excess of nitrogen in films at higher negative bias voltage can be occurred because the nitrogen ions near substrate incorporate in films at interstitial site or grain boundary. The more stable excess nitrogen in films are bonded with (200) orientation, a non-polar direction, than (111) plane, a polar direction in the NaCl structure [62-63]. Moreover, Cr atoms tend to decrease due to the re-sputtering effect because of the higher sputtering yield of Cr than that of Zr. In addition, the

bond dissociation energy of metal nitride is higher than that of metal [64]. The Cr atoms can be easier re-sputter than others.

The x-ray diffractrogram of films grown at different assisted ion energy is shown in Fig. 4.10. The result demonstrated that the energy of assisted-ions play role in preferred orientation and crystallinity, as other parameters kept constant. As the ion energy increases, the texture coefficient of (200), calculated from $I_{hkl} / \sum I_{hkl}$, start to increase . For energy of ions less than 1000 eV, the (200) orientation is the preferred orientation in all films because it has high density and shorter diffusion length [65]. The capture of N on (200) plane to form nitride compound has more strong bond than the bond between metal or nitrogen atoms. This phenomenon makes the diffusion or the mean free path of cation decrease [66]. The low flux ion irradiation in this work transfers the momentum and energy to adatoms. This result is similar to an increase in the growth temperature [63]. In this case, the growth temperature is higher than $0.5T_m$ (the melting point of film). Therefore, the bulk diffusion can be occurred. This phenomenon can be explained that the atoms incorporating in the films can readjust their position within the lattice to form the minimum of surface energy (200) orientation [18, 67]. (200) orientation can survive from ion bombardment because it is the opening channel. The ions can move into deeper part in this plane. This can lower the sputtering yield and create lattice distortion [66]. Moreover, the low flux of energetic ions affect the preferential sputtering (220) orientation in the films. At the higher energy of ion bombardment, the smaller grain size is the result of the reduction in the critical nuclei size due to an increase in nucleation rate from interaction between ions and surface [68]. The shadowing effect can be ignored because of the surface diffusion.

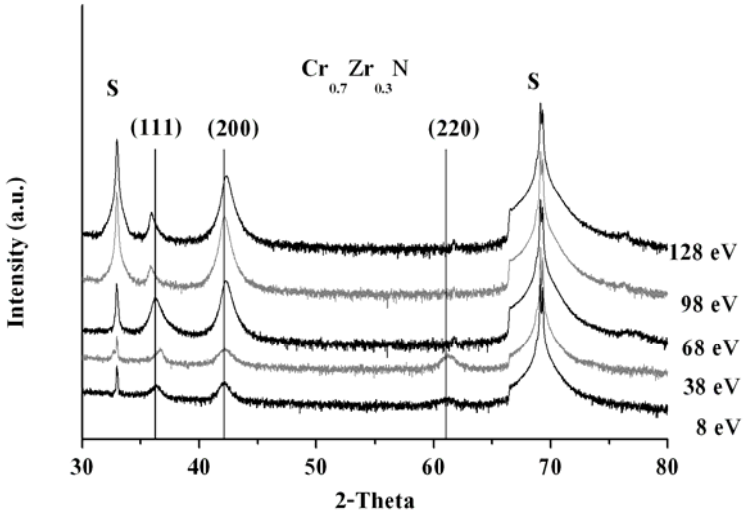

Figure 4.10: X-ray diffraction pattern of Cr-Zr-N on Si with various ion energy.

Cr interlayer was grown between the substrate and films to improve the adhesive and to reduce the mismatch of thermal expansion coefficient between the substrate and films [69]. From XRD graph, as shown in Fig. 4.11, it shows body center cubic (BCC) Cr (110) orientation and $Cr_{0.7}Zr_{0.3}N$ (111) texture can be developed by varying ion energy. Moreover, there is no signal related to the crystalline CrN and ZrN, presenting the solid solution of films. As the energy of ion bombardment increases, the energy transfers to adatoms also increase. In this reason, CrZrN tends to form more (111) orientation, consisting of either nitrogen atoms or metal atoms. The grain size of films on Cr layer is higher than that of Cr-Zr-N on Si. From AFM result, as shown in Fig. 4.12, it shows that the roughness of films tends to increase with increasing ion energy from 1.3 nm to 4.8 nm. The increase in the roughness is due to the resputtering effect from higher ion energy bombardment at the lowest substrate temperature. In the case of atomic packing, (110) is the most dense atomic packing in BCC structure; whereas, (111) is the most dense atomic packing in FCC structure [70]. This reason leads to the activation energy to form Cr-Zr-N(111) on Cr(110) is the minimum [71]. In this work, it presents that the preferable orientation of (111) doesn't relate to the larger thickness of film (large compressive

stress). The thickness of films decrease with increasing the energy of ions, however the texture coefficient of (111) also starts to increase. This means the strain energy doesn't affect the development of (111) orientation. The roughness of Cr-Zr-N on stainless steel is higher than that of Si because of the more roughness of stainless steel substrate before growth films.

Fig. 4.13 shows the cross-sectional microstructure of Cr-Zr-N grown at -98 eV in film without interlayer and film with interlayer of Cr-Zr-N on Si substrate. It shows the dense columnar and the voids cannot be observed due to low flux irradiation. The comparison between the diffraction pattern mode of Cr-Zr-N on Si and Cr-Zr-N/Cr on Si shows the agreement in XRD result that the grain size in film with interlayer is higher than that of film without interlayer. From XRD data, the lattice constant increases because the ions move to bombard films and stay in interstitial site. Moreover, it leads to less of the grain size and the roughness of films with an increase in ion energy due to an increase in the nucleation density during ion bombardment. During the nucleation growth, ion bombardment makes the dissociation of super-critical islands into sub-critical sized islands at high adatom supersaturation [72]. This makes the grain size decrease as an increase in ion energy.

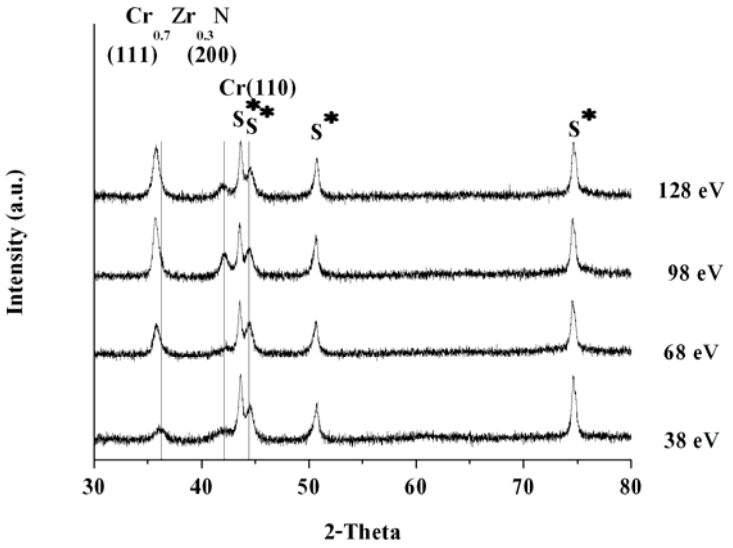

(a)

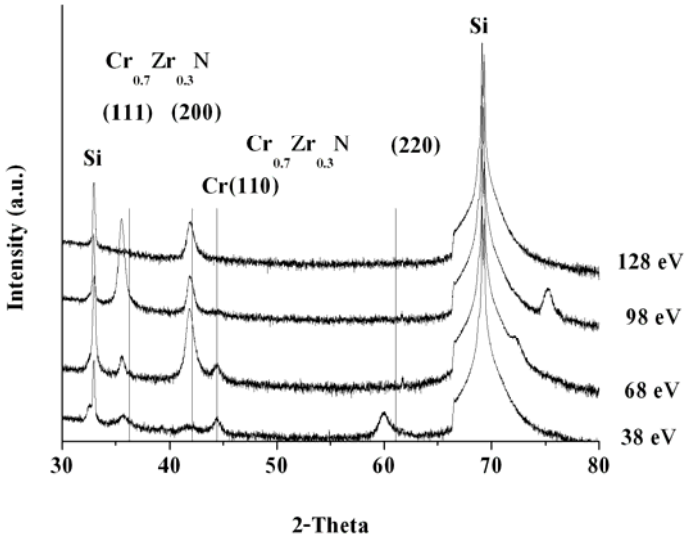

(b)

Figure 4.11: X-ray diffraction pattern of Cr-Zr-N/Cr with various ion energy (a) on stainless steel (S^*) and (b) on Si.

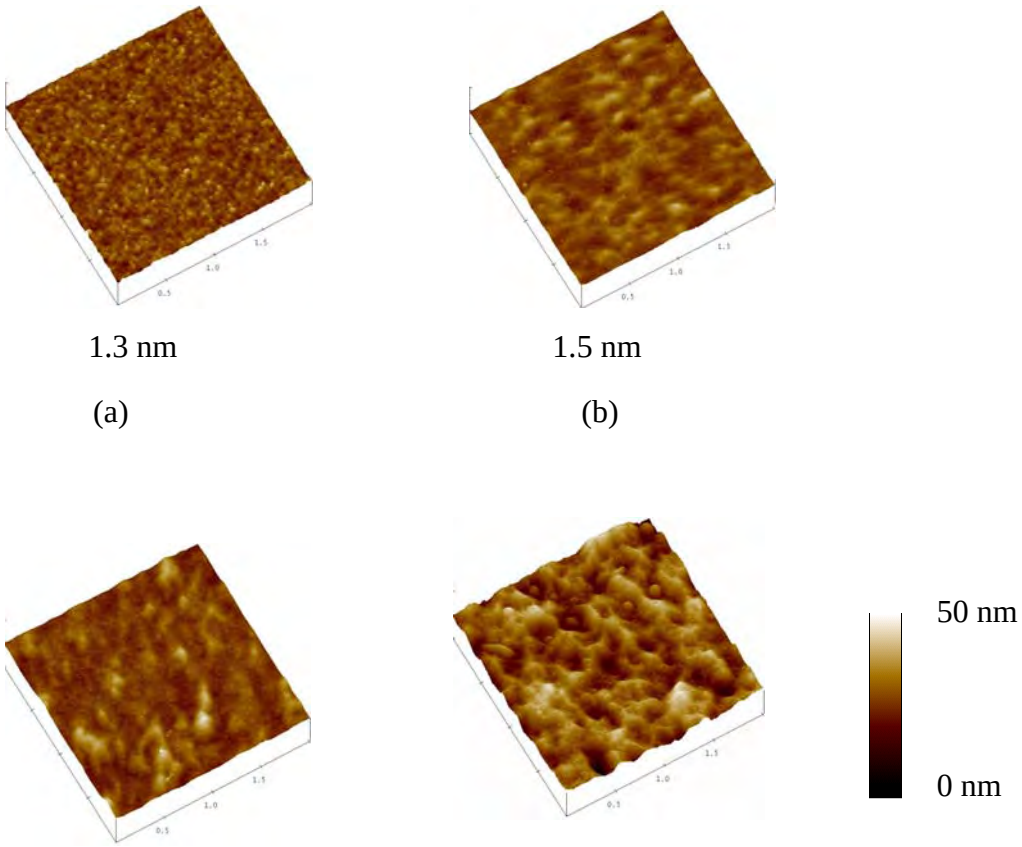

Figure 4.12: Representative AFM images of Cr-Zr-N films with interlayer on Si formed with different energy of ions (a) 38 eV, (b) 68 eV, (c) 98 eV and (d) 128 eV.

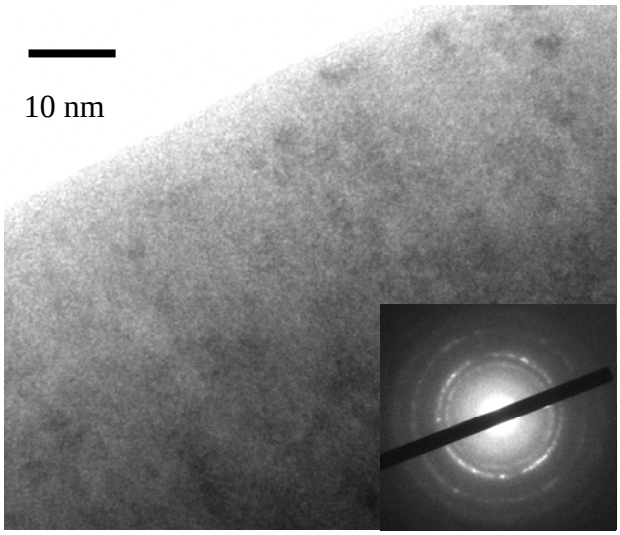

(a)

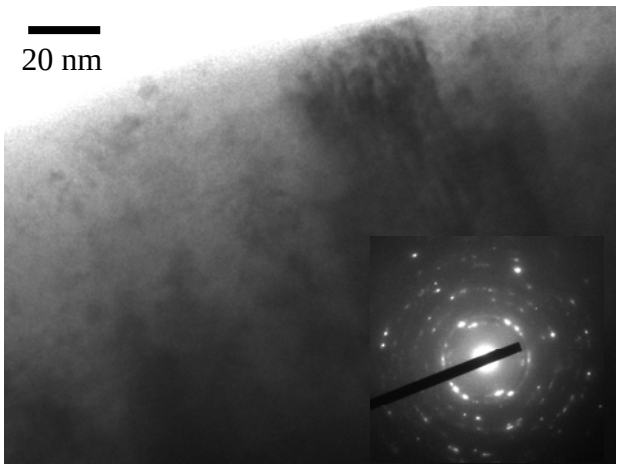

(b)

Figure 4.13: The cross-sectional microstructure of Cr-Zr-N grown at -98 eV a) film without interlayer b) film with interlayer.

The reduction of the grain size also affects the mechanical properties. It makes the hardness of films increase because of the increase in dislocation density.

Moreover, grain boundary restricts the motion of dislocation. The less grain size makes the higher hardness [72]. Table 4.3 shows the hardness and reduced modulus of Cr-Zr-N films without interlayer with different ion energy. For Si substrate, the hardness and reduced modulus of Cr-Zr-N film without interlayer increases with increasing ion energy. Although Cr interlayer affects the smoothness of the film, Cr interlayer makes the hardness and reduced modulus of Cr-Zr-N lower than that of films without interlayer. The hardness of film with interlayer is almost constant, approximately 25 GPa, whereas the reduced modulus of film with interlayer is about 240 GPa. Because the grain size of Cr interlayer is more 2 times than Si substrate, this phenomenon makes the grain size of film with interlayer increase with an increase in ion energy. The increase in grain size makes the hardness of films decrease [23]. For consideration the hardness of substrate, the hardness of steel is lower than that of Si [45]. The hardness and reduced modulus of Cr-Zr-N with interlayer on stainless steel is still higher than that of Cr-Zr-N films with interlayer on Si, as shown in Fig.4.14. The hardness of Cr-Zr-N films with interlayer on steel is in the range between 24 to 42 GPa, whereas the reduced modulus is in the range between and 217 to 349 GPa. Consideration for the maximum depth which the hardness of substrate doesn't affect the hardness of films. The report shows that the maximum depth of single crystal substrate is the lower than that of polycrystalline substrate [73]. In this work, the indentation depth of film with interlayer is kept constant at 50 nm. Therefore, the hardness of Cr-Zr-N/Cr on Si substrate may be affected from the Si substrate that softer than films. So, this reason can describe that the hardness of Cr-Zr-N films with interlayer on a single crystalline Si is lower than that of Cr-Zr-N films with interlayer on polycrystalline stainless steel.

This reason, Cr (110), the densest plane in bcc, can be formed the preferred orientation in Cr layer on all substrates at low ion energy. At low ion energy, 38 eV, there are competition among $Cr_{0.7}Zr_{0.3}N$ (111), (200) and (220) because of the limitation of surface diffusion energy. The grain size can be formed at saturate nucleation density at fist stage of formation films. There are many random orientations [66]. It is possible to grow (200) plane more than (111) at higher ion energy. Apart from the introduction of the Cr interlayer, the varying ion energy at low ion flux affects the evolution of structure, the inhibition the columnar structure and the higher roughness at higher ion energy bombardment.

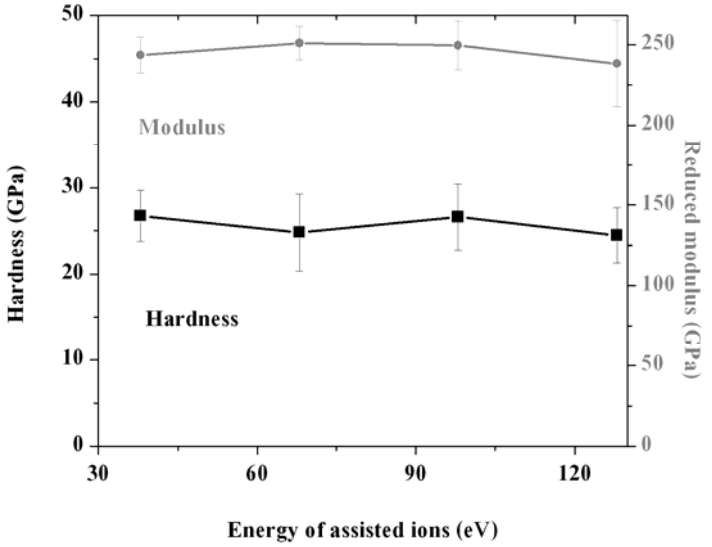

(a)

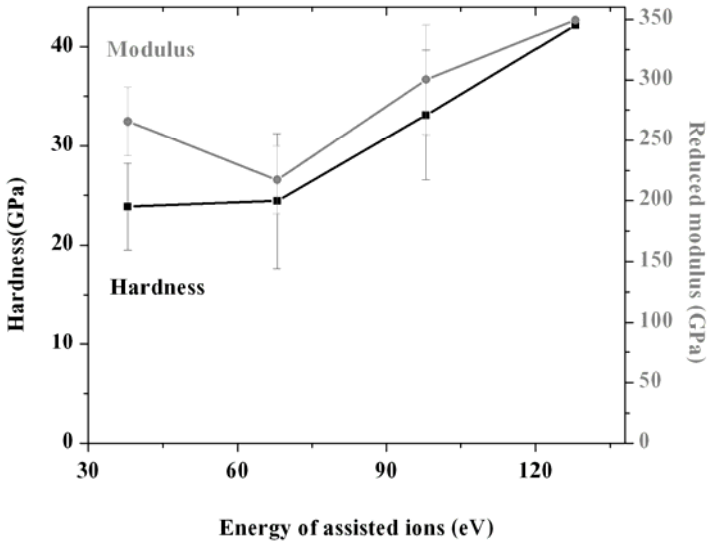

(b)

Figure 4.14: The relation between the hardness (■) and reduced modulus (●) with different ion energies of Cr-Zr-N with interlayer (a) on Si and (b) on stainless steel.

Part II: Transition metal carbide

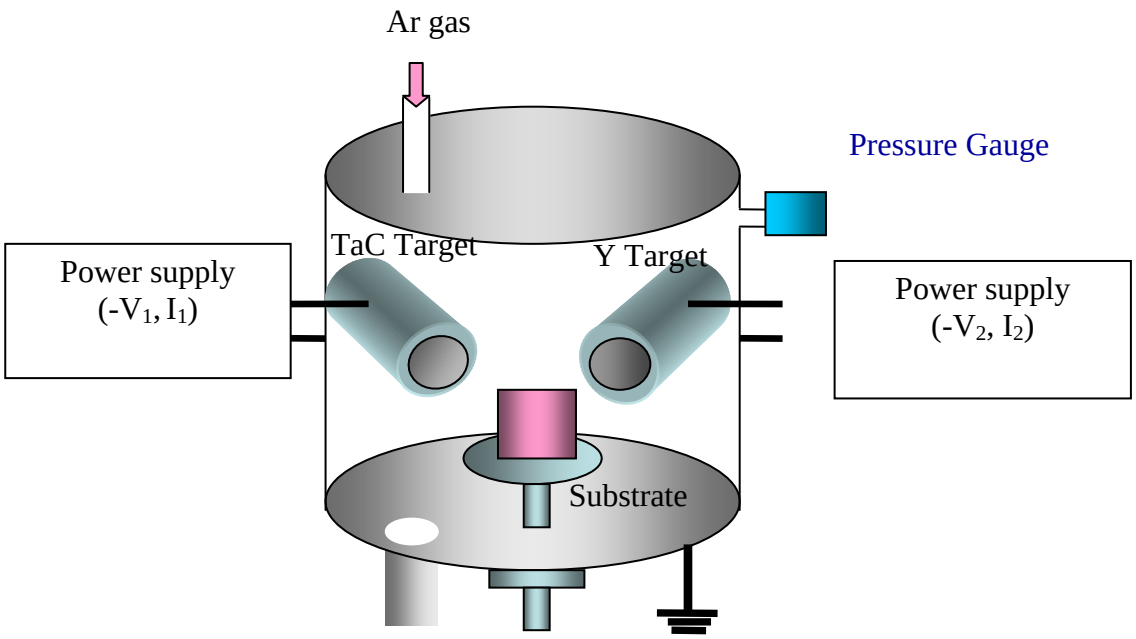

Figure 4.15: Schematic of dual magnetron sputtering system for growth $(TaC)_{1-x}Y_x$ films.

In the synthesis part the transition metal carbide in this work, the TaC and Y targets were used in the sputtering system. Inert Ar gas is introduced to the system as the sputtered gas. The flow rate is kept constant 20 sccm. The schematic diagram of the system is shown in Fig. 4.15. The composition of $(TaC)_{1-x}Y_x$ can be controlled by varying the power of the magnetrons power supplies. The stoichiometric forms of the compound, $(TaC)_{1-x}Y_x$, were calculated from the deposition rate. The density of TaC and Y target is 13.9 g/cm^3 and 4.472 g/cm^3, respectively. Therefore, the mol of TaC and Y is 0.072 and 0.05 mol, respectively. TaC contains Ta 1 mol and C 1 mol. The number of atoms of Ta and Y are $0.072\times6.02\times10^{23}$ and $0.05\times6.02\times10^{23}$ in volume 1 cm^3, respectively. Because the deposition rate of TaC and Y is individual, the percent of Y in $(TaC)_{1-x}Y_x$ can be calculated from

$$\frac{Y}{Ta+Y} = \frac{0.05R_y}{0.05R_y + 0.072R_{Ta}} \tag{4.1}$$

where R_{Ta} is the deposition rate of Ta

R_Y is the deposition rate of Y.

Multiple $(TaC)_{1-x}Y_x$ -gated MOS capacitors were prepared as follows: A 3-nm-thick SiO_2 film is formed on a p-type Si using a thermal process. 3.5-, 4.2-, and 4.9-nm-thick HfO_2, and a 4.9-nm-thick $HfSiO_x$ film with 60at.% Hf were deposited on top of SiO_2 film by a metal organic chemical vapor deposition (MOCVD) process. Post-deposition annealing was then carried out at 1050°C in N_2 ambient. Typically, a 150-nm-thick $(TaC)_{1-x}Y_x$ film with several x values was deposited on HfO_2 or $HfSiO_x$ film by horizontal magnetron sputtering method using TaC and Y targets. In order to decrease the whole resistance of gate electrode, a 100-nm-thick Pt was deposited on some $Ta_{1-x}Y_xC$ films. Post-annealing was performed at 500 and 600°C for 30s in N_2 after forming gas annealing (FGA) at 400°C in 3% H_2. In this case, H_2 gas is used to eliminate the dangling bond (Si^-), existing at the interface between Si and SiO_2. Each hydrogen molecule can passivate Si^- in the reaction [74].

$$H_2 + 2Si^- \rightarrow 2Si - H \tag{4.2}$$

The V_{fb} value was estimated from capacitance-voltage (C-V) characteristics at 500 kHz in room temperature using the program called MIRAI-ACCEPT [75].

To examine the structural properties and electrical resistivity of the film, a 100-nm-thick $(TaC)_{1-x}Y_x$ film were also prepared on SiO_2 (100 nm)/p-Si. The structure and chemical bond formation of the $(TaC)_{1-x}Y_x$ film were studied by x-ray diffraction (XRD) and x-ray photoelectron spectroscopy (XPS), respectively. The electrical resistivity of the films was measured by two probe method. The C-V measurements were performed to study the electrical properties of $(TaC)_{1-x}Y_x$ -gated MOS capacitors using Keithley 4200 SCS semiconductor parameter analyzer.

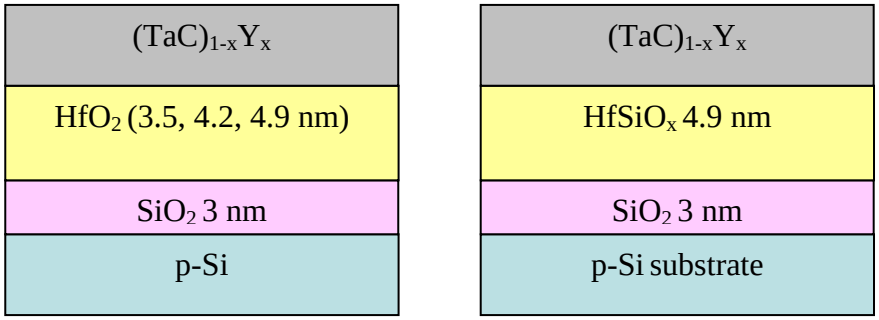

(a) (b)

Figure 4.19: Multiple $(TaC)_{1-x}Y_x$-gated MOS capacitors (a) on HfO_2 layer (b) on $HfSiO_x$ layer.

Table 4.4: The growth condition of $(TaC)_{1-x}Y_x$ and estimated composition by using deposition rate.

Power of TaC (W)	Power of Y (W)	Elemental composition
100	0	TaC
300	30	$(TaC)_{0.83}Y_{0.17}$
250	50	$(TaC)_{0.71}Y_{0.29}$
220	70	$(TaC)_{0.60}Y_{0.40}$
150	70	$(TaC)_{0.50}Y_{0.50}$
100	100	$(TaC)_{0.32}Y_{0.68}$
0	100	Y

The elemental composition of $(TaC)_{1-x}Y_x$ can be controlled by varying the power of TaC and Y**,** which the results are shown in Table 4.4.

The $(TaC)_{1-x}Y_x$ films consist of face center cubic (FCC) and disorder crystalline structures in $x \leq 0.4$ and $x \geq 0.5$, respectively, after annealing at 600 °C by XRD measurement as shown in Fig. 4.17. It seems that amorphous structure consists of rich Y content because it makes no-long-range order of the position. The (111) and (200) peaks of TaC shift toward the lower diffraction angle as x-value increases. It means that the lattice constant increases with an increasing Y content in $(TaC)_{1-x}Y_x$ films. No phase separation occurs between TaC and Y because the solid solution can be formed. This phenomenon indicates that Y atoms substitute some position of Ta atoms in TaC.

The resistivity of $(TaC)_{1-x}Y_x$ films is un-changed in the range $x \leq 0.5$ at 600 °C while the Y content at x = 0.68 increase with increasing annealing temperature as shown in Fig.4.18. It can be explained that an excess of Y atoms in $(TaC)_{0.32}Y_{0.68}$ make more impurity point defect.

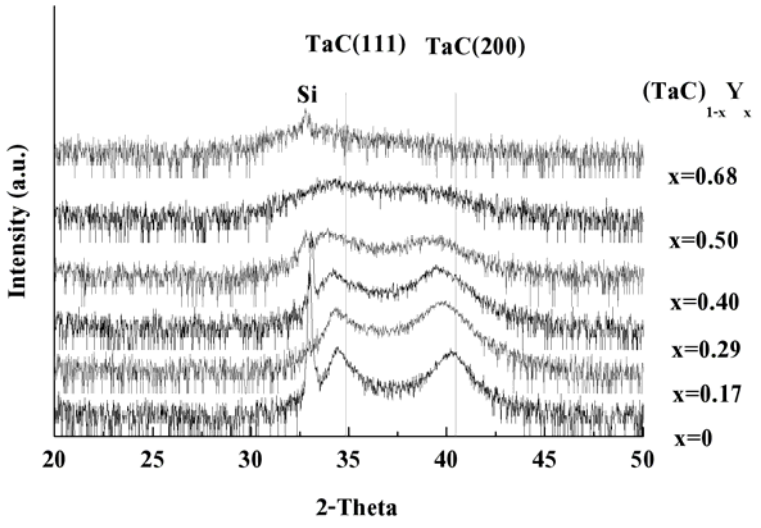

Figure 4.17: X-ray diffraction patterns of $(TaC)_{1-x}Y_x$ thin films on SiO_2/Si at various composition of x=0, 0.17, 0.29, 0.40, 0.50, and 0.68, respectively. All samples were annealed at 600°C [76].

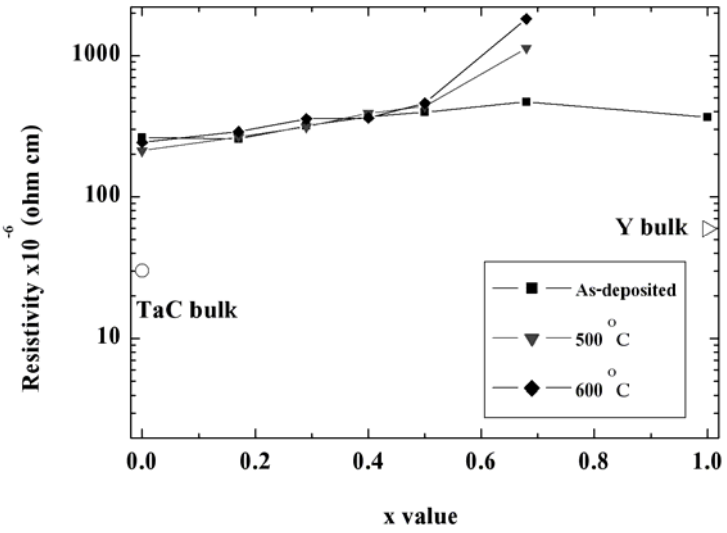

Figure 4.18: Resistivity of $(TaC)_{1-x}Y_x$ films on SiO_2/Si as a function of x value before and after annealing at 500 and 600°C. Open circle and triangle represent TaC and Y bulk data, respectively [76].

It is cleared that the C-V characteristics of $(TaC)_{1-x}Y_x$ /HfO_2(4.9nm)/SiO_2(3nm)/Si capacitors shift toward the negative direction with an increasing of Y content in films, as shown in Fig. 4.19. The effective work function ($\phi_{m,eff}$) value was determined by the EOT_{HfO2} thickness dependence of V_{fb}, as shown in Fig. 4.20.

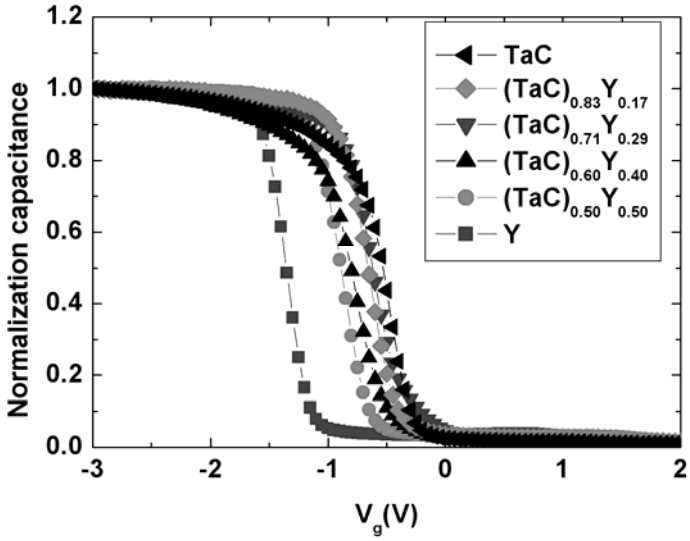

Figure 4.19: C-V characteristics of $(TaC)_{1-x}Y_x$ /HfO_2 (4.9 nm) /SiO_2 (3 nm)/Si MOS capacitors before annealing. X values in $(TaC)_{1-x}Y_x$ gate electrodes were varied from 0 to 1 [76].

The $\phi_{m,eff}$ tends to decrease as Y content increases. It can be varied from 4.27 eV to 4.81 eV. We found that the $\phi_{m,eff}$ can be easily controlled by changing Y content in $(TaC)_{1-x}Y_x$ films. Fig. 4.21 shows XPS peak position of Ta4f , C1s and O1s in as-deposited TaC film after sputtering 0 – 900 s. For C1s spectra, the absorbed carbon peak (285.5 eV) disappears after sputtering for 300 s while Ta-C peak (282.9 eV) remains in all sputtering times. For Ta4f spectra, the peaks of TaC and Ta_2O_5 component were observed in the as-deposited film and the TaC peak becomes stronger as sputtering time increases. However, Ta_2O_5 component still remains after sputtering for 900 s and it results in the high $\phi_{m,eff}$ value (4.70 eV).

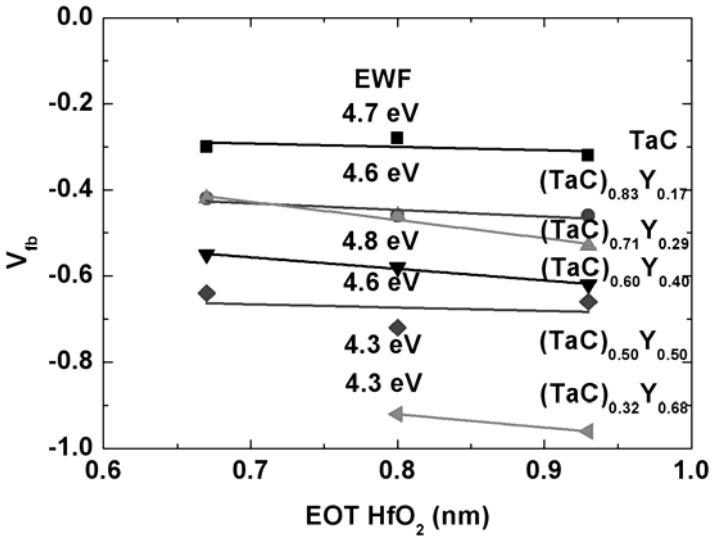

Figure 4.20: Relationship between Vfb and EOT of HfO_2 for HfO_2 MOS capacitors with $(TaC)_{1-x}Y_x$ gate electrode before annealing process. The $\phi_{m,eff}$ values were estimated by extrapolating to y-axis [76].

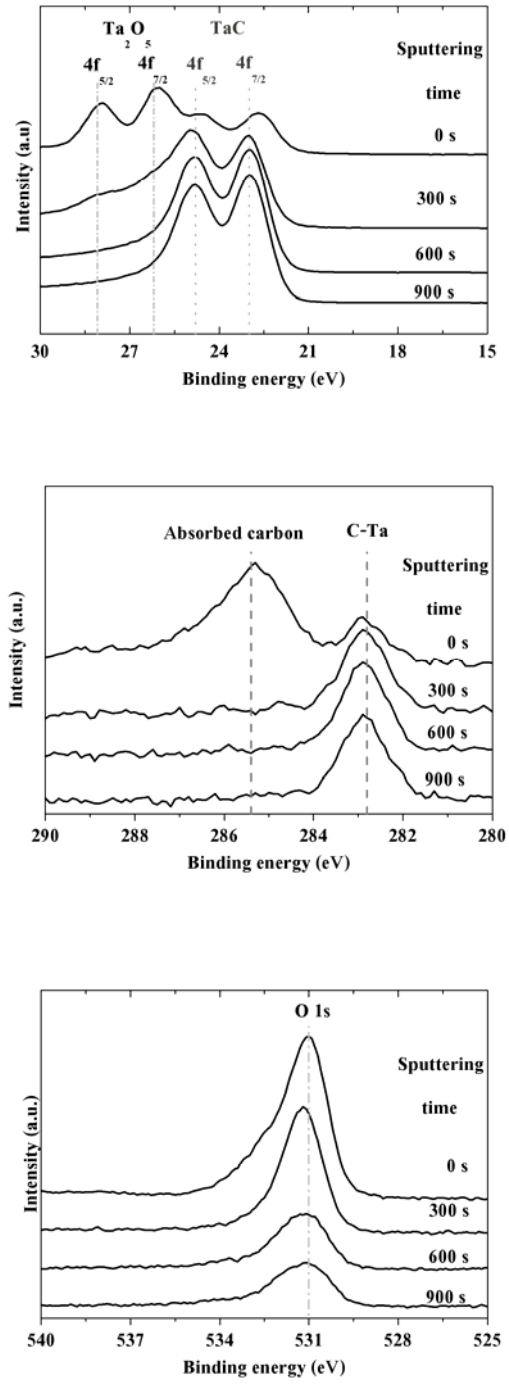

Figure 4.21: XPS spectra showed (a) Ta4f and (b) C1s (c) O1s positions in as-deposited TaC film on SiO_2/Si by changing sputtering time [76].

The flatband voltage (V_{fb}) change of $(TaC)_{1-x}Y_x$ gate capacitors with HfO_2 of 4.2 and 4.9 nm thicknesses are shown in Fig. 4.22. It is clear that the V_{fb} shifts toward negative direction as x value increases regardless of annealing temperature of 500 and 600 °C. However, the x-value is limited less than 0.4 because of high leakage current at 600 °C. In the case of $HfSiO_x$, we found that the change in V_{fb} has a similar behavior to in the case of HfO_2, These phenomena indicate that V_{fb} shift is not influenced by high-k material but it depends on Y content in $(TaC)_{1-x}Y_x$. The V_{fb} shift is approximate 0.5 V and 0.2V after annealing at 500 and 600 °C, respectively, as shown in Fig. 4.23.

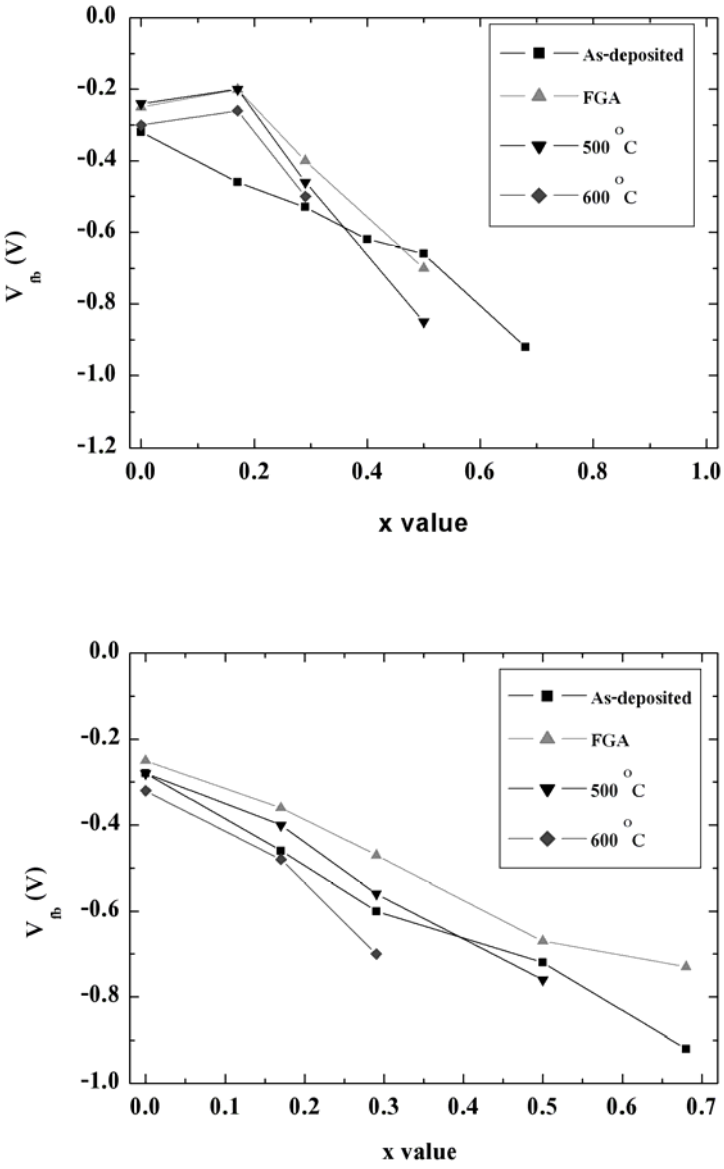

Figure 4.22: The V_{fb} change of $(TaC)_{1-x}Y_x$ -gated MOS capacitors with HfO_2 of (a) 4.9 and (b) 4.2 nm thicknesses as a function of x value, respectively. Post metal deposition annealing was performed at 500 and 600°C in N_2 after FGA at 400°C in H_2 [76].

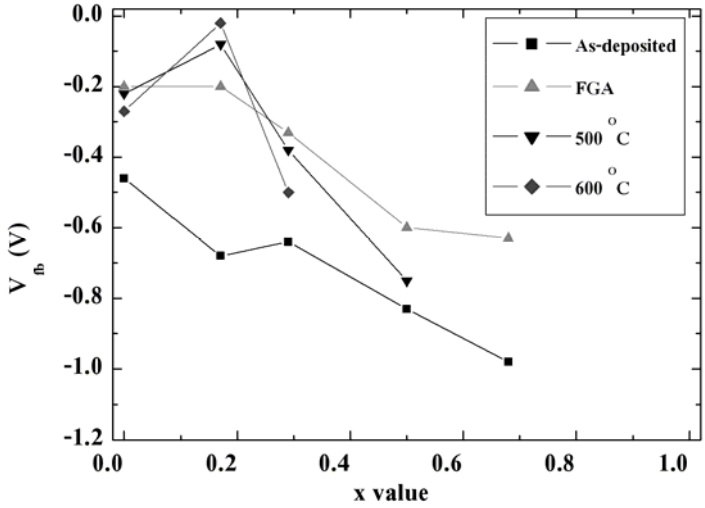

Figure 4.23: The V_{fb} change of $(TaC)_{1-x}Y_x$ -gated MOS capacitors with $HfSiO_x$ with 4.9 nm as a function of x value. Post metal deposition annealing was performed at 500 and 600°C in N_2 after FGA at 400°C in H_2 [76].

CHAPTER V
CONCLUSIONS

All transition metal nitride (chromium zirconium nitride) and transition metal carbide (tantalum yttrium carbide) films in this work were grown by magnetron sputtering system. We found that both of them could be high potential candidate materials in future industry for protective coating layer and n-metal gate electrode in gate-last process, respectively. As transition metal atoms substitute for another transition metal atom, solid solution could be formed in both chromium zirconium nitride and tantalum yttrium carbide thin films. There is no phase separation, even after post-annealing. It means both of them have a good thermal stability after annealing. For transition metal nitride, the structural properties, the resistivity and mechanical properties of chromium zirconium nitride can be controlled by varying the nitrogen partial pressure and the magnetron current. We found that 20% nitrogen partial pressure is optimizing condition for growth of this nitride thin film. Post-annealing of chromium zirconium nitride can help for an improvement of the mechanical properties. The substitution of zirconium atoms at chromium atom sites can be improved the hardness of films. The structural and mechanical properties of chromium zirconium nitride can be developed by ion-assistance and introduction of Cr interlayer between substrate and film. The development of structure occurred in 2 processes, the arrangement of atoms and the diffusion on surface. The (200) texture can be developed because of the dominant thermodynamic energy transferring energy and momentum from ions to surface. In contrast, (111) texture can be developed because of the introduction of Cr interlayer and the dominant kinetic energy. The increase in the kinetic energy of ions near the substrate moving to bombard the surface films affects the increase in the hardness. The Cr interlayer affects the re-arrangement of atoms on Cr layer in the way of low activation energy.

For transition metal carbide, we investigated the structural and electrical properties as a function of yttrium content in tantalum yttrium carbide gate electrodes for MOS capacitor with HfO_2 and $HfSiO_x$ dielectrics. We studied usefulness of $(TaC)_{1-x}Y_x$ films as n-metal gate electrode for hafnium oxide and hafnium silicate gate dielectrics. Yttrium atoms substitute for tantalum atoms in tantalum carbide. We observed that the structure of $(TaC)_{1-x}Y_x$ films was kept showing face center cubic

and amorphous structure in $x \leq 0.4$ and $x \geq 0.5$, respectively, without phase separation after annealing at 600 °C. The resistivity was almost constant in $x \leq 0.5$ even at 600 °C. For the first time we found that the flatband voltage can be controlled in the wide range of 0.5V by changing yttrium content in $(TaC)_{1-x}Y_x$ gate electrodes on hafnium oxide and hafnium silicate capacitors at 500 °C.

REFERENCES

[1] Wasa, K., and Hayakawa, S. 1992. Handbook of sputter deposition technology principles, technology and applications. New Jersey: Noyes Publications.

[2] Pogrebnjak, A.D., Shpak, A.P., Azarenkov, N.A., and Beresnev, V.M. July 2009. Review of topical problems structures and properties of hard and superhard nanocomposite coatings. Physics- Uspekhi 52:29-54.

[3] Fornics, L.E., Galindo, R.E., Sanchez, O., and Albella, J.M. May 2006. Growth of CrNx films by DC reactive magnetron sputtering at constant N2 / Ar gas flow. Surface and coatings technology 200: 6047-6053.

[4] Lin, J. et al. January 2009. A comparative study of CrN_x coatings synthesized by DC and pulsed DC magnetron sputtering. Thin solid films 517: 1887–1894.

[5] Shin, S.H. et al. August 2008. Cutting performance of CrN and Cr-Si-N coated end-mill deposited by hybrid coating system for ultra-high speed micro machining. Surface and coatings technology 202: 5613–5616.

[6] Aouadi, S.M., Maeruf, T., Twesten, R.D., Mihut, D.M., and Rohde, S.L. 2006. Physical and mechanical properties of chromium zirconium nitride thin films. Surface and coatings technology 200: 3411–3417.

[7] Kim, G.S., Kim, B.S., Lee, S.Y., and Hahns, J.H. November 2005. Structure and mechanical properties of Cr-Zr-N films synthesized by closed field unbalanced magnetron sputtering with vertical magnetron sources. Surface and coatings technology 200: 1669–1675.

[8] Lamni, R., Sanjines, R., Parlinska-Wojtan, M., Karimi, A., and F. Levy. 2005. Microstructure and nanohardness properties of Zr-Al-N and Zr-Cr-N thin films. Journal of vacuum science & technology A 23: 593–598.

[9] Khyzhun., O.Y. 1997. XPS, XES, and XAS studies of the electronic structure of substoichiometric cubic TaC_x and hexagonal Ta_2C_y carbides. Journal of alloys and compounds 259: 47.

[10] Nabatame, T. et al. 2008. Change in effective work function of Hf_xRu_{1-x} alloy gate electrode. Microelectronic engineering 85: 1524**.**

[11] Tse, K., and Robertson, J. 2006. Work function control at metal-oxide interfaces in CMOS. Materials science in semiconductor processing 9: 964.

[12] Schaeffer, J.K. et al. 2007. Tantalum carbonitride electrodes and the impact of

interface chemistry on device characteristics. Journal of applied physics 101: 014503.

[13] Gavartin, J.L., Shluger, A.L., Foster, A.S., and Bersuker, G.I. 2005. The role of nitrogen-related defects in high-k dielectric oxides: density-functional studies. Journal of applied physics 97: 053704.

[14] Park, T.J. et al. 2008. Effective work function tunability and interfacial reactions with underlying HfO_2 layer of plasma-enhanced atomic layer deposited TaC_xN_y films. Applied physics letter 92: 202902.

[15] Triyoso, D.H. et al. 2007. Atomic layer deposited TaC_y metal gates: Impact on microstructure, electrical properties, and work function on HfO_2 high-*k* dielectrics**.** Journal of applied physics 102:104509.

[16] Riedel, R. 2000. Handbook of ceramic hard materials, the Republic of Germany: Wiley-VCH.

[17] Rossnagel, S.M. 1991. This film process II. Academic Press Inc.

[18] Thornton, J.A. 1988. Physical vapor deposition. Semiconductor material and process technology handbook for very large scale integration (VLSI) and ultra large scale integration (ULSI), pp. 329-444. New Jersey: Noyes Publications.

[19] Chapman, B. 1980. Glow discharge process sputtering and plasma etching. New York: John Wiley & Sons.

[20] Sukkaneste Tungasmita. Growth of wide-band gap AlN and $(SiC)_x(AlN)_{1-x}$ thin films by reactive magnetron sputter deposition. Doctoral thesis, departmant of physics and measurement technology. Linkoping University.

[21] Greene, J.E. 2010. Thin film nucleation, growth, and microstructural evolution: an atomic scale view. Martin, P.M. Handbook of deposition technologies for films and coating science, applications and technology, pp. 554-616. United states. Elsevier Inc.

[22] Ohring, M. 1992. The materials science of thin film. California: Academic Press.

[23] Taha, A.S., and Hammad, F.H. June 1990. Application of the Hall-Petch relation to microhardness measurement on Al, Cu, Al-Mo, and Al-Cu alloys. Physica status solidi a 119: 455-462.

[24] Zhang, S., Sun, D., Fu, Y. and Du, H. 2003. Recent advances of superhard nanocomposite coating: a review. Surface and coatings technology 167: 113-119.

[25] Paskvale, S. March 2007. Document in seminar Properties of PVD hard coating. Faculty of mathematics and Physics, University of Ljubljana.

[26] Song, S.C. et al. 2007. Integration challenges and opportunities for nanometer scale dual meter gate CMOSFET. In Claeys, C. Iwai, H., Tao, M., Murota, J., Liou, J.J. and Deleonibus, S. (ed), USLI process integration 5, pp. 315-329. New Jersey: The Electrochemical Society, Inc.

[27] Sze, S.M., and Ng, K.K. 2007. Physics of semiconductor devices, Third edition. New Jersey: Wiley.

[28] Taur, Y., and Ning, T.H. 2009. Fundamental of modern VLSI devices, Second edition. New York: Cambridge university press.

[29] Neamen, D.A. 1992. Semiconductor physics and devices Basic principles. The United States of America: Richard D. Irin, INC.

[30] Houssa, M. et al. 2006. Electrical properties of high-k gate dielectrics: challenges, current issues and possible solutions. Materials science and engineering R 51: 37-85.

[31] Guha, S., and Narayanan, V. April 2009. High-k/ metal gate science and technology. The annual review of materials research. 39: 181-202.

[32] Nabatame, T. 12 April 2010. General Manager in national institute for materials science. Interview.

[33] Ota, H. et al. 2008. Inversion layer mobility in high-k dielectric MOSFETs intrinsic mobility degradation by electrric dipole at high-k/SiO_2 interface. Electrochemical society transaction 16: 67-75.

[34] Saito, S.I. el al. 2005. Remote-charge-scattering limited mobility in field-effect transistors with SiO_2 and Al_2O_3/ SiO_2 gate stacks. Journal of applied physics 98: 113706.

[35] Cullity, B.D., and Stock, S.R. 2001. Elements of x-ray diffraction, Third edition. New Jersey: Prentice-Hall.

[36] Fultz, B., and Howe, J.M. 2008. Transmission electron microscopy and diffracttometry of materials, Third edition. New York: Springer.

[37] Bhushan, B., and Kawata, S. 2007. Applied scanning probe methods VI characterization. Berlin Heidelberg: Springer-Verlag.

[38] Digital Instruments Inc. 1998. Support Note No.225. Santa Barbara, CA.

[39] Holt, D.B., and Yacobi, B.G. 2007. Extended defectd in semiconductors electronic properties, device effect and structure. New York: Cambridge

University Press.

[40] Goldstein, J.I. et al. 1992. Scanning electron microscopy and x-ray microanalysis, Second edition. New York: Plenum Press.

[41] Schweitzer, J. March 2011. Scanning electron microscope. Available from: http://www.purdue.edu/rem/rs/sem.htm

[42] Brandon, D., and Kaplan, W.D. 2001. Microstructural characterization of materials. England: Wiley & Son Ltd.

[43] Fischer-Cripps laboratories. 2009. Nanoindentation. Available from: http://ibisonline.au

[44] Sherman, D., and Brandon, D. 2000. Mechanical properties and their relation to microstructure. the Federal Republic of Germany: Wiley-VCH.

[45] Fischer-Cripps, A.C. 2004. Nanoindentation, Second Edition. Mechanical engineering series. New York: Springer.

[46] Rinde, J.A. August 1970. Poisson's ratio for rigid plastic foams. Journal of applied polymer science 14: 1913-1926.

[47] Sokolnikoff, I.S. 1983. Mathematical theory of elasticity, Second edition. Krieger: Malabar FL.

[48] Wikimedia foundation Inc. 2011. Scratch test. Available from: http://en.wikipedia.org/wiki/scratch_tester.

[49] Watts, J.F., and Wolstenholme, J. 2003. An Introduction to surface analysis by XPS and AES. Great Britain: John Wiley& Sons, Inc.

[50] van der Pauw, L.J. 1958. A method of measuring specific resistivity and hall effect of discs of arbitrary shape. Philips Research Reports 13 No.1:1-9.

[51] Stauffer, L. Febuary2009. Fundamentals of semiconductors C-V measurements. Ohio: Keithley Instrument, Inc.

[52] Ong, D.G. 1986. Modern MOS technology: processes, devices and design. Singapore: McGraw-Hill Book Co.

[53] Pattira Homhuan, Surasing Chaiyakun, Rattaporn Thonggoom, Nurot Panich, and Sukkaneste Tungasmita. 2010. Growth and structural characterizations of nanostructured chromium-zirconium-nitride thin films for tribological applications. Material transactions, The Japan institute of materials51:1651-1655.

[54] Lee, Y.K., Kim, J.Y., Lee, Y.K., Lee, M.S, Kim, D.K., and Jin, D.Y et al. January 2002. Surface chemistry of non-stoichiometric TiN_x films grown on

(100)Si substrate by DC reactive magnetron sputtering. Journal of crystal growth 234: 498-504.

[55] Combadiere, L., and Machet, J. January 1996. Reactive magnetron sputtering deposition of TiN films I: influence of the substrate temperature on structure composition and morphology of films. Surface and coatings technology 88:17-27.

[56] Vaughan, W.H., Leivo, W.J., and Smoluchowski, R. May 1958. Density and hardness changes produced by plastic deformation in KCl crystals. Physical review 110: 652-657.

[57] Hulman, L., Helmersson, U., Barnett, S.A., Sundgren, J.-E., Greene, J.E. 1987 Low-energy ion irradiation during film growth for reducing defect densities in epitaxial TiN(100) films deposited by reactive-magnetron sputtering. Journal of applied physics 61: 552-555.

[58] Huang, J.-H., Lau, K.-W., and Yu, G.-P. February 2005. Effect of nitrogen flow rate on structure and properties of nanocrystalline TiN thin films produced by unbalance magnetron sputtering. Surface and coatings technology 191: 17-24.

[59] Logothetidis, S., Alexandrou, I., and Kokkou, S. March 1996. Optimize of TiN thin film growth with in sito monitoring: the effect of bias and nitrogen flow rate. Surface and coatings technology 80: 66-71.

[60] Huang, P.-K., and Yeh, J.-W. 2009. Effect of substrate bias on structure and mechnical properties (AlCrNbSiTiV)N coatings. Journal of physics D: applied. physics 42: 115401.

[61] Niu, E.W. et al. 2007. Influence of substrate bias on structure and properties of ZrN films deposited by cathodic vacuum arc. Materials science and engineering A 460-461:135-139.

[62] Sundgren, J.-E. 1990. Ion-assisted film growth: modification of structure and chemistry. Vacuum 41: 1347.

[63] Gall, D., Kodambaka, S., Wall, M.A., Petrov, I., and Greence, J.E. 2003 Pathways of atomic processes on TiN(001) and (111) surfaces during film growth: and ab initio study. Journal of applied physics 93: 9086.

[64] Lide, D.R. 1997. Handbook of Chemistry and Physics, 77th edition. Boca Raton: CRC Press.

[65] Shew, B.-Y., Huang, J.-L., and Lii, D.-F. January 1997. Effect of R.F. bias and nitrogen flow rates on the reactive sputtering of TiAlN film. Thin Solid Films

293: 212-219.

[66] Petrov, I., Barba, P.B., Hultman, L., and J.E. Greene. September 2003. Microstructural evolution during film growth. Journal of vacuum science and technology A21: S117.

[67] Greene, J.E., Sundgren, J.-E., Hultnan, L., Petrov, I., and Bergstom, D.B. 1995. Development of preferred orientation in polycrystalline TiN layers grown by ultrahigh vacuum reactive magnetron sputtering. Applied physics letters 67: 2928.

[68] Chang, H.-W., Huang, P.-K., Yeh, J.-W., Davison, A., Tsau, C.-H., and Yang, C.-C. April 2008. Influence of substrate bias, deposition temperature and post-deposition annealing on the structure and properties of multi-principle-component (AlCrMoSiTi)N coating. Surface and coatings technology 202: 3360-3366.

[69] Daniel, R., Martinschitz, K.J., Keckes, J., Mitterer, C. 2009. Journal of physics D: applied physics 42: 075401.

[70] William, D., and Callister, Jr. 2003. Material science and engineering an introduction, Sixth edition. Great Britain: John Wiley&Sons.

[71] Huang, J.-H., Tsai, Y.-P., and Yu, G.-P. November 1999. Effect of processing parameters on the microstructure and mechanical properties of TiN film on stainless steel by HCD ion plating. Thin Solid Films 355-356: 440-445.

[72] Heiland, W. 1992. The interaction of slow ions with surfaces. Solid state phenomena 27:107-128.

[73] Manika, I., and Manika, J. 2008. Effect of substrate hardness and film structure on indentation depth criteria for film hardness testing. Journal of physics D: applied physics 41:074010.

[74] Fleetwood, D.M. 2002. Effects of hydrogen transport and reactions on microelectronics radiation response and reliability 42: 523.

[75] Yasuda, N., Ota, H., Horikawa, T., Nabatame, T., Satake, H., and. Toriumi, A. et al. 2005. Ext. Abstr. Solid State Devices and Materials p. 250.

[76] Pattira Homhuan, Nabatame, T., Chickyow, T. and Sukkaneste Tungasmita. January 2011. Effect of Y content in $Ta_{1-x}Y_xC$ gate electrodes on V_{fb} control for Hf-based high-k. Dielectric thin films for future electron devices: science and technology IWDTF 2011. Tokyo, Japan. pp. 9-10. 2011.

APENDICES

APPENDIX A

LIST OF CONFERENCES (Oral Presentation)

1. **5th Thailand Materials Science and Technology Conference** at Miracle Grand Convention Hotel, Bangkok on 16-19 September 2008.
Title "Effect of Nitrogen Partial Pressure on the Structural Properties of $(Cr_xZr_{1-x})N$ Thin Films"
2. **International Conference on Nanoscience and Technology** in Beijing, China on 1-3 September 2009.
Title "Growth and Structural Characterization of Nanostructure CrZrN Thin Films on Tribological Application"
3. **The 71th Fall Meeting of The Japan Society of Applied Physics** in Nagasaki University, Japan on 14-17 September 2010.
Title "Electrical Properties of $Ta_{1-x}Y_xC$ on Hf-based high-k as n-metal gate electrode"
4. **International Workshop on Dielectric Thin Films for Future Electron Devices: Science and Technology** in Tokyo Institute of Technology, Japan on 20-21 January 2011.
Title "Effect of Y Content in $Ta_{1-x}Y_xC$ Gate Electrodes on V_{fb} Control for Hf-based High-k"

SCHOLARSHIPS

2007-2010 The Commission on Higher Education No.PhD-SW-INV-20060105
2009-2010 Graduate Thesis Grant
Graduate School, Chulalongkorn University
2010 **NIMS Internship Program**
National Institute for Materials Science, Japan

APPENDIX B

Paper 1: 2010. Growth and structural characterizations of nanostructured chromium zirconium-nitride thin films for tribological applications. Material transactions, The Japan institute of materials 51:1651-1655.

Materials Transactions, Vol. 51, No. 9 (2010) pp. 1651 to 1655

Growth and Structural Characterizations of Nanostructured Chromium-Zirconium-Nitride Thin Films for Tribological Applications

Pattira Homhuan[1,*1], Surasing Chaiyakun[2], Rattaporn Thonggoom[3,4], Nurot Panich[5] and Sukkaneste Tungasmita[5,6,*2]

[1]*Nanoscience and Technology, Graduate School, Chulalongkorn University, Bangkok, 10330, Thailand*
[2]*Department of Physics, Faculty of Science, Burapa University, Chonburi, 20131, Thailand*
[3]*Department of Chemistry, Faculty of Science, Mahidol University, Bangkok, 10400, Thailand*
[4]*Center for Surface Science and Engineering, Faculty of Science, Mahidol University, Bangkok, 10400, Thailand*
[5]*Center of Innovative Nanotechnology, Chulalongkorn University, Bangkok, 10330, Thailand*
[6]*Department of Physics, Faculty of Science, Chulalongkorn University, Bangkok, 10330, Thailand*

Nanostructured Cr-Zr-N thin films were grown on Si(100) substrates in a mixture of Ar and N_2 plasma. The nitrogen partial pressure was varied to produce and control the stoichiometric forms obtained. All the Cr-Zr-N films exhibited a nanostructure with an average grain size of less than 10 nm, as determined by X-ray diffractogram analysis, and were formed in the solid-solution. As the contents of nitrogen in the film increased, it lead to changes in the crystal texture and competitive growth. The maximum root mean square roughness was 7.87 nm at a 20% nitrogen partial pressure and the roughness tended to decrease as the grain size decreased. The nano-indentation showed that the films grown at a 20% nitrogen partial pressure and annealed at 700°C had the highest reduced modulus and hardness at 349.2 and 35.1 GPa, respectively. The mechanical properties of films can be improved by a post-annealing heat treatment. With respect to the electrical properties of these films, the sheet resistance, which is related to the defect level, tended to increase as the nitrogen partial pressure increased.
[doi:10.2320/matertrans.M2010140]

(Received April 20, 2010; Accepted June 10, 2010; Published July 28, 2010)

Keywords: *magnetron sputtering, nanostructure, hard coating, protective thin films*

1. Introduction

Transition-metal-nitride thin films deposited by physical vapor deposition (PVD) have been developed and used as mechanically and chemically protective layers for industrial applications for many years. The cubic-base structural chromium nitride (CrN) is a more recent and interesting choice of such layers due to its well-matched properties to some industrial requirements, especially those that require a hard coating and for tribological applications. This is largely due to the fact that CrN films have a high hardness, high wear- and corrosion-resistance, and also have a low friction-coefficient.[1,2] Adding one more metal element to form Cr-based ternary nitride films has been reported to show improved properties compared to the binary CrN compound.[3–5] However, in the case of Zn, as an example added tertiary metal element, there is an apparent lack of important information about the properties of the ternary Cr-Zr-N films derived from various growth parameters, despite the fact that these are the key variables for engineering the desired properties of the material. In this work, we explored the role of the nitrogen partial pressure during film formation, and that of the post-process annealing temperature, on the structural, mechanical and electrical properties of the resultant Cr-Zr-N film.

2. Experimental Procedures

Ternary Cr-Zr-N films were grown by dual unbalanced D.C. magnetron sputtering with horizontal magnetron sources on Si(100) substrates. All films were produced from pure Cr and Zr targets in a defined mixture of Ar and N_2 plasma. The base pressure in this reactive sputtering system was pumped down to 5×10^{-5} mbar. The partial pressure of nitrogen ($N_2/Ar + N_2$) during the process was varied to produce various compositions of films. During the formation of films, the discharge current of each target was controlled at a constant 0.5 A. All films were grown without an extra heat source, except the transferred energy at the substrate surface from the collision of adatoms and plasma species. In this work, the substrate was at a floating potential. The thickness of all the films obtained was in the range of 0.9–2.0 μm, depending on the nitrogen partial pressure used during their growth.

The elemental composition of each film was measured by energy dispersive spectroscopy (EDS) (Oxford INCA), coupled to a scanning electron microscope (JEOL JSM-6480LV), that was also used for scanning electron microcopy (SEM). For the structural characterization of films, the specimens were characterized by X-ray diffraction (XRD) (Brukers D8 Discover) with Cu Kα ($\lambda = 0.15406$ nm) as the X-ray source. The cross-sectional microstructure was investigated by transmission electron microscopy (TEM) (JEOL JEM-2010 200 kV transmission electron microscope). The surface topography was investigated by atomic force microscopy (AFM) (Veeco Nanoscope-IV).

The hardness and reduced modulus were both measured using a Micro Material Nano Test in the constant depth mode with a Berkovich pyramidal indenter tip. To avoid the effect of substrate, the depth of indentation was limited to less than 1/10 that of the film thickness, which in this case meant the depth was taken at about 100 nm. The sheet-resistance of the film material was evaluated by the van der Pauw method. The

*[1]Graduate Student, Chulalongkorn University
*[2]Corresponding author, E-mail: Sukkaneste.t@chula.ac.th

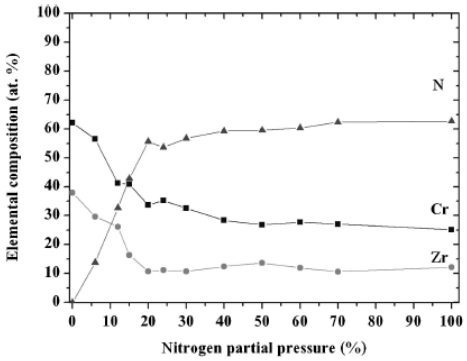

Fig. 1 Elemental concentrations of Cr-Zr-N films formed with different nitrogen partial pressures. Elemental concentrations are shown for N (triangles), Cr (squares) and Zr (circles).

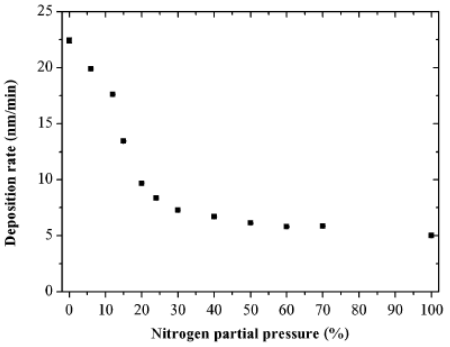

Fig. 2 Deposition rate of Cr-Zr-N films as a function of the nitrogen partial pressure.

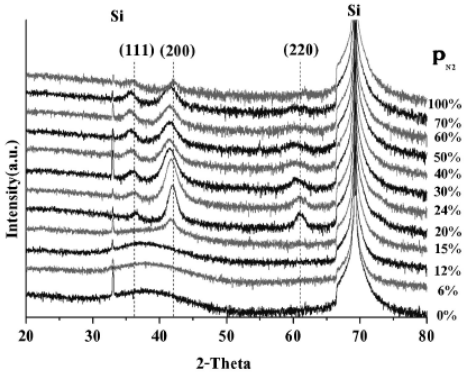

Fig. 3 Representative XRD spectra of Cr-Zr-N films grown at the indicated different nitrogen partial pressures.

stoichiometric Cr-Zr-N films grown at a 20% nitrogen partial pressure were used for the study of the effect of the post-growth annealing temperature under an Ar flow at vacuum pressure for 1 h, and then cooled down. The ramping rate of the annealing reaction was 5°C/min.

3. Results and Discussion

3.1 Effect of nitrogen partial pressure

3.1.1 Chemical composition

The elemental concentrations of Cr, Zr and N in the as-deposited films on silicon (100) substrates derived under different nitrogen partial pressures are shown in Fig. 1. The nitrogen composition in the films increased essentially linearly with increasing nitrogen partial pressure up to a nitrogen partial pressure of 20%, and thereafter remained almost constant and largely numerically and statistically independent of the nitrogen partial pressure. This represents the saturated condition for nitrogen atoms incorporation into the film material. Moreover, at all nitrogen partial pressures, there was a higher concentration of Cr than Zr, because Cr has a higher sputtering yield compared to that for Zr.[6] By increasing the nitrogen partial pressure, the reaction rate between nitrogen and metal at the target surface increases, which causes the sputtered nitrogen atoms and some of the metal-nitrogen cluster particles from the surface target to also increase.[7] In contrast, the relative proportion of sputtered Zr and Cr atoms from the surface target that form films decreases due to the increased coverage of nitrogen on the surface, resulting in the formation of metal nitride on the surface of the metallic target. The sputter yield for the nitride material at the target surface is much lower than that for the metal, which causes the deposition rate of films to decrease as the percentage of nitrogen partial pressure increases (see Fig. 2).

3.1.2 Structural properties

Figure 3 shows representative X-ray diffraction (XRD) spectra of the Cr-Zr-N films grown under the different nitrogen partial pressures, plotted on a semi-log scale. Since the Cr-Zr-N ternary compound came from the combination of CrN and ZrN materials, which alone both have a rock-salt NaCl type crystal structure, then the Cr-Zr-N also seems to retain a NaCl-like crystal structure. The peak positions for some major orientations of the Cr-Zr-N materials as a function of the Zr/Cr ratio have been calculated and presented elsewhere.[4] Here, according to EDS results, the composition of the material becomes stable after a 20% nitrogen partial pressure was applied and exhibits a pattern similar to the $Cr_{0.7}Zr_{0.3}N$ form in the ICDD 03-065-9004 database, with a NaCl-like structure. The $Cr_{0.7}Zr_{0.3}N(200)$ form starts to develop from a nitrogen partial pressure of 15%, whilst the (200) plane is the preferable orientation when formed over and above a 15% nitrogen partial pressure because of the dominant surface energy. The $Cr_{0.7}Zr_{0.3}N(200)$ is more stable and has the lowest surface energy.[8] However, the lowest strain energy is found with $Cr_{0.7}Zr_{0.3}N(111)$ and is the preferred orientation for CrN at low temperature growth.[9] Accordingly, the development of texture in the Cr-Zr-N films can be changed from that of CrN alone by control of the ternary metal and nitrogen partial pressure. This can be explained by re-nucleation, due to the addition of zirconium in the films.[10] Whilst the formation (detection) of both the $Cr_{0.7}Zr_{0.3}N(111)$ and the $Cr_{0.7}Zr_{0.3}N(220)$ forms started to appear at a 20% nitrogen partial pressure, as the nitrogen partial pressure increases

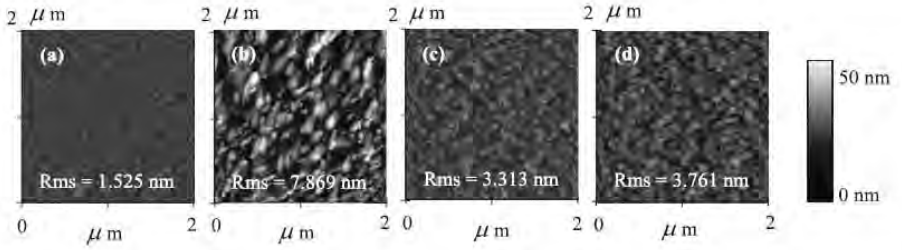

Fig. 4 Representative AFM images of Cr-Zr-N films formed under different nitrogen partial pressures of (a) 6%, (b) 20%, (c) 50% and (d) 100%.

further above 20% the position of these peaks shifts slightly towards the lower diffraction angles. This may be related to an increase in the compressive stress in the film due to the formation of a solid solution.[10] In addition, changes in the atomic density of the crystalline films can be considered. The density values of (200), (220) and (111) represent 4, 2.83 and 2.31 at/a^2, respectively. As the nitrogen partial pressure increases, so the adatoms are arranged to form films in lower density planes because the mobility of the adatoms is limited, and the energy of sputtered atoms decreases with increasing in the nitrogen partial pressures.[11]

The size of the formed grains was evaluated from the XRD peaks using the Scherer formula. All films have a grain size of less than 10 nm, but are perhaps even smaller since this value ignores the fact that the peak can be broad from the residual stress.[12] Therefore, the result indicates that all the films were conform to a Zone 1 model in the Thornton's structure zone model, with a low substrate temperature. In this zone, adatoms have a low surface diffusion because of a low substrate temperature and, since the adatoms are insufficient to overcome the shadowing effect, the films have a typical small-width columnar structure with voids with a rough surface.[13,14]

3.1.3 Cross-sectional and surface morphology

The surface morphology of the Cr-Zr-N films, as evaluated by AFM, as a function of the nitrogen partial pressure is shown in Fig. 4. The maximum root mean square roughness was 7.87 nm at a 20% nitrogen partial pressure, because of the competition among the Cr-Zr-N(111), (200) and (220), whilst the roughness tended to decrease as the grain size decreased.[15] A typical TEM micrograph of a Cr-Zr-N film grown at a 20% nitrogen partial pressure is shown in Fig. 5, along with an electron diffraction pattern. The microstructure of the film has a clear dense columnar structure, with some voids visible in the film material, whilst the average domain size is about or less than 10 nm. This particle domain size conforms well to that calculated from the XRD data.

3.1.4 Mechanical properties

With respect to the mechanical properties of hard coatings, the hardness and reduced modulus are the two most important properties of films and so were evaluated. Both the hardness and the reduced modulus of the Cr-Zr-N films, plotted as a function of the nitrogen partial pressure, were maximal when formed under a 20% nitrogen partial pressure (Fig. 6). At their maximum hardness and reduced modulus (30.0 and 324.1 GPa, respectively), they were nearly stoichiometric

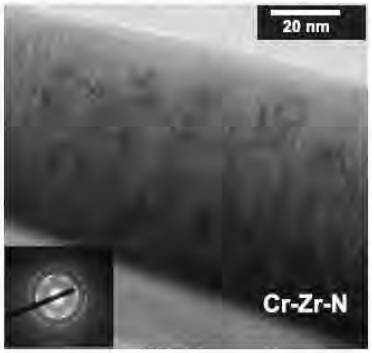

Fig. 5 Representative cross-sectional micrograph of a Cr-Zr-N film formed at a 20% nitrogen partial pressure, with an electron diffraction pattern shown in the insert.

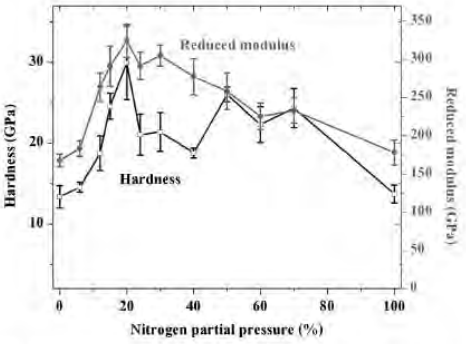

Fig. 6 Hardness and reduced modulus of Cr-Zr-N films as a function of the nitrogen partial pressure.

with a $Zr_{0.3}Cr_{0.7}N$ form that was in good agreement with that for ICDD 03-065-9004 in the database. From these results the roughness and grain diameter appear to be related to the hardness, as there is competition among (111), (200) and (220) planes. Moreover, the hardness strongly depends on the nitrogen contents in the films, as shown by the dose-dependence to the nitrogen partial pressure over from 0 to 20% range. This maximum hardness of the Cr-Zr-N film, when grown at a 20% nitrogen partial pressure, consists of

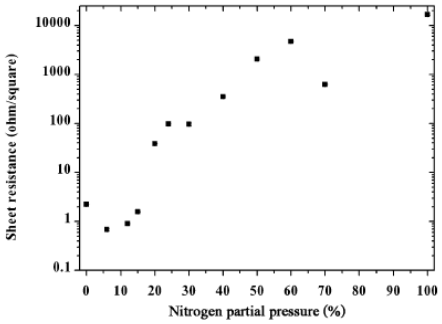

Fig. 7 The sheet resistance of Cr-Zr-N films developed with different nitrogen partial pressures.

the maximum amount of nitrogen completely bonded with metallic atoms.[16] However, that it then declines with further increases in nitrogen partial pressures, rather than remains at same saturation level, is due to the fact that higher partial pressures of nitrogen lead to a larger excess of nitrogen in the films located in the interstitial sites. This form of solid solution has a high hardness because the Zr atoms, which substitute for the Cr atoms in the face-center-cubic-structure, are limited to the mobility of dislocation.

The strength of adhesion between each of the different Cr-Zr-N films and the silicon (100) substrate was tested by nano-scratch, where the critical load is determined by a sudden change in the penetration depth in scratch tests. By this method, a maximum critical load (L_C) of 2.1 N was obtained with films produced at a 15% nitrogen partial pressure, and decreased thereafter at higher nitrogen partial pressures (data not shown). Thus, Cr-Zr-N films grown at a 15% nitrogen partial pressure had the best adhesion to the silicon (100) substrate. That the adhesion of films tended to decrease as the nitrogen partial pressure was increased is because the adatoms under these conditions have less energy to form films.

3.1.5 The electrical properties

The observed relationship between the Cr-Zr-N sheet resistance and the nitrogen partial pressure was almost linear with the sheet resistance increasing markedly as the nitrogen partial pressure increases (Fig. 7). The change in the sheet resistance is inversely proportional to the mean free path of conduction electrons, which relates to the microstructure and defect of the films.[17] Therefore, a lower sheet resistance is likely to mean that there are fewer defects in the film. Initially, Cr-Zr-N films, grown at a low nitrogen partial pressure, have a lower sheet resistance than Cr-Zr films because the nitrogen atoms incorporate into the films and bond with the Cr and Zr atoms. After saturation a higher nitrogen content in the films then makes for more impurity point defects, which can be found in the solid solution, because the excess of either nitrogen or metal atoms can situate on the interstitial site or grain-boundary.[18,19] When the partial pressure of nitrogen increases, there are many grain-boundaries in the film because the adatoms do not have enough energy to re-nucleate the crystallographic orientation. With more nitrogen incorporate in the film structure, the material shows a ceramic-like property. Therefore, over-stoichiometric films exhibit the highest sheet resistance than the other films.

Table 1 The properties of the Cr-Zr-N films grown at a 20% nitrogen partial pressure and subsequentially treated at different annealing temperatures.

Annealing Temp (°C)	Composition	Hardness (GPa) (H)	Reduced modulus (GPa) (E)	H/E*
0	$Cr_{0.33}Zr_{0.11}N_{0.56}$	30.0 ± 4.6	324.1 ± 21.7	0.092
300	$Cr_{0.31}Zr_{0.11}N_{0.58}$	30.0 ± 3.8	320.3 ± 14.0	0.094
500	$Cr_{0.35}Zr_{0.12}N_{0.53}$	33.3 ± 3.2	323.7 ± 23.8	0.102
700	$Cr_{0.32}Zr_{0.11}N_{0.57}$	35.1 ± 4.7	349.2 ± 18.6	0.101

*H/E = The ratio between hardness (GPa) and reduced modulus (GPa)

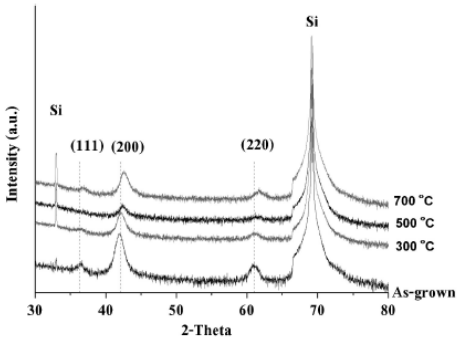

Fig. 8 Representative XRD spectra of Cr-Zr-N films grown at different annealing temperatures.

3.2 Effect of annealing temperature

Cr-Zr-N films grown at a 20% nitrogen partial pressure were then annealed at 300, 500 or 700°C to investigate the thermal stability of the films formed. With respect to the elemental composition, these did not significantly change after annealing (Table 1).

Figure 8 shows the typical XRD spectra of Cr-Zr-N films grown at a 20% nitrogen partial pressure with different post-annealing temperature treatment, plotted on a semi-log scale. The (200) plane remains the preferred orientation in all samples, and the diffraction peaks shift towards the higher diffraction angles as the annealing temperature increases, indicating that the lattice constant decreases as the annealing temperature increases. This is presumably because nitrogen atoms can diffuse from the grain boundary or the interstitial site to empty lattice sites.[20] Still, there is no phase separation after annealing at 700°C, indicating the thermodynamic stability of these films.

The hardness tends to increase as the annealing temperature increases, reaching a maximum reduced modulus and hardness of 349.2 and 35.1 GPa, respectively, after annealing at 700°C for 1 h (Table 1). The post-annealing treatment makes the modification of grain boundary of the film structure. Since the films were grown at low temperatures, all of them exhibited typical fine columnar structure. The

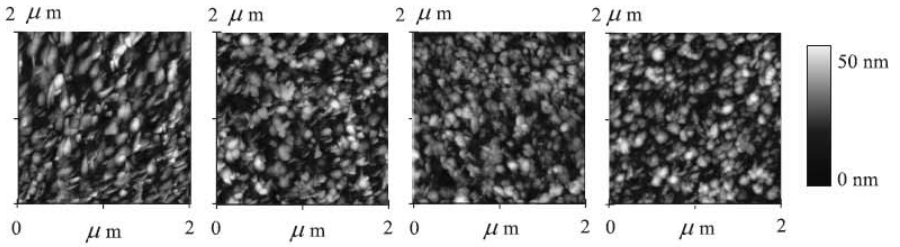

Fig. 9 Representative AFM images of Cr-Zr-N films; (a) as-deposited specimen, and specimens annealed at (b) 300°C, (c) 500°C and (d) 700°C.

post-annealing process can cause lattice vibration and introduces grain boundary annihilation mechanism. This results in an increasing of domain width and the changing in crystal structure.

The wear resistance of the films can be found from the ratio between the hardness and modulus,[21] and revealed that Cr-Zr-N films grown at a 20% nitrogen partial pressure and annealed at 500°C had the maximum value (highest wear resistance). After annealing, the RMS roughness was not changed (Fig. 9).

4. Conclusions

Chromium zirconium nitride films were grown at different nitrogen partial pressures (0–100%) on silicon (100) substrates. The nitrogen partial pressure was observed to play an important role in the stoichiometry, microstructure, deposition rate, surface morphology, sheet-resistance and hardness of the obtained Cr-Zr-N films due to the incorporation of nitrogen into the films. This phenomenon leads to the creation, and competitive growth, of the texture and surface roughness of the films. The films developed from a random oriented crystalline structure to a texture-crystalline structure at nitrogen partial pressures of 15%. The solid solution material was formed without any evidence of phase separation between the CrN and the ZrN. The hardness of the film did not seem to significantly depend on the content of nitrogen, but rather was related to the equilibrium site. The $Cr_{0.32}Zr_{0.11}N_{0.57}$ film, grown at a 20% nitrogen partial pressure and annealed at 700°C, had the highest hardness and reduced modulus. The sheet resistance of Cr-Zr-N films tended to increase with increasing nitrogen partial pressure. The films had thermal stability up to 700°C.

Acknowledgements

The authors would like to thank Mr. Nuttapong Parncharoenthaworn for helping measure the nanoindentation and The Commission on Higher Education and Graduate Thesis Grant for financial support that enabled this research work to be performed.

REFERENCES

1) J. Lin, Z. L. Wu, X. H. Zhang, B. Mishra, J. J. Moore and W. D. Sproul: Thin Solid Films **517** (2009) 1887–1894.
2) S. H. Shin, M. W. Kim, M. C. Kang, K. H. Kim, D. H. Kwon and J. S. Kim: Surf. Coat. Technol. **202** (2008) 5613–5616.
3) S. M. Aouadi, T. Maeruf, R. D. Twesten, D. M. Mihut and S. L. Rohde: Surf. Coat. Technol. **200** (2006) 3411–3417.
4) G. S. Kim, B. S. Kim, S. Y. Lee and J. H. Hahns: Surf. Coat. Technol. **200** (2005) 1669–1675.
5) R. Lamni, R. Sanjines, M. Parlinska-Wojtan, A. Karimi and F. Levy: J. Vac. Sci. Technol. A **23** (2005) 593–598.
6) G. E. McGuire (Ed): *Semiconductor Materials and Process Technology Handbook for Very Large Scale Integration (VLSI) and Ultra Large Scale Integration (ULSI)*, (Noyes Publications, New Jersey, 1988) p. 373.
7) S. Hofmann: Thin Solid Films **191** (1990) 335–348.
8) J. L. Ruan, J. L. Huang, J. S. Chen and D. F. Lii: Surf. Coat. Technol. **200** (2005) 652–1658.
9) P. Homhoul, C. Thavornthira, S. Chaiyakun and S. Tungasmita: J. Sci. Res. Chula Uni. **33** (2008) 43–49.
10) G. Ababias: Surf. Coat. Technol. **202** (2008) 2223–2235.
11) L. Combadiere and J. Machet: Surf. Coat. Technol. **88** (1996) 17–27.
12) S. Ulrich, H. Holleck, J. Ye, H. Leiste, R. Loos, M. Stuber, P. Pesch and S. Sattel: Thin Solid Films **437** (2003) 164–169.
13) S. PalDey and S. C. Deevi: Mater. Sci. Eng. A **342** (2003) 58–79.
14) G. E. McGuire (Ed): *Semiconductor Materials and Process Technology Handbook for Very Large Scale Integration (VLSI) and Ultra Large Scale Integration (ULSI)*, (Noyes Publications, New Jersey, 1988) p. 415.
15) Z. X. Song, Y. Wang, C. J. F. Wang, C. L. Liu and K. W. Xu: Surf. Coat. Technol. **202** (2007) 5412–5415.
16) R. D. Arnell, J. S. Colligon, K. F. Minnebaev and V. E. Yurasova: Vacuum **47** (1996) 425–431.
17) Y. K. Lee, J. Y. Kim, Y. K. Lee, M. S. Lee, D. K. Kim, D. Y. Jin, T. H. Nam, H. J. Ahn and D. K. Park: J. Crystal Growth **234** (2002) 498–504.
18) L. Hulman, U. Helmersson, S. A. Barnett, J.-E. Sundgren and J. E. Greene: J. Appl. Phys. **61** (1987) 552–555.
19) D. William and Jr. Callister: *Material Science and Engineering an Introduction 6 ed.*, (John Wiley&Sons, 2003) p. 77.
20) L. Hultman: Vacuum **57** (2000) 1–30.
21) P. K. Huang and J. W. Yeh: Surf. Coat. Technol. **203** (2009) 1891–1896.

APPENDIX C

Paper 2: Effect of Y content in $(TaC)_{1-x}Y_x$ gate electrodes on flatband voltage control for Hf-based high-k gate stacks. Revised to Japanese journal of applied physics.

Effect of Y Content in $(TaC)_{1-x}Y_x$ Gate Electrodes on Flatband Voltage Control for Hf-based High-k Gate Stacks

Pattira Homhuan[1,*], Toshihide Nabatame[2], Toyohiro Chikyow[2] and Sukkaneste Tungasmita[3]

[1] Nanoscience and Technology, Graduate School, Chulalongkorn University, 254 Phayathai Road, Bangkok 10330, Thailand

[2]Advanced Electronic Materials Center, National Institute for Materials Science, Tsukuba, Ibaraki 305-0044, Japan

[3]Department of Physics, Faculty of Science, Chulalongkorn University, 254 Phayathai Road, Bangkok 10330, Thailand

[*]Corresponding author; E-mail address: Pattira_h@hotmail.com

Abstract

The effect of varying the Yttrium (Y) level in a $(TaC)_{1-x}Y_x$ gate electrode on the structural and electrical properties, including the flatband voltage (Vfb), for a Hafnium (Hf)-based high-k metal oxide semiconductor (MOS) capacitor was evaluated. The composition of $(TaC)_{1-x}Y_x$ was controlled by the power of the pure TaC and Y target in the magnetron sputtering. The structure of the formed $(TaC)_{1-x}Y_x$ film was that of either a face center cubic (FCC) at all compositions of $x \leq 0.4$ or amorphous at $x \geq 0.5$, after annealing at temperatures below 600 °C. X-ray photoelectron spectroscopy (XPS) analysis revealed that the TaC and $(TaC)_{1-x}Y_x$ films all contained about 10% oxygen. The resistivity of the $(TaC)_{1-x}Y_x$ films were invariant for all compositions of $x \leq 0.5$, but increased with increasing annealing temperatures up to 600 °C for compositions where $x \geq 0.68$. In the as-deposited case, the effective work function, which is estimated from the relationship between Vfb and the equivalent oxide thickness of the HfO_2 film, clearly changed from 4.8 to 4.3 eV as the x value increased. The Vfb of HfO_2 and $HfSiO_x$ dielectrics could be controlled within 0.5 V after annealing at 500 °C by changing the composition (in terms of the x value) of the $(TaC)_{1-x}Y_x$ film. Based on the experimental data, it is clear that $(TaC)_{1-x}Y_x$ composites are candidate materials for n-metal gate electrodes in the gate last process.

1. Introduction

In small scale (<45 nm) complementary metal-oxide-semiconductor devices (CMOS) a metal gate electrode and high-dielectric constant (κ) have been used to replace poly-crystalline Si and SiO_2, respectively. Recently, it has been reported that CMOS fabricated by either the gate-first or gate-last process are being mass produced[1, 2]. The gate-last process features a lower temperature fabrication compared to that of the gate-first process[1]. Hafnium (Hf)-based materials, including Hafnium oxide (HfO_2) and Hafnium silicate ($HfSiO_x$), are some of the most promising candidates. To control the flatband voltage (Vfb), several approaches have been demonstrated. Firstly, the effect of the capping that is deposited on the Hf-based high-k dielectrics on the control of Vfb has been evaluated. Here, a capping layer of MgO, SrO, Y_2O_3 or La_2O_3 materials was used in n-type MOS field-effect transistors (nMOSFETs)[3-5]. A second approach is to select metal materials that have a work function near the conduction band edge (4.1 eV) of Si[6]. Metal carbides, such as TaC, HfC and HfCN, with a sufficient thermal stability and a low effective work function (ϕm,eff), have been reported to be promising gate electrodes for nMOSFETs[6-10]. Indeed, interest in nitrogen-free TaC based materials has especially increased because of their high mobility[6, 7, 10]. However, it is insufficient to meet the requirement for a n-metal gate electrode because the ϕm,eff displays a wide range (4.2 – 4.9 eV)[10]. Therefore, we expect that a lower ϕm,eff could be obtained by introducing a Yttrium (Y) atom with a low work function of 3.1 eV to TaC materials.

In this paper, we report on the systematic investigation of the effect of varying the Y content in $(TaC)_{1-x}Y_x$ gate electrodes on the structural properties, resistivity and Vfb control for HfO_2 and $HfSiO_x$ MOS capacitors.

2. Experimental

Multiple $(TaC)_{1-x}Y_x$ -gated MOS capacitors were prepared as follows: A 3-nm-thick SiO_2 film was first formed on a p-type Si using a thermal process. Then, 3.5-, 4.2- and 4.9-nm-thick HfO_2, and 4.9-nm-thick $HfSiO_x$ films, with 60 at.% Hf were deposited on the SiO_2 film by a metalorganic chemical vapor deposition process. Post-deposition annealing was then carried out at 1050 °C under a N_2 atmosphere at ambient pressure. Typically, several 150-nm-thick $(TaC)_{1-x}Y_x$ films of different compositions, in terms of the x values, were each deposited on either the HfO_2 or $HfSiO_x$ film by horizontal magnetron sputtering method using TaC and Y metal targets. The elemental composition of each $(TaC)_{1-x}Y_x$ composite was controlled by

varying the sputtering power of both the TaC and Y target. Then, in order to decrease the whole resistance of the gate electrode, a 100-nm-thick Pt layer was deposited on some $(TaC)_{1-x}Y_x$ films. The annealing was performed at 500 and 600 °C for 30 s in N_2 after forming gas annealing (FGA) at 400 °C in 3% H_2. The Vfb value was estimated from the capacitance-voltage (C-V) characteristics using the program MIRAI-ACCEPT[11].

To examine the structural properties and resistivity of each film, 100-nm-thick $(TaC)_{1-x}Y_x$ films of different compositions (in terms of the x value) were also prepared on a SiO_2 (100 nm)/p-Si. The structure and chemical bond formation of the $(TaC)_{1-x}Y_x$ film were studied by x-ray diffraction (XRD) and x-ray photoelectron spectroscopy (XPS), respectively, whilst the resistivity of each film was measured by the two-probe method. C-V measurements were performed to study the electrical properties of the $(TaC)_{1-x}Y_x$-gated MOS capacitors, using a Keithley 4200 SCS semiconductor parameter analyzer.

3. Results and Discussion

3.1 Physical properties and resistivities of $(TaC)_{1-x}Y_x$ films

We examined the structural properties in $(TaC)_{1-x}Y_x$ films with various compositions (x values). **Fig. 1** shows the typical XRD patterns of $(TaC)_{1-x}Y_x$ films on the SiO_2 (100 nm)/p-Si after annealing at 600 °C. The XRD peaks of 2θ of 34.86° and 40.46°, corresponding to the (111) and (200) phases, respectively, of the face center cubic (FCC) structure of TaC, were observed in all compositions where $x \leq 0.4$. The $(TaC)_{1-x}Y_x$ films have a slight preference for the (111) orientation with the lowest plane density due to the limited atom mobility during the film growth[12]. The grain size, calculated by the Scherer formula, is less than 15 nm. In contrast, the films with a composition where the x value is 0.5 and 0.68 show an amorphous structure. It seems that the amorphous structure results from too high a Y content because it can make no-long-range order of the position. The adatoms or the incident flux of film species have a higher deposition rate (in unit of atoms) with an increase in Y content in films, the adatoms do not have enough time to diffuse on the substrate and to rearrange themselves in the crystal structure. They are buried by the subsequently deposited atoms. Therefore, the amorphous films can be formed.

The (111) and (200) peaks of the TaC phase shifted towards a lower diffraction angle as the x value in the composition increased, indicating an increase in the d-

spacing in the crystal structure. This is likely to be due to the strain domain in the film during the competitive growth stage. In fact, the lattice constant, which can be estimated from XRD peaks, increases with an increasing proportion of Y atoms in the $(TaC)_{1-x}Y_x$ films, as shown in **Fig. 2**. Moreover, the lattice constant relates to an increasing level of compressive stress in the films due to the formation of a solid solution[13]. No phase separation was observed in all compositions of the $(TaC)_{1-x}Y_x$ films evaluated. This could be due to the solid solution being formed, in which the Y atoms with a large ionic radius (0.090 nm) substitute for some of the positions of Ta atoms (0.068 nm radius) in the TaC cubic structure. In addition, the as-deposited $(TaC)_{1-x}Y_x$ film was found to consist of the same FCC and amorphous structures when $x \leq 0.4$ and $x \geq 0.5$, respectively.

To examine the chemical bond formation of the TaC film, the Ta4f, C1s and O1s spectra for the as-deposited TaC films formed with varying sputtering times from 0 to 900s were examined and the results are shown in **Fig. 3**. With respect to the Ta4f spectra (Fig. 3a), the 4f7/2 and 4f5/2 spin orbital splitting of the Ta-O, and Ta-C bonds were found at 26.2 and 28.1, and 23.0 and 24.8 eV, respectively. The intensity of the Ta-C bond increases as the sputtering time increases. However, it is clear that the Ta-O bond still remains in the films after sputtering for 900 s. For the C1s spectra (Fig. 3b), the absorbed carbon peak (285.4 eV) disappears entirely after sputtering for 300 s or longer. The peak at 282.8 eV, which corresponds to the Ta-C bond, appears in all sputtering times. The O1s peak also clearly remains, even after a sputtering time of 900 s (Fig. 3c). These indicate that the TaC films contain oxygen, and that the oxygen content was estimated to be at around 10%, as derived by integration of the area under the curve of the Ta-O bond.

The Y3d and O1s spectra of the $(TaC)_{0.71}Y_{0.29}$ films as a function of the sputtering time are shown in **Fig. 4**. With respect to the Y3d spectra, the Yttrium compound contains Y-Y (155 eV, 156.9 eV), Y-C (157.2 eV,159.1 eV) and Y-O (157.9 eV, 159.8 eV), with the Y-O bond remaining in the $(TaC)_{0.71}Y_{0.29}$ film after sputtering for 900 s, as determined from analysis of the Y3d and O1s spectra. In addition, the oxygen content in the $(TaC)_{1-x}Y_x$ films was almost the same at about 10%, regardless of the composition, in terms of the x value, of the $(TaC)_{1-x}Y_x$ films.

The resistivity of the $(TaC)_{1-x}Y_x$ films as a function of the Y content before and after annealing at 500 and 600 °C are shown in **Fig. 5**. The as-deposited

TaC and Y films show a higher resistivity than the bulk data[14-15] because of the sputtering damage. Note that the resistivity of the $(TaC)_{1-x}Y_x$ films is unchanged in the range $x \leq 0.5$ at 600 °C while the $(TaC)_{1-x}Y_x$ film with $x = 0.68$ increases significantly with an increasing annealing temperature. This can be explained as that an excess of Y atoms in $(TaC)_{0.32}Y_{0.68}$ introduces more impurity point defects[16]. Since the mean free path of electron conduction is inversely proportional to the resistivity[17], then an excess of Y atoms in the interstitial site or grain boundary decreases the mean free path. Therefore, the $(TaC)_{0.32}Y_{0.68}$ film shows the maximum resistivity.

3.2 Vfb behaviors of $(TaC)_{1-x}Y_x$-gated MOS capacitor with Hf-based high-k

Next the Vfb behavior of the Hf-based high-k MOS capacitors as a function of the composition (in terms of the x value) of the $(TaC)_{1-x}Y_x$ gate electrodes was evaluated. The C-V characteristics of the $(TaC)_{1-x}Y_x$-gated MOS capacitors with varying x value compositions on a HfO_2 (4.9 nm)/SiO_2 (3 nm) dielectric before annealing are shown in **Fig. 6**. Note that the capacitance is normalized to the maximum capacitance for ease of comparison. The C-V curves shift to a more negative value as the x value in the $(TaC)_{1-x}Y_x$ gate electrodes increases, although that for $(TaC)_{0.71}Y_{0.29}$ does not shift in a simple way because it has maximum fixed charges in the order of 10^{-11} cm^{-2} at the HfO_2/SiO_2 interface. **Fig. 7** shows the relationship between the Vfb and equivalent oxide thickness (EOT) of HfO_2 for the different $(TaC)_{1-x}Y_x$-gated MOS capacitors with HfO_2. The Vfb shifts to more negative values with increasing x values for each different HfO_2 film thickness. This indicates that the Y atoms with a low work function occur with a negative Vfb shift with an increasing x value in the $(TaC)_{1-x}Y_x$ gate electrodes. All samples exhibited an apparent or potential linear relationship between Vfb and EOT. The $\phi_{m,eff}$ values were determined from extrapolating the Vfb versus EOT plots, based on the following equation:

$$V_{fb} = (\phi_{m,eff} - \phi_{Si}) - \frac{Q_{ox}}{\varepsilon_o \cdot \varepsilon_{ox}} \times EOT_{HfO_2}, \quad (1)$$

where ϕ_{Si}, Q_{ox}, ε_{ox}, and EOT_{HfO2} are the Fermi-level of silicon substrate, the fixed charges, the dielectric constant of SiO_2 and the EOT of the HfO_2 film, respectively. This equation assumes that all fixed charges are at the HfO_2/SiO_2 interface[18]. Note

that the $\phi_{m,eff}$ values tend to decrease as the Y content increases and varies from 4.3 to 4.8 eV. The large value (4.7 eV) of the pure TaC gate is due to the influence of the oxygen content (about 10%) in the TaC, as previously reported[10]. Indeed, $\phi_{m,eff}$ can be low if the oxygen is eliminated from the sputtering system. The maximum observed $\phi_{m,eff}$ value, 4.8 eV for $(TaC)_{0.71}Y_{0.29}$, may be due to the fixed charges at the HfO_2/SiO_2 interfaces.

The Vfb change of the $(TaC)_{1-x}Y_x$ -gated MOS capacitors with a 4.2 and 4.9 nm thick HfO_2 film are shown in **Fig. 8**. It is clear that the Vfb values shift towards a negative direction as the x value increases regardless of the annealing temperature (at 500 and 600 °C). However, the x value is limited to less than 0.4 at 600 °C because of a high leakage current at 600 °C. In the case of $HfSiO_x$, the change in Vfb towards more negative values with increasing x values and annealing temperature was also noted and in a broadly similar manner to that seen in the case of with HfO_2, as shown in **Fig. 9.** The Vfb shift is approximately 0.5 and 0.2 V after annealing at 500 and 600 °C, respectively. Thus, the Vfb shift is not influenced by a high-k material but rather it depends strongly on the x value of the $(TaC)_{1-x}Y_x$ composition. It has previously been reported that the positive EWF shift can occur because of the dipole in the HfO2/SiO2 interface, whereas, the negative EWF can occur because of the metal carbide potential offset[19]. It has been well-known that bottom interface dipole at high-k/SiO2 strongly affects Vfb shift[20-21]. Actually, Y2O3 and La2O3 high-k materials show negative Vfb shift while Al_2O_3 high-k material shows a positive Vfb shift. In our case, Y atoms in $(TaC)_{1-x}Y_x$ metal gate electrode don't diffuse into HfO2 and HfSiOx films in low annealing temperature at 600 °C. The effect of the bottom interface dipole doesn't occur in this case. Therefore, the negative Vfb shift as a function of Y content is due to the change of work function of gate $(TaC)_{1-x}Y_x$ electrode. Therefore, the experimental data suggest that $(TaC)_{1-x}Y_x$ composites are a set of potential candidate materials for n-metal gate electrodes in the gate last process. These data also indicate that the $\phi_{m,eff}$ can be easily controlled by changing the Y content in the $(TaC)_{1-x}Y_x$ films.

4. Conclusion

We investigated the structural and electrical properties as a function of the composition in terms of the x value of $(TaC)_{1-x}Y_x$ gate electrodes for MOS capacitors with HfO_2 or $HfSiO_x$ dielectrics. The structure of the different $(TaC)_{1-x}Y_x$ films

maintained a FCC structure at all $x \leq 0.4$ compositions without phase separation after annealing at 600 °C, indicating thermal stability until at least 600 °C. The resistivity of $(TaC)_{1-x}Y_x$ films remained relatively low for compositions with $x \leq 0.5$ even at 600 °C. Note that the V_{fb} can be controlled over a wide range of about 0.5 V at 500 °C by changing the composition in terms of the x value in $(TaC)_{1-x}Y_x$ gate electrodes, regardless of the presence of high-k materials, such as HfO_2 and $HfSiO_x$ dielectrics. All $(TaC)_{1-x}Y_x$ films contain 10% oxygen content and the $\phi_{m,eff}$ attributes to higher value. These results suggest that $(TaC)_{1-x}Y_x$ composites with an x value below 0.5 are one set of candidate materials for n-metal gate electrodes in the gate-last process.

Acknowledgements

We are very grateful to The Commission on Higher Education and Graduate Thesis Grant, Thailand, and to the National Institute for Materials Science, Japan, for financial support enabling this research work. We also thank Mr. Hiroyuki Yamada and the members of MANA Foundry of International Center for Materials Nanoarchitectonics (MANA) of the National Institute for Materials Science, Japan.

References

1) S. C. Song, M. Hussain, J. Barnett, C. S. Park, C. Park, P. Kirsch, B. H. Lee, and R.Jammy: ECS Trans. **11** (2007) 315.

2) H. Zhao, J. Huang, Y. T. Chen, J. H. Yum, Y. Wang, F. Zhou, F. Xue, and J. C. Lee: Appl. Phys. Lett. **95** (2009) 253501.

3) V. Narayanan, V. K. Paruchuri, N. A. Bojarczuk, B. P. Linder, B. Doris, Y. H. Kim, S. Zafar, J. Stathis, S. Brown, J. Arnold, M. Copel, M. Steen, E. Cartier, A. Callegari, P. Jamison, J.-P. Locquetl, D. L. Lacey, Y. Wang, P. E. Batson, P. Ronsheim, R. Jammy, M. P. Chudzik, M. Leong, S. Guha, G. Shahidi, and T. C. Chen: VLSI Tech. Dig., 2006, p.224.

4) N. Mise, T. Morooka, T. Eimori, S. Kamiyama, K. Murayama, M. Sato, T.

Ono, Y. Nara, and Y. Ohji: IEDM Tech. Dig., 2007, p.527.

5) T. Morooka, T. Sato, T. Matsuki, T. Suzuki, K. Shiraishi, A. Uedono, S. Miyazaki, K. Yamada, T. Nabatame, T. Chikyow, J. Yugami, K. Ikeda, and Y. Ohji: VLSI Tech. Dig., 2010, p.33.

6) J. K. Schaeffer, C. Capasso, R. Gregory, D. Gilmer, l. R. C. Fonseca, M. Raymond, C. Happ, M. Kottke, S. B. Samavedam, P. J. Tobin, and B .E. White, Jr.: J. Appl. Phys. **101** (2007) 014503.

7) W. S. Hwang, C. Shen, X. P. Wang, D. S. H. Chan, and B. J. Cho: VLSI Tech. Dig., 2007, p.156.

8) W. Wang, T. Nabatame, N. Haneji, and Y. Shimogaki: Jpn. J. Appl. Phys. **32** (2005) L1019.

9) T. J. Park, J. H. Kim, J. H. Jang, K. D. Na, C. S. Hwang, G. M. Kim, K. J. Choi, and J. H. Jeong: Appl. Phys. Lett. **92** (2008) 202902.

10) W. Mizubayashi, K. Akiyama, W. Wang, M. Ikeda, K. Iwamoto, Y. Kamimuta, A.Hirano, H. Ota, T. Nabatame, and A. Toriumi: VLSI Tech Dig., 2008, p. 42.

11) N. Yasuda, H. Ota, T. Horikawa, T. Nabatame, H. Satake, A. Toriumi, Y. Tamura, T. Sasaki, and F. Ootsuka: Ext. Abstr. Solid State Devices and Materials (2005) p. 250.

12) L. Combadiere, and J. Machet: Surf. Coat. Technol. **88** (1996) 17.

13) G. Ababias: Surf. Coat. Technol. **202** (2008) 2223.

14) W. Lengauer: in Handbook of Ceramic Hard Materials, ed. R. Riedel (Wiley- VCH, the Federal Replublic of Germany, 2000) p. 203.

15) D. R. Lide: in Handbook of Chemistry and Physics: a ready book of chemical and physical data (CRC Press, New York, 2008) p. 12-40.

16) P. Homhuan, S. Chaiyakun, R. Thonggoom, N. Panich, and S. Tungasmita: Mater. Trans, JIMS. **51** (2010) 1651.

17) Y. K. Lee, J. Y. Kim, Y. K. Lee, M. S Lee, D. K. Kim, D. Y. Jin, T. H. Nam, H. J. Ahn, D. K. Park: J. Crystal Growth **234** (2002) 498.

18) J. K. Schaeffer, L. R. C. Fonseca, S. B. Samavedam, Y. Liang, P. J. Tobin, and B. F. White: Appl. Phys. Lett. **85** (2004) 1826.

19) W. Mizubayashi, K. Akiyama, W. Wang, M. Ikeda, K. Iwamoto, Y. Kamimuta, A. Hirano, H. Ota, T. Nabatame, and A. Toriumi: Appl. Surf. Sci. **254** (2008) 6123.

20) K. Kita, and A. Toriumi: Appl. Phys. Lett. **94** (2009) 132902.

21) K. Iwamoto, Y. Kamimuta, A. Ogawa, Y. Watanabe, S. Migita, W. Mizubayashi, Y. Morita, M. Takahashi, H. Ota, T. Nabatame, and A. Toriumi: Appl. Phys. Lett. **92** (2008) 132907.

Figure captions

Fig. 1 Representative XRD patterns of $(TaC)_{1-x}Y_x$ thin films on SiO_2/Si dielectric film at various compositions of x = 0, 0.17, 0.29, 0.40, 0.50 and 0.68, respectively. All samples were annealed at 600 °C.

Fig. 2 Lattice constant of different composition $(TaC)_{1-x}Y_x$ films as a function of the x value before and after annealing at 500 and 600 °C. The open symbol represents the bulk data for the FCC structure of TaC.

Fig. 3 Representative XPS spectra of (a) Ta4f, (b) C1s and (c) O1s in the as-deposited TaC films on SiO_2/Si with changing sputtering times.

Fig. 4 Representative XPS spectra of (a) Y3d and (b) O1s in the as-deposited $(TaC)_{0.71}Y_{0.29}$ films on SiO_2/Si with changing sputtering times.

Fig. 5 Resistivity of the different composition $(TaC)_{1-x}Y_x$ films on SiO_2/Si as a function of the x value before and after annealing at 500 and 600 °C. The open circle and triangle represent the TaC and Y bulk data, respectively.

Fig. 6 Representative C-V characteristics of various $(TaC)_{1-x}Y_x$ /HfO_2 (4.9 nm) /SiO_2 (3 nm)/Si MOS capacitors before annealing. The x values in the $(TaC)_{1-x}Y_x$ gate electrodes were varied from 0 to 1.

Fig. 7 Relationship between the Vfb and EOT of HfO_2 for HfO_2 MOS capacitors with a $Ta_{1-x}Y_xC_{1-x}$ gate electrode of varying x values before the annealing process. The $\phi_{m,eff}$ values were estimated by extrapolating to the y-axis.

Fig. 8 The change in Vfb of the $(TaC)_{1-x}Y_x$-gated MOS capacitors with a (a) 4.9 and (b) 4.2 nm thick HfO_2 layer as a function of the x value. The annealing was performed at 500 and 600 °C in a N_2 atmosphere after FGA at 400 °C in H_2.

Fig. 9 The Vfb change of $(TaC)_{1-x}Y_x$-gated MOS capacitors with a 4.9 nm $HfSiO_x$ layer as a function of the x value. Post-deposition annealing was performed at 500 and 600 °C under a N_2 atmosphere after FGA at 400 °C in H_2.

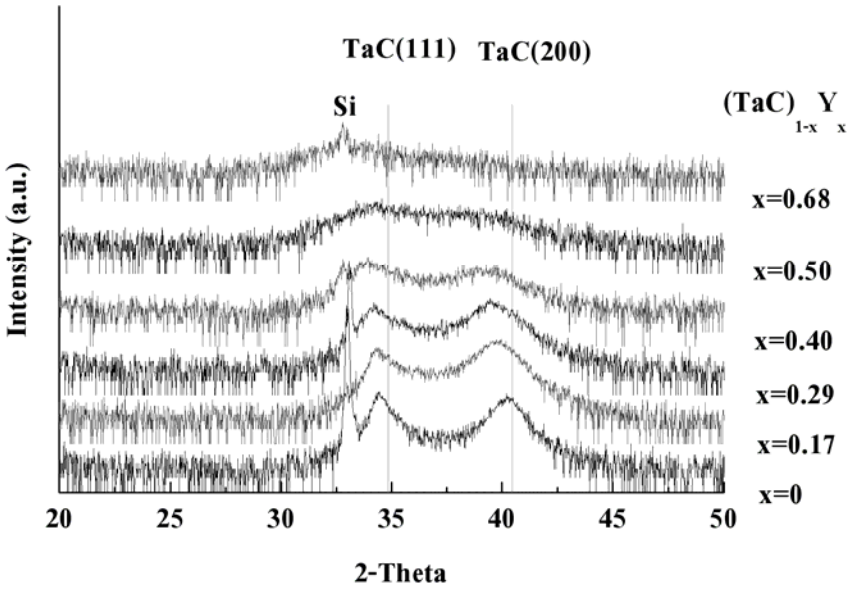

Fig. 1 Representative XRD patterns of $(TaC)_{1-x}Y_x$ thin films on SiO_2/Si dielectric film at various compositions of x = 0, 0.17, 0.29, 0.40, 0.50 and 0.68, respectively. All samples were annealed at 600 °C.

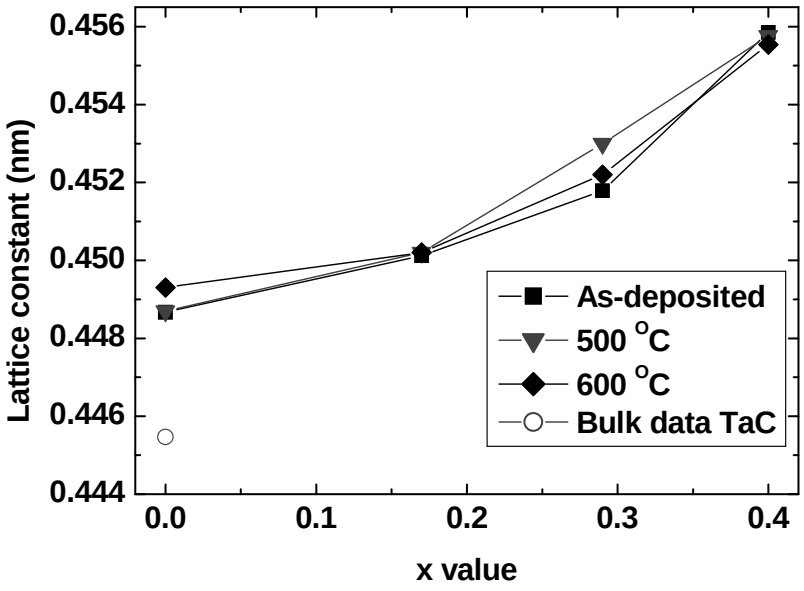

Fig. 2 Lattice constant of different composition $(TaC)_{1-x}Y_x$ films as a function of the x value before and after annealing at 500 and 600 °C. The open symbol represents the bulk data for the FCC structure of TaC.

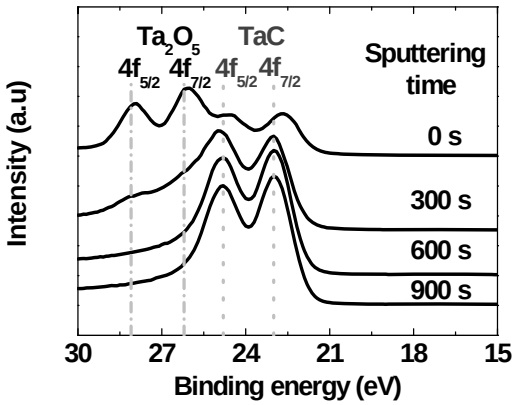

(a)

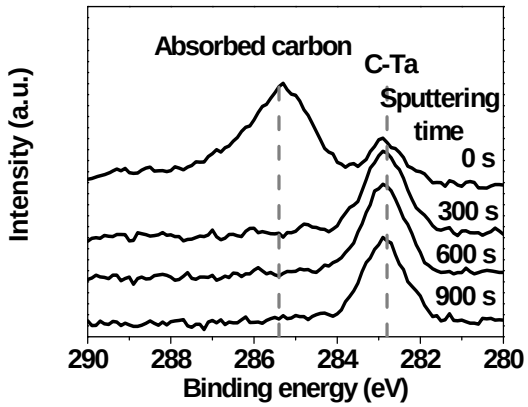

(b)

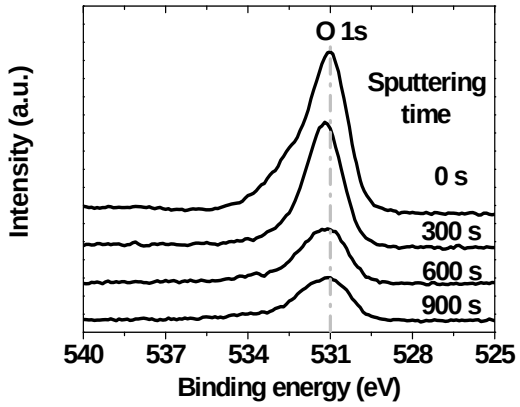

(c)

Fig. 3 Representative XPS spectra of (a) Ta4f, (b) C1s and (c) O1s in the as-deposited TaC films on SiO_2/Si with changing sputtering times.

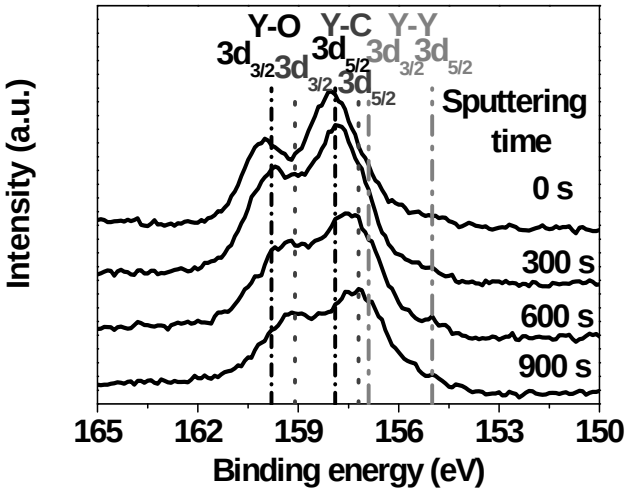

(a)

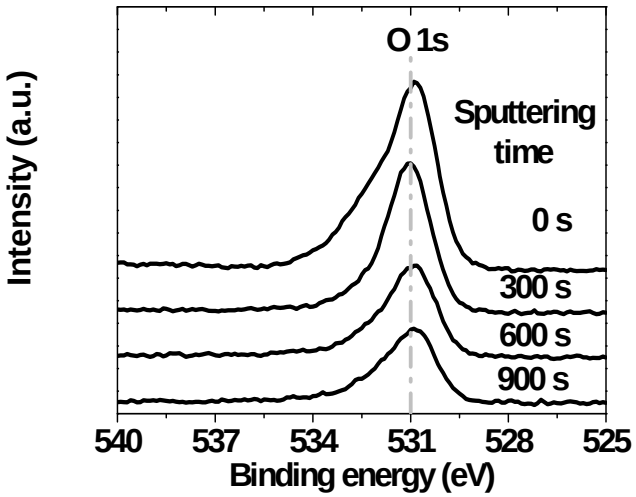

(b)

Fig. 4 Representative XPS spectra of (a) Y3d and (b) O1s in the as-deposited $(TaC)_{0.71}Y_{0.29}$ films on SiO_2/Si with changing sputtering times.

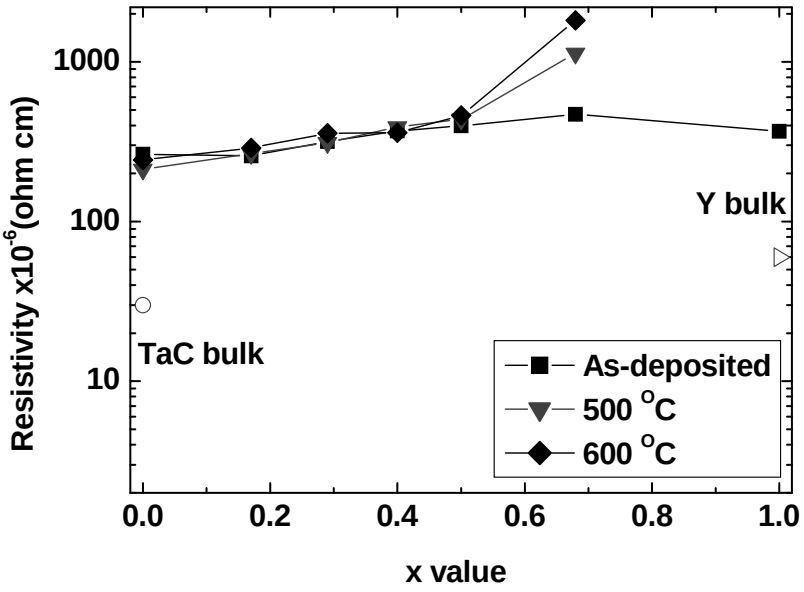

Fig. 5 Resistivity of the different composition $(TaC)_{1-x}Y_x$ films on SiO_2/Si as a function of the x value before and after annealing at 500 and 600 °C. The open circle and triangle represent the TaC and Y bulk data, respectively.

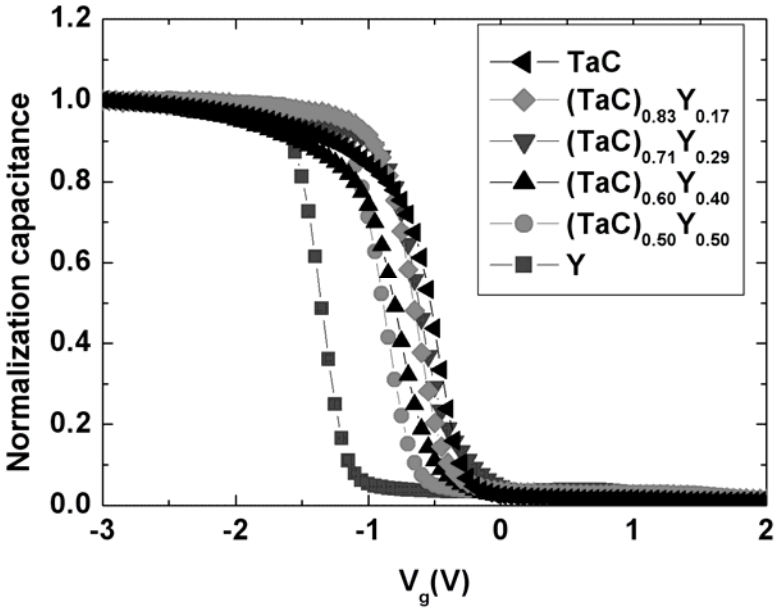

Fig. 6 Representative C-V characteristics of various $(TaC)_{1-x}Y_x$ /HfO_2 (4.9 nm) /SiO_2 (3 nm)/Si MOS capacitors before annealing. The x values in the $(TaC)_{1-x}Y_x$ gate electrodes were varied from 0 to 1.

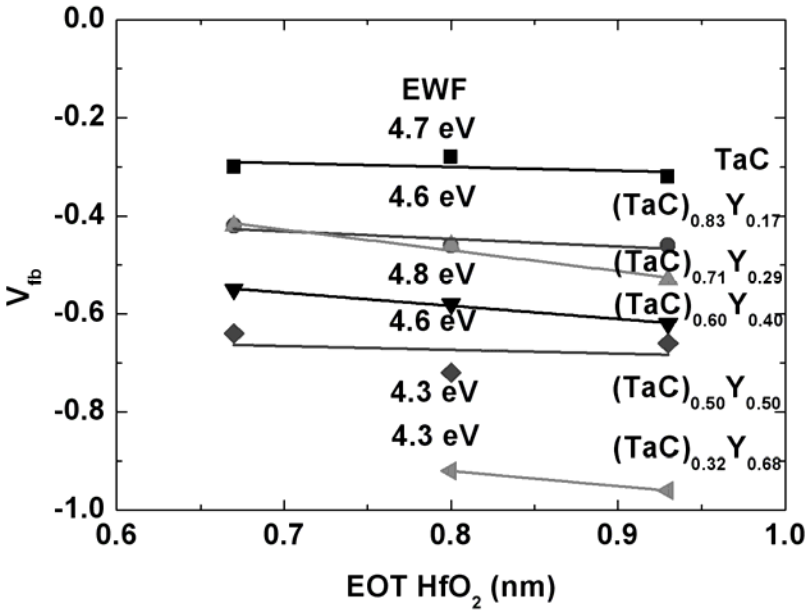

Fig. 7 Relationship between the Vfb and EOT of HfO_2 for HfO_2 MOS capacitors with a $(TaC)_{1-x}Y_x$ gate electrode of varying x values before the annealing process. The $\phi_{m,eff}$ values were estimated by extrapolating to the y-axis.

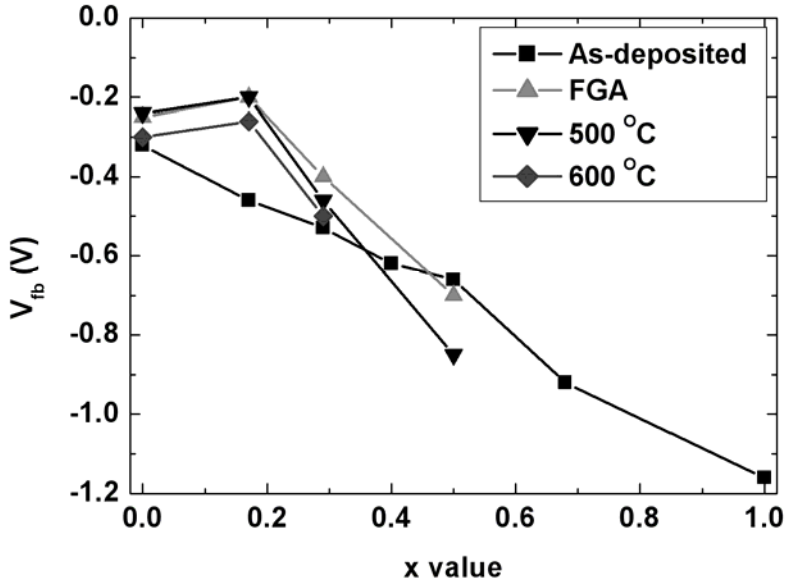

(a)

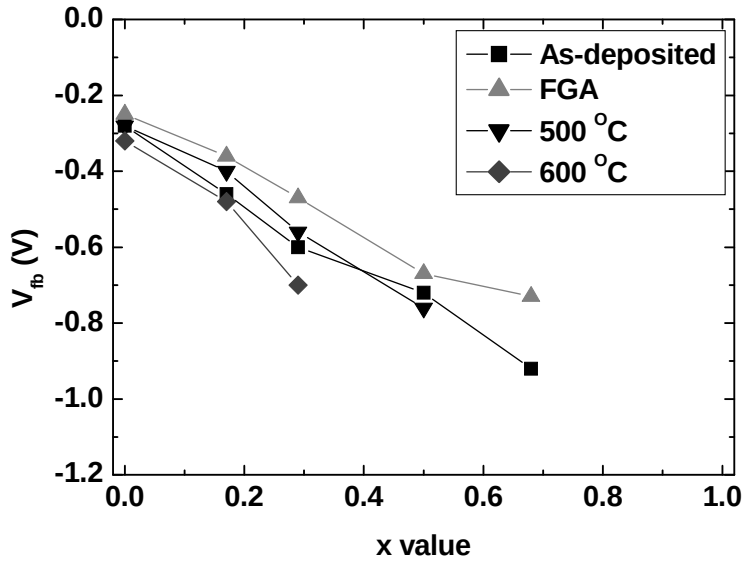

(b)

Fig. 8 The change in Vfb of the $(TaC)_{1-x}Y_x$ -gated MOS capacitors with a (a) 4.9 and (b) 4.2 nm thick HfO_2 layer as a function of the x value. Post-deposition annealing was performed at 500 and 600 °C in a N_2 atmosphere after FGA at 400 °C in H_2.

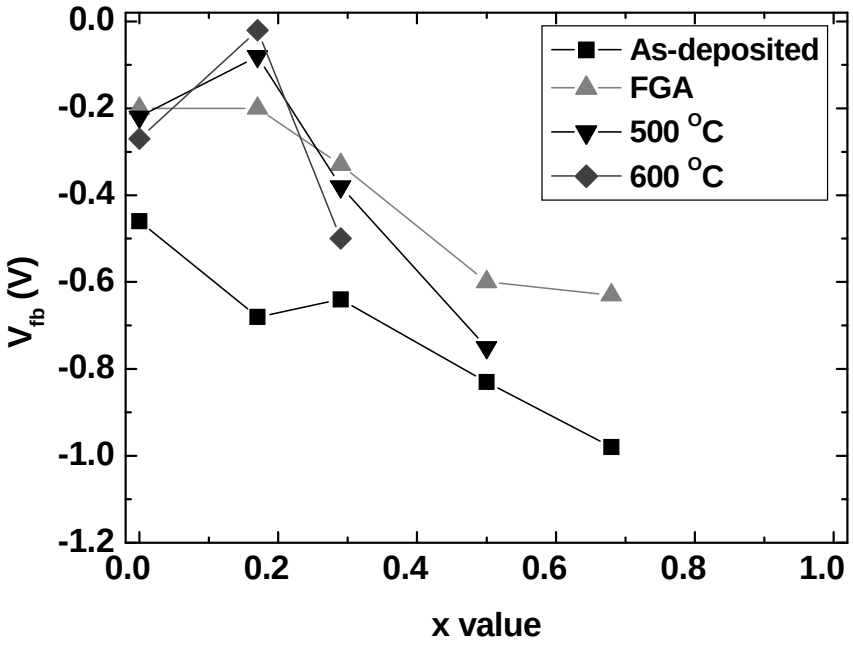

Fig. 9 The Vfb change of $(TaC)_{1-x}Y_x$ -gated MOS capacitors with a 4.9 nm $HfSiO_x$ layer as a function of the x value. Post-deposition annealing was performed at 500 and 600 °C under a N_2 atmosphere after FGA at 400 °C in H_2.

APPENDIX D

Paper 3: 2008. Low-temperature growth of chromium nitride thin films for wear protective coating, by reactive DC magnetron sputter deposition. The journal of scientific research Chulalongkorn university 33: 43-49.

Low-Temperature Growth of Chromium Nitride Thin Films for Wear-Protective Coating, by Reactive DC Magnetron Sputter Deposition

Pattira Homhoul[1], Chakrapan Thavornthira[2], Surasing Chaiyakun[2] and Sukkaneste Tungasmita[1, 3*]

[1]*The Graduate Program in NanoScience and Technology, Graduate School, Chulalongkorn University, Bangkok 10330, Thailand*
[2]*Department of Physics, Faculty of Science, Burapa University, Chonburi 20131, Thailand*
[3]*Department of Physics, Faculty of Science, Chulalongkorn University, Bangkok 10330, Thailand*

ABSTRACT: Chromium nitride (CrN) thin films was deposited on Si(100) substrates by reactive DC magnetron sputtering at different substrate temperatures in a low-growth temperature regime. The optimized condition to obtain stoichiometric chromium nitride material was evaluated when using a nitrogen partial pressure in the process of between 20-40% of the total pressure. The growth temperature was varied from room temperature up to 250°C. Increasing the growth temperature causes the development of CrN(200) domains whilst the CrN(111) domain dominates at all growth temperatures. The chemical composition of all the films was in the stoichiometric range. At higher growth temperatures, the surface morphology tended to be smoother due to an increasing degree of adatoms mobility on the substrate surface during film growth. This also influences the mechanical and tribological properties of the films. The hardness of the films increased as the growth temperature increased with, at 250°C, the highest hardness at 18.2 GPa and the lowest wear rate of 9.32 x 10^{-3} mm^3/ Nm being attained.

Key words: Chromium nitride, magnetron sputter deposition, wear-protective coating

INTRODUCTION

Transition metal nitride thin films, deposited by physical vapor deposition (PVD) techniques have been developed and used as mechanical and chemical protective layers in modern industrial applications for many years. Cubic-based structured chromium nitride (CrN) is one interesting choice in recent years due to its properties being well matched to some industrial requirements, especially for hard coating and tribology applications. Chromium nitride has a high hardness, wear, corrosion, and high temperature oxidation resistance even at temperatures as high as 700°C, and also has a low friction coefficient.[1-3] Due to its ceramic-like properties, this material becomes essentially a chemical inert material exhibiting a high corrosive resistance in various environments.[4] These properties make thin film coating with chromium nitride have a lot of potential to be used in diverse applications, e. g., to improve the life time of cutting tools, die casting molds, automotive moving parts and decorative materials.[5,6] Synthesized by physical vapor deposition techniques, such as reactive magnetron sputtering process, CrN thin film coating can be an alternative to the electrochemical hard chrome production that produces harmful hard chrome contaminated waste into the environment.[7] Moreover, CrN is also a biocompatible material that can be used in biomedical applications.[8]

* *Correspondence to: e-mail: Sukkaneste.T@chula.ac.th*

In this work, we present our investigations on the growth of chromium nitride thin films by reactive D. C. magnetron sputtering in a low-temperature growth regime, from room temperature up to 250°C. These studies and development suggest that CrN can be applied as a protective coating on some temperature sensitive substrates, such as treated steels, polymers or plastics which would otherwise be damaged or impaired by high temperature growth, such as the induction of defects and stress, or degradation.

EXPERIMENTAL DETAILS

The CrN thin films were deposited on silicon (100) substrates by reactive DC magnetron sputter deposition technique. Prior the growth, the substrates were ultrasonically cleaned; following a standard cleaning procedure in trichloroethylene (TCE), acetone, alcohol and de-ionized water, respectively. The thin native oxide layer on the surface of the substrate was removed by an acid etching, using a 10% (v/v) solution of HF for 20 seconds and then rinsed with de-ionized water before blow drying with nitrogen gas and loading into the vacuum chamber. The system was then evacuated down to a base pressure of about 2.0×10^{-5} Torr. In the sputtering process, CrN thin films were produced from a reactive sputter process of pure chromium target (99.99%) in an argon and nitrogen mixed atmosphere (99.99% purity). The argon and the nitrogen flows were controlled by a mass flow controller and kept constant at 6.7 and 8.7 sccm, respectively. The nitrogen partial pressure was set at 25% of the total mixture pressure. At a target-to-substrate distance of about 13 cm, a total gas pressure of 6 mTorr and a target power at 450 W, a CrN deposition rate of about 0.2 nm/sec was yielded. This is our optimum condition that gives a stiochiometric CrN material in a low growth temperature regime. However, our preliminary results indicate that a stoichiometric CrN thin film can be formed using a nitrogen partial pressure in the process of between 20-40%. During deposition, substrates were on floating potential and the deposition time was kept at 60 min for each sample. Substrates were heated by an irradiative heater and the growth temperatures during deposition were varied from room temperature up to 250°C. As-deposited CrN films were characterized by X-ray diffraction (XRD) for the structural information using a Phillips MRD Diffractometer and Bruker D8 Discover X-ray Diffractometer. The chemical composition and topography of the films were evaluated using Jeol JSM-5800 scanning electron microscope (SEM), equipped with the Oxford - ISIS energy dispersive spectroscopy (EDS). The surface morphology and root-mean-square roughness of all the samples were investigated by using a Veeco Nanoscope-V atomic force microscope (AFM). For mechanical properties of the CrN films, the nano-indentation was performed to measure the mechanical hardness of the films, using a special Berkovich diamond indent tip attached to the Nanoscope-V AFM. The same tip was also used in the scratch test mode to obtain the friction coefficient value and wear rate.

RESULTS AND DISCUSSION

The chemical composition of the as-deposited chromium nitride thin films was measured by using SEM/EDS with the primary electron energy of about 20 keV. The results from energy dispersive spectra, show the contents of the chromium and nitrogen from different growth temperatures. Since the growth of the metallic nitride materials by the reactive process is quite sensitive to the nitrogen concentration of the reactive gas mixture during deposition, we performed preliminary experiment to determine the nitrogen partial pressure that was required for the growth of stoichiometric chromium nitride materials: the "*process window*", by examining the stoichiometric ratio of chromium/nitrogen as a function of nitrogen partial pressure in the growth process. These results indicated that the required partial pressure of nitrogen in the film growth process was in the range of between 20-40% of the total pressure (data not shown). With higher nitrogen levels in the reactive gas mixture, the chromium nitride film becomes over-stoichiometric and exhibits a dark grey or black color film. On the other hand, when the nitrogen concentration is lower than 20%, the chromium nitride film becomes under-stoichiometric and appears closer to pure chromium films. Therefore, using this range of nitrogen partial pressures as an initial growth condition, the effects on the growth temperature was investigated. The Cr/N compositions of the films grown at low temperatures are just slightly under-stoichiometric and become stoichiometric as the growth temperature increases from 100°C upwards, as shown in Figure 1. This is a rather typical behavior for the low temperature growth in reactive nitriding process, due to insufficient internal energy to incorporate nitrogen into the material to form the metallic-nitride, which is thus improved as the external thermal energy is increased.

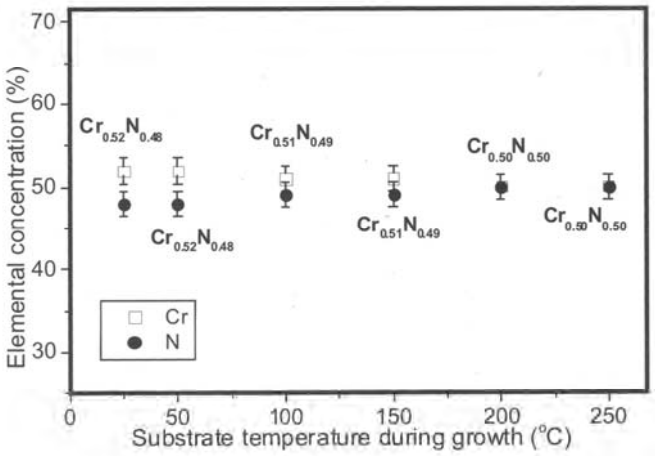

Figure 1. The elemental compositions of the CrN thin films grown at different substrate temperatures, measured by energy dispersive x-ray spectroscopy (EDS). All the films exhibited near- or stoichiometric compositions.

The structural characterization of the as-deposited films was investigated by XRD. The diffractograph of CrN thin films deposited at different growth temperatures, in a semi-log scale, is shown in Figure 2. It was clearly seen in the diffractographs that, for all the growth temperatures of chromium nitride thin films, the CrN(111) domain peak remains as a dominate peak in all substrate temperatures. As the growth temperature increased, the CrN(200) domain peak starts to develop at a temperature of about 100°C and can clearly observed from the samples grown at 250°C. This shows the semi-thermodynamic transformation point of the CrN preferred orientation growth with our optimum growth condition. The positions of the CrN(200) domain peak shifts towards lower 2θ values, as can be noticed in Figure 2. The decrease in the diffraction angles likely results from an increase in the d-spacing in the crystal structure due to the strain of CrN(200) domains in the films during the competitive growth stage. Generally, at low growth temperatures, the growth of the CrN film is controlled by the *surface energy*[9] resulting in the (111) preferred orientation. For higher growth temperatures, the growth of the CrN film is controlled by the *strain energy*[9] and as a result, the (200) orientation starts to develop. The (111) preferred orientation, which has the lowest surface energy,[10] can be observed at all growth temperatures. Moreover, this (200) orientation is a stable surface[9] and has the lowest strain energy at high temperatures. In this manner, there is a competitive growth between (111) and (200) oriented domains of CrN. This is quite typical for the growth mechanism to prefer the kinetic limitations rather than the thermodynamic driving force.[11] In addition, the microstructure evolution during the film growth can occur because of the increasing diffusion of the transition metal atom in the crystalline plane which develops from the lowest surface energy to the plane with a higher surface energy.[12] Moreover, the full width at half maximum (FWHM) can be determined from the XRD peak by fitting the peak width with a Pseudo-Voigt function. The peak broadening appears because of the crystal imperfection due to the mosaic structure in the film structure.[13] At higher growth temperatures, the mosaic structure is increased. The FWHM of CrN(111) peak tends to increase as the growth temperature increases, due to development of the CrN(200) oriented domains and a competitive growth mechanism between CrN(111) and CrN(200).[12] Due to the broadening peak of CrN(200), a non-uniform strain occurs at this plane.[13]

The surface morphology of CrN thin films was investigated by atomic force microscope (AFM), as shown in micrographs of Figure 3 and the values of the root-mean-square (RMS) surface roughness for all the growth conditions are summarized in Figure 4. The images show a mixing feature between the large and small surface grains. According to the Thornton's structure zone diagram for PVD, the melting temperature of CrN is 1773K[14] which makes the ratio between the substrate temperature to the film material melting temperature (T_S/T_m) of between 0.168 and 0.295 for growth temperatures between room temperature and 250°C. The Thornton's structural zone of the CrN thin films could be predicted to fall in between the "zone 1" and "zone T" due to the lack of surface mobility of adatoms on the substrate. Figure 4 shows the root-mean-square (RMS) surface roughness of CrN thin films as a function of substrate

temperature during growth. As the temperature increases, the roughness is decreased due to the increasing adatoms mobility resulting from the additional thermal energy present from substrate heating. As seen in Figure 4, the surface roughness of CrN thin films, when grown at 100°C, had the maximum value because of the competitive growth and the changing crystallographic preferred orientation between CrN(200) and CrN(111).

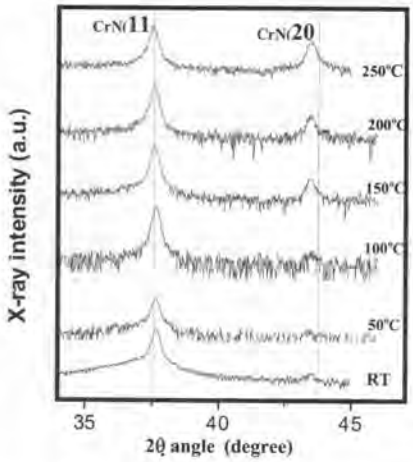

Figure 2. The x-ray diffraction (XRD) patterns of the CrN thin films grown on Si(001) substrates at different substrate temperatures (in semi-logarithm scale). Note that, the CrN(200) domain peaks have shifted from the bulk position, indicating some strain in the film structure.

The mechanical and tribological properties of these CrN films were also measured. A nano-indentation with a Berkovich-type diamond indent tip at different tip loads was performed to determine the mechanical hardness of the films. The hardness values and wear rates obtained from the nano-indentation and nano-scratch tests are summarized in Figure 5. The hardness of CrN films tends to increase as the substrate temperature increases at least above 100°C, and is likely due to the development of CrN(200) domains at the higher growth temperatures. The CrN material grown at 250°C, exhibited the highest film hardness at 18.2 GPa. In contrast, the CrN thin film grown at 100°C, showed the lowest hardness at 5.6 GPa. This can be explained by the competitive growth mechanism between the two crystallographic domains, CrN(200) and CrN(111), at the growth temperature of 100°C. The same aspects are noticeable from the wear rate values. The maximum wear rate (93.52 x 10^{-3} mm^3/ Nm) was observed with the film grown at 100°C, whilst the CrN film grown at 250°C yielded the minimum wear rate some ten fold lower (9.32 x 10^{-3} mm^3/ Nm). The average friction coefficient of the CrN thin films was calculated to be about 0.36. The presence of CrN(200) domains in the film structure helped to enhance the mechanical and tribological properties of the CrN thin film layer as seen from the result of films grown at 250°C, which have the highest hardness and the lowest wear rate for the protective coating layer in application perspectives. However, there are more factors that need to be considered, for example: residual stress in the film and adhesion between the film and the substrate, which can contribute to both mechanical and tribological properties of the materials.

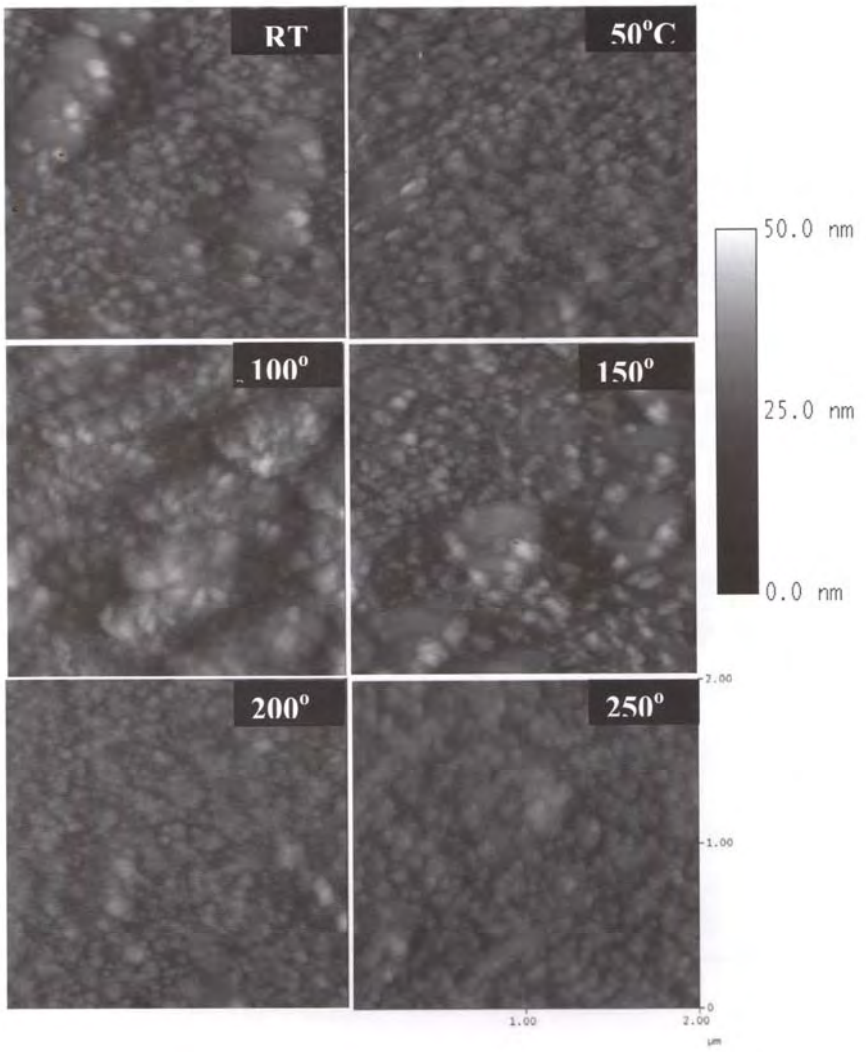

Figure 3. The 2 x 2 μm of surface morphology images from atomic force microscope (AFM) on the CrN thin films, grown at different substrate temperatures.

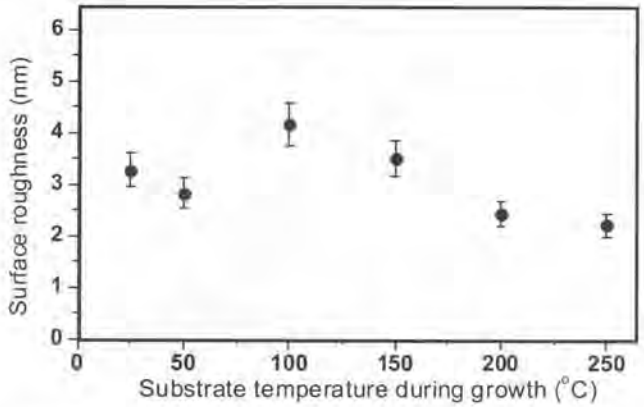

Figure 4. The root-mean-square (RMS) surface roughness of CrN thin films grown on Si(001) substrates at different substrate temperatures.

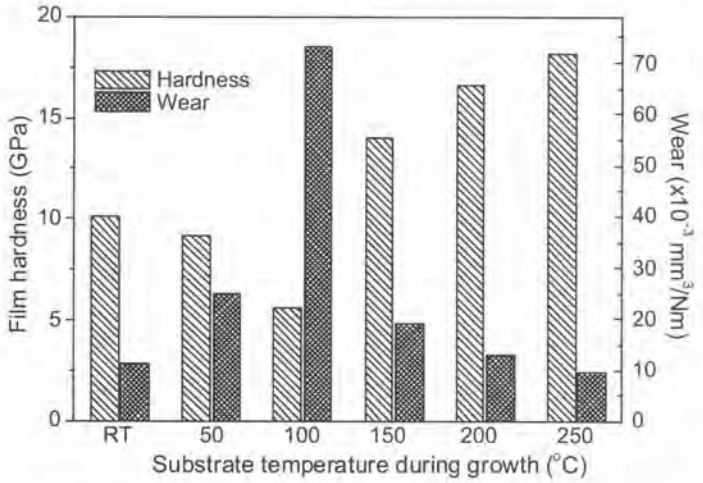

Figure 5. The film material hardness (left Y-axis) and wear (right Y-axis) of CrN thin films grown at different substrate temperatures.

SUMMARY

CrN thin film layers have been deposited on Si substrates by DC reactive magnetron sputtering from a metallic target in a mixed nitrogen and argon atmosphere. By maintaining the nitrogen partial pressure at 20% and keeping the flow rate of Ar and N_2 constant during the deposition period, we achieved the preferred conditions to grow CrN thin films with a stoichiometric Cr/N ratio in the film material at all substrate temperatures. The CrN(111) texture dominates at all growth conditions, but CrN(200) domains started to appear as the temperature increases above 100°C and becomes more pronounced with increasing temperature, presumably due to the change in growth mechanism from the lowest surface energy to the higher surface energy. The increasing FWHM of CrN peaks indicated an increase in the mosaicity of the crystal structure as a result from the competitive growth mechanism between two domains of CrN material. This is also reflected in the surface morphology of the films. The hardness of CrN thin

films increases as the growth temperature increases. Film grown at 250°C had the highest hardness (18.2 GPa) and the lowest wear rate (9.32 x 10^{-3} mm^3/Nm). The films grown at 250°C have the highest potential as candidates for protective coating and wear resistance layers to extend the lifetime of the substrates that require low-temperature process.

ACKNOWLEDGMENTS

Some parts of this work are financial supported by the grant from Ratchada-piseksompoch Program and the Thailand Research Fund (TRF) contract no. RDG4850024. The additional support was provided by the Graduate School of Chulalongkorn University.

REFERENCES

1. Bertrand, G., Savall, C. and Meunier, C. (1997) *Surf. Coat. Technol.* **96**, 323.
2. Sue, J. A. and Chang, T. P. (1997) *Surf. Coat. Technol.* **76-77**, 61.
3. Hand, Z., Tian, J. Lai, Q., Yu, X. and Li., G. (2003) *Surf. Coat. Technol.* **162**, 189.
4. Urgen, M. and Cakir, A. F. (1997) *Surf. Coat. Technol.* **96**, 236.
5. Navinsek, B. and Panjan, P. (1995) *Surf. Coat. Technol.* **74-75,** 919.
6. Rebholz, C., Zeigele, H., Leyland, A. and Matthews, A. (1999) d*Surf. Coat. Technol.* **115,** 222.
7. Barata, A., Cunha, L. and Moura, C. (2001) *Thin Solid Films.* **398-399,** 501.
8. J. Fisher and *et. al.* (2002) Proc. Inst. Mech. Eng[H], **216**, 219.
9. Min, J. J., Kyung, H. N., Yun, M. J. and Jeon. G. H. (2003) *Surf. Coat. Technol.* **171,** 59.
10. Ensinger, W. (1998) *Surf. Coat. Technol.* **99,** 1.
11. Schell, N., Peterson, J. H., Bottiger, J., Mucklich, A., Chevallier, J., Andresen, K. P. and Eichhorn, F. (2003) *Thin Solid Films.* **426**, 100.
12. Olaya, J. J., Rodil, S. Muhl, E. S. and Huerta, L. (2006) *Surf. Coat. Technol.* **200**, 5743.
13. Cullity, B. D. (1956) *Elements of X-Ray Diffraction.* Massachusetts: Addison-Wesley Publishing.
14. Mientus, R. and Ellmer, K. (1999) *Surf. Coat. Technol.* **116-119**, 1093.

Received: September 17, 2007
Accepted: June 21, 2008

VITAE

Miss Pattira Homhuan was born on October 7, 1979 in Ayutthaya, Thailand. She received a Bachelor's Degree of Science (second class honors) in Physics from Chulalongkorn University in 2000 followed by a Master's Degree of Science in Physics from Chulalongkorn University in 2005. She continued her Doctoral Degree in Nanoscience and Technology from Chulalongkorn University in 2006.

Miss Pattira Homhuan has been a regular participant in the national and international conferences and received an award for "Best Paper Award of Surface Treatment" at the 5th Thailand Materials Science and Technology Conference, Thailand on 16-19 September 2008".

During her studies in the doctoral program, she received a scholarship from The Commission on Higher Education for six months, she stayed in Japan to join the NIMS Internship Program at National Institute for Materials Science in Japan to research high-k dielectric and metal gate with Dr. Toshihide Nabatame and Dr. Toyohiro Chikyow at Advanced Electronic Materials Center, National Institute for Materials Science, Japan.

PUBLICATIONS LIST

1. **Pattira Homhuan**, Surasing Chaiyakun, Rattaporn Thonggoom, Nurot Panich, and Sukkaneste Tungasmita. 2010. Growth and structural characterizations of nanostructured chromium-zirconium-nitride thin films for tribological applications. Material transactions, The Japan Institute of Materials 51:1651-1655.
2. **Pattira Homhuan**, Toshihide Nabatame, Toyohiro Chikyow and Sukkaneste Tungasmita. Effect of Y content in $(TaC)_{1-x}Y_x$ gate electrodes on flatband voltage control for Hf-based high-k gate stacks. Revised to Japanese Journal of Applied Physics.
3. **Pattira Homoul**, Chakrapan Thavornthira, Surasing Chaiyakun and Sukkaneste Tungasmita. 2008. Low-temperature growth of chromium nitride thin films for wear-protective coating, by reactive DC magnetron sputter deposition. The Journal of Scientific Research Chulalongkorn University 33: 43-49.
4. **Pattira Homhuan**, Surasing Chaiyakun, Rattaporn Thonggoom, and Sukkaneste Tungasmita. Room-Temperature Growth of Chromium Zirconium Nitride Thin Films by Unbalanced Magnetron Sputtering. In manuscript.